



**International Doctorate School in Information and
Communication Technologies**

DISI - University of Trento

**DESIGN AND CHARACTERIZATION OF A CURRENT ASSISTED
PHOTO MIXING DEMODULATOR FOR TOF BASED 3D CMOS
IMAGE SENSOR**

Quazi Delwar Hossain

Advisor:

Prof. Gian-Franco Dalla Betta

DISI, University of Trento,

Trento, Italy

Abstract

Due to the increasing demand for 3D vision systems, many efforts have been recently concentrated to achieve complete 3D information analogous to human eyes. Scannerless optical range imaging systems are emerging as an interesting alternative to conventional intensity imaging in a variety of applications, including pedestrian security, biomedical appliances, robotics and industrial control etc. For this, several studies have reported to produce 3D images including stereovision, object distance from vision system and structured light source with high frame rate, accuracy, wide dynamic range, low power consumption and lower cost. Several types of optical techniques for 3D imaging range measurement are available in the literature, among them one of the most important is time-of-flight (TOF) principle that is intensively investigated. The third dimension, i.e. depth information, can be determined by correlating the reflected modulated light signal from the scene with a reference signal synchronous with the light source modulation signal.

CMOS image sensors are capable of integrating the image processing circuitry on the same chip as the light sensitive elements. As compared to other imaging technologies, they have the advantages of lower power consumption and potentially lower price. The merits make this technology competent for the next-generation solid-state imaging applications. However, CMOS process technologies are developed for high-performance digital circuits.

Different types of 3D photodetectors have been proposed for three-dimensional imaging. A major performance improvement has been found in the adoption of inherently mixing detectors that incorporate the role of detection and demodulation in a single device. Basically, these devices use a modulated electric field to guide the photo generated charge carriers to different collection sites in phase with a modulation signal. One very promising CMOS photonic demodulator based on substrate current modulation has recently been proposed. In this device the electric field penetrates deeper into the substrate, thus enhancing the charge separation and collection mechanism. A very good sensitivity and high demodulation efficiency can be achieved.

The objective of this thesis has been the design and characterization of a Current Assisted Photo mixing Demodulator (CAPD) to be applied in a TOF based 3D CMOS sensing system. At first, the experimental investigation of the CAPD device is carried out. As a test vehicle, 10×10 pixel arrays have been fabricated in $0.18 \mu\text{m}$ CMOS technology with $10 \times 10 \mu\text{m}^2$ pixel size. The main properties of CAPD devices, such as the charge transfer characteristic, modulation contrast, noise performance and non-linearity problem, etc. have been simulated and experimentally evaluated. Experimental results demonstrate a good DC charge separation efficiency and good dynamic demodulation capabilities up to 45MHz. The influence of performance parameters such as wavelength, modulation frequency and voltage on this device is also discussed. This test device corresponds to the first step towards incorporating a high resolution TOF based 3D CMOS image sensor.

The demodulator structure featuring a remarkably small pixel size $10 \times 10 \mu\text{m}^2$ is used to realize a 120×160 pixel array of ranging sensor fabricated in standard $0.18 \mu\text{m}$ CMOS technology. Initial results demonstrate that the demodulator structure is suitable for a real-time 3D image sensor. The prototype camera system is capable of providing real-time distance measurements of a scene through modulated-wave TOF measurements with a modulation frequency 20 MHz. In the distance measurement, the sensor array provides a linear distance range from 1.2m to 3.7m with maximum accuracy error 3.3% and maximum pixel noise 8.5% at 3.7m distance. Extensive testing of the device and prototype camera system has been carried out to gain insight into the characteristics of this device, which is a good candidate for integration in large arrays for time-of-flight based 3D CMOS image sensor in the near future.

Keywords- Time-of-Flight, Range camera, Current Assisted Photo mixing Demodulator, CMOS image sensor.

Acknowledgement

Above all, I would like to express my gratitude to my supervisor **Prof. Gian-Franco Dalla Betta** for accepting me into his research group and also express my heartfelt thanks to him for his guidance, encouragement and continuous support during my graduate studies. His enthusiasm for teaching and research offered challenging opportunities to expand my scientific knowledge and my growing interest in the world of Photonics.

I would like to express my deep appreciation to **Dr. Lucio Pancheri** for sparing me countless hours of his precious time, useful discussions and suggestions during all the stages of my thesis work. I will always be grateful to him. I also wish to give my thanks to **Dr. David Stoppa** for his frank discussions and unique ideas.

I want to thank my fellow doctoral students in Nano & Micro Systems group for their helpful cooperations and assistance. I also thank all the colleagues at SOI group of FBK who contributed in their personal ways to carry out my Ph.D. thesis work.

I would like to express my sincere gratitude to **Prof. Giovanni Verzellesi**, University of Modena and Reggio Emilia and **Dr. Giuseppe Martini**, University of Pavia for accepting to review my thesis.

I want to thank Dr. S. Farazi Feroz and Mr. Shahin Reza for their help in proof reading of my dissertation. In overbearing times, I was lucky to have the support of all Bangladeshi students at the University of Trento which made my stay here in Italy much more fun and enjoying. I also thank all the administrative associates in Ph.D. office and Welcome office for their kind assistance and cheerful spirit.

This research work is partially supported by the Italian Ministry for Education, University and Research (MIUR), under the project PRIN07 N.2007AP789Y “Time of Flight Range Image Sensor (TRIS)” and by the European Community 6th Framework programmed within the project NETCARITY. I would like to thank all the members of FBK, Italy and UMC, Taiwan for their support in chip fabrication

Finally, I want to thank all my family members for their unconditional support all through out my life and academic career; special words of appreciation to my wife Nusrat for her encouragement, endless support and contribution in every aspect along the years. This thesis dissertation is dedicated to them.

TABLE OF CONTENTS

ABSTRACT	ii
ACKNOWLEDGEMENT	iii
TABLE OF CONTENTS	iv
LIST OF FIGURES	vii
LIST OF TABLES	x
CHAPTER 01: INTRODUCTION	1
1.1 Motivation	1
1.2 Thesis Objectives	2
1.3 Thesis Overview	3
CHAPTER 02: THEORETICAL OVERVIEW	5
2.1 Photon and photo sensing physics in semiconductors	5
2.1.1 <i>Description of light and photon</i>	5
2.1.2 <i>Energy band structure of semiconductors</i>	6
2.1.3 <i>Optical absorption in semiconductors</i>	7
2.1.4 <i>Photon-semiconductor interaction</i>	9
2.2 Silicon based photodetectors and light detection	10
2.2.1 <i>Photoconductor</i>	10
2.2.2 <i>Photodiode</i>	12
2.2.3 <i>Phototransistor</i>	13
2.2.4 <i>Photo-gate</i>	14
2.3 Different types of CMOS compatible photodiodes	15
2.4 Considerable parameters of photodetector	16
2.4.1 <i>Responsivity</i>	17
2.4.2 <i>Quantum efficiency</i>	17
2.4.3 <i>Response time</i>	17
2.4.4 <i>Leakage current</i>	18
2.4.5 <i>Capacitance</i>	18
2.4.6 <i>Noise</i>	19
2.5 Review of CCD and CMOS Image Sensor	20
2.5.1 <i>Charged-Coupled Device (CCD) Image Sensor</i>	20
2.5.2 <i>CMOS based Image Sensor</i>	23
2.5.3 <i>Comparison between CCD and CMOS Imagers</i>	24
2.6 Available technologies for Image Sensor	25
2.6.1 <i>CCD Image Sensor technology</i>	25
2.6.2 <i>CMOS Image Sensor technology</i>	25
CHAPTER 03: STATE OF THE ART OF 3D IMAGING	27
3.1 Different optical measurement techniques for 3D imaging	27
3.1.1 <i>Triangular method</i>	28
3.1.1.1 <i>Passive Triangular method</i>	28

3.1.1.2 <i>Active Triangular method</i>	29
3.1.2 <i>Interferometry</i>	30
3.1.3 <i>Time of Flight (TOF) method</i>	31
3.1.3.1 <i>Pulsed Modulation TOF technique</i>	33
3.1.3.2 <i>Continuous Wave (CW) modulation TOF technique</i>	33
3.1.3.3 <i>Pseudo-Noise modulation TOF technique</i>	34
3.1.4 <i>Comparison between the main optical techniques for range measurement</i>	35
3.2 <i>Time-of-Flight (TOF) based 3D vision sensors</i>	36
3.2.1 <i>Standard photodiode is coupled with complex processing circuit</i>	36
3.2.2 <i>Photo-demodulator fabricated with special technologies</i>	37
3.2.3 <i>Single Photon Avalanche Diode (SPAD) based Imager</i>	39
3.2.4 <i>Photo Mixing Device (PMD) based Imager</i>	39
3.2.5 <i>Gates-on-Field Oxide structure based CMOS Range Image Sensor</i>	41
3.2.6 <i>Field Assisted CMOS Photo-Demodulator based 3D imaging</i>	42
CHAPTER 04: TEST STRUCTURES AND CHARACTERIZATIONS	44
4.1 <i>High Resistivity Current Assisted Photo mixing Device (CAPD)</i>	44
4.1.1 <i>Device structure and operation of Linear-shaped CAPD</i>	44
4.1.2 <i>Characterization of Linear-shaped CAPD</i>	46
4.1.3 <i>Device structure, operation and characteristics of a Multiple-strip based CAPD</i>	48
4.1.4 <i>Non-linearity measurement of the Linear-shaped CAPD and Multi-tap CAPD</i>	51
4.1.5 <i>Device architecture and Operation characteristics of a Square shaped CAPD</i>	52
CHAPTER 05: CURRENT ASSISTED PHOTO MIXING DEMODULATOR IN STANDARD CMOS TECHNOLOGY	56
5.1 <i>Device Architecture</i>	56
5.2 <i>Operation principle and Charge transfer</i>	58
5.3 <i>Device performance and Experimental results</i>	60
5.3.1 <i>Device Characterizations</i>	61
5.3.1.1 <i>Measurement setup</i>	61
5.3.1.2 <i>Optical input and modulation signal</i>	62
5.3.1.3 <i>Static and Dynamic performance</i>	62
5.3.2 <i>Influence of wavelength on the device</i>	66
5.3.3 <i>Influence of modulation frequency on the device</i>	67
5.3.4 <i>Demodulation contrast vs. Modulation voltage of the device</i>	67
5.3.5 <i>Spectral Responsivity and Quantum Efficiency</i>	67
5.3.6 <i>Capacitance measurement</i>	69
5.3.7 <i>Phase linearity measurement of the device</i>	70
5.3.8 <i>Noise measurement</i>	72
5.4 <i>Device geometry and power consumptions</i>	73
CHAPTER 06: CAPD BASED 3D-IMAGING CAMERA IN STANDARD CMOS TECHNOLOGY	75
6.1 <i>Design of Photodemodulator Active Pixel Sensor (APS)</i>	75
6.2 <i>Simulation of Photodemodulator APS</i>	76

6.3 Layout design of an Active Pixel Sensor and its specifications	77
6.4 Photodemodulator Verilog simulations	78
6.5 Architecture of a 120×160 pixels Image Sensor	83
6.5.1 Column Amplifier	84
6.5.2 Double Delta Sampling (DDS)	85
6.5.3 Row and Column Decoder	86
6.6 Characterizations of a 120 ×160 pixels Image Sensor	87
6.6.1 System Description	87
6.6.1.1 Illumination module and Modulation driver	88
6.6.1.2 Light wavelength and power	89
6.6.1.3 Field of View	89
6.6.1.4 Diffuser	90
6.6.2 Correlation function measurement	90
6.7 Distance measurement setup	91
6.8 3D Range measurement and sample pictures	91
CHAPTER 07: CONCLUSION AND FUTURE WORKS	95
BIBLIOGRAPHY	97
APPENDIX-A	102
APPENDIX-B	105

LIST OF FIGURES

Fig. 1.1	Block diagram of 3D TOF ranging Imager.	1
Fig. 2.1	Electromagnetic Spectrum	6
Fig. 2.2	Simplified band structure of (a) GaAs (b) Si (c) Ge	7
Fig. 2.3	Semiconductor under incident light and exponential decay of photon power	8
Fig. 2.4	Absorption coefficient of some optoelectronic Semiconductors	8
Fig. 2.5	Photon-semiconductor Interaction process (a) Photon absorption (b) Photon stimulated emission	9
Fig. 2.6	Schematic diagram of a photoconductor with semiconductor slab and two ohmic contacts.	10
Fig. 2.7	Device configuration of a $p-n$ photodiode	12
Fig. 2.8	Schematic of a $p-n-p$ phototransistor	14
Fig. 2.9	Cross-sectional view of Photo-gate structure	15
Fig. 2.10	CMOS compatible photodiode structures	16
Fig. 2.11	Charged-Coupled Device (CCD) Cell	21
Fig. 2.12	Charge transfer process	21
Fig. 2.13	Area Array of CCD Architecture	22
Fig. 2.14	CMOS based pixel & pixel read out System	23
Fig. 3.1	Passive triangulation methods.	28
Fig. 3.2	Active triangulation methods	29
Fig. 3.3	Set up of Interferometry Method	31
Fig. 3.4	Time of Flight Principle	32
Fig. 3.5	Phase shift measurement techniques	33
Fig. 3.6	Relative resolutions of three types of 3D optical measurement method	35
Fig. 3.7	Pulsed I-TOF ranging Technique	37
Fig. 3.8	Cross sectional view of the CCD part (IG: integration gate PGL/PGM/PGR: left/middle and right photogate)	38
Fig. 3.9	Cross section of a pixel by Canesta Inc.	38
Fig. 3.10	SPAD pixel cross sectional view with Readout Circuit	39
Fig. 3.11	Schematic illustrates the cross-section of a PG-PMD receiver	40
Fig. 3.12	Cross-sectional view of finger structure MSM-PMD	41
Fig. 3.13	Gates-on-Field Oxide Structure based Imager (a) cross-sectional view and (b) layout design	41
Fig. 3.14	Schematic cross section of a Current Assisted Photonic Demodulator	42
Fig. 4.1	Cross sectional view of high resistivity linear-shaped CAPD	44
Fig. 4.2	Layout design of the linear-shaped CAPD	45
Fig. 4.3	Hole current density of linear shaped CAPD1	46
Fig. 4.4	DC Charge transfer characteristic of linear shaped CAPD1	47
Fig. 4.5	Dynamic Demodulation Contrast of CAPD1 at different Voltage	47
Fig. 4.6	Dynamic Demodulation Contrast of two CAPD devices at different geometries	48
Fig. 4.7	Cross sectional view of multiple strip CAPD and Device layout	49

Fig. 4.8	Hole current density of Multiple CAPD device	50
Fig. 4.9	DC characteristics of the device under the illumination of wide spectrum light	50
Fig. 4.10	Growth of demodulation contrast for multi-strip device as a function of different modulation voltage	51
Fig. 4.11	Phase linearity measurement (a) for Linear shaped CPAD1 (b) Multiple Strip CAPD	52
Fig. 4.12	Square shaped CAPD Device (a) Cross sectional View (b) Device layout (c) Hole current for square shaped CAPD	53
Fig. 4.13	DC current at the collection diode of device at two different ring voltages	54
Fig. 4.14	(a) Measured average current at two modulation frequencies (b) Measured Demodulation Contrast	55
Fig. 5.1	Device Cross sectional view of CMOS based CAPD (not to scale)	56
Fig. 5.2	(a) Cross-sectional view (b) 3D geometry of CAPD and (c) top view of the CAPD pixel. In (a) the SiO ₂ passivation layer is omitted.	57
Fig. 5.3	Simulated electron current density under illumination.	58
Fig. 5.4	(a) Single device layout (b) 10×10 pixel array layout and (c) Layout and Micro-photograph of the fabricated test structure.	60
Fig. 5.5	Experimental setup for (a) DC characterizations & (b) Dynamic characterizations	61
Fig. 5.6	Optical signal (a) Modulation signals for Laser and (b) Device Modulation Input.	62
Fig. 5.7	Simulated (solid line) and experimental (dotted line) DC characterizations of CAPD 10×10 array (a) DC current at the collecting electrodes I _{C1} and I _{C2} and total current I _{TOT} and (b) Corresponding charge transfer efficiency.	63
Fig. 5.8	Average current measured at collecting electrode at different modulation frequencies.	64
Fig. 5.9	Demodulation Contrast (a) Experimental and (b) simulated demodulation contrast as a function of modulation frequency. The laser wavelength is 650 nm.	65
Fig. 5.10	Demodulation Contrast as a function of the modulation frequency at two different wavelengths.	66
Fig. 5.11	Demodulation Contrast as a function of the modulation voltage for CAPD device.	67
Fig. 5.12	Test setup for spectral response characterization	68
Fig. 5.13	Responsivity vs. Wavelengths for CAPD	68
Fig. 5.14	Quantum efficiency vs. Wavelengths for CAPD	69
Fig. 5.15	Experimental set-up for capacitance measurement	69
Fig. 5.16	C-V response at different frequencies	70
Fig. 5.17	Measured and Real phase delay for (a) Sinusoidal wave (b) Square wave	71
Fig. 5.18	Phase linearity error vs. Applied phase in the case of sine-wave modulation and square-wave modulation	71
Fig. 5.19	Experimental set-up for shot noise measurement	72
Fig. 5.20	Noise Spectrum Density vs. Frequency	72
Fig. 5.21	Percentage of noise deviation vs. Frequency	73
Fig. 5.22	Simulated power vs. charge-transfer-efficiency (E_{CT}) curves for different modulation-electrode geometries. Simulated devices are minimum-size CAPD's (10×10 μm ² pixel).	74
Fig. 6.1	Pixel Circuit Schematic	75
Fig. 6.2	Simulation result of Photodemodulator APS	76
Fig. 6.3	Pixel circuit layouts	77
Fig. 6.4	Schematic of Verilog-CAPD devices	79
Fig. 6.5	I-V curve for Verilog CAPD	79

Fig. 6.6	(a) & (b) Pixel circuit configuration using Verilog-device model.	80
Fig. 6.7	Transient simulation of the pixel circuit using Verilog device model	82
Fig. 6.8	Imaging Chip Architecture	83
Fig. 6.9	Sensor micro-photograph	84
Fig. 6.10	Column Amplifier	85
Fig. 6.11	Double Delta Sampling (DDS)	86
Fig. 6.12	Row and Column Decoder	87
Fig. 6.13	3D measuring system block diagram.	88
Fig. 6.14	(a) Illumination module schematic diagram (b) Modulation driver schematic diagram.	88
Fig. 6.15	Micro Photograph of 3D imager with illumination module	89
Fig. 6.16	(a) Measured differential output as a function of applied phase. (b) Measured time delay as a function of applied time delay.	90
Fig. 6.17	TOF based measurement Set-up	91
Fig. 6.18	(a) Measured distance of a white diffusing target. (b) Measured distance precision	92
Fig. 6.19	Left: Distance map of two hands in front of a white diffusing target. Distance in meters is coded in gray levels. Right: Histogram of distance distribution	92
Fig. 6.20	Sample of 3D image	93
Fig. 6.21	Sample frames from a video acquired in 7 3D frames per second	93

LIST OF TABLES

Table-I	Summarized the comparative study between CCD and CMOS image sensor	24
Table-II	Comparison between three optical measurement systems	36
Table-III	Performance Comparison Table different types of 3D imager research	43
Table-IV	Pixel Summaries	78
Table-V	Illumination module Specifications	89
Table-VI	Sensor Summary	94

Chapter 01

Introduction

1.1 Motivation:

Range-imaging sensors accumulate large amount of three-dimensional (3D) coordinate data from visible surfaces in a scene and can be used in a large growing applications such as: positioning system, automobile guidance, security systems, obstacle detection and medical diagnosis. They are unique imaging devices in that the image data points explicitly correspond to scene surface geometry as sampled points. A new generation imager is designed to address concerns of compactness, speed and also consider the power, safety and cost limit of the system.

The importance of visual information to society is measured by the technological endeavour over millennia to record observed scenes on an independent medium. To capture an image, the electronics in a 3D imaging camera handle a considerable amount of image processing for colour imaging, image enhancement, compression control and interfacing. These functions are usually implemented with many chips fabricated in different process technologies. Presently, CMOS image sensor is capable of acting as a highly intelligent information collector by integrating image processing circuitry on the same chip.

Different types of image sensor design are broadly grouped into two categories: Charge Coupled Device (CCD) and Complementary Metal Oxide Semiconductor (CMOS) sensor. In CCD, the electric charge collected by the photo detector array during exposure time is serially shifted out of the sensor chip, thus resulting in slow readout speed and high power consumption. The key features in favour of the CMOS image sensor are lower power dissipation, cheaper fabrication, radiation tolerance and the ability to integrate other electronics in the sensor itself. Pixel size reduction can be achieved with CMOS transistor scaling but it has traditionally provided inferior image quality when compared to CCD due to noise and lower sensitivity, although this is improving.

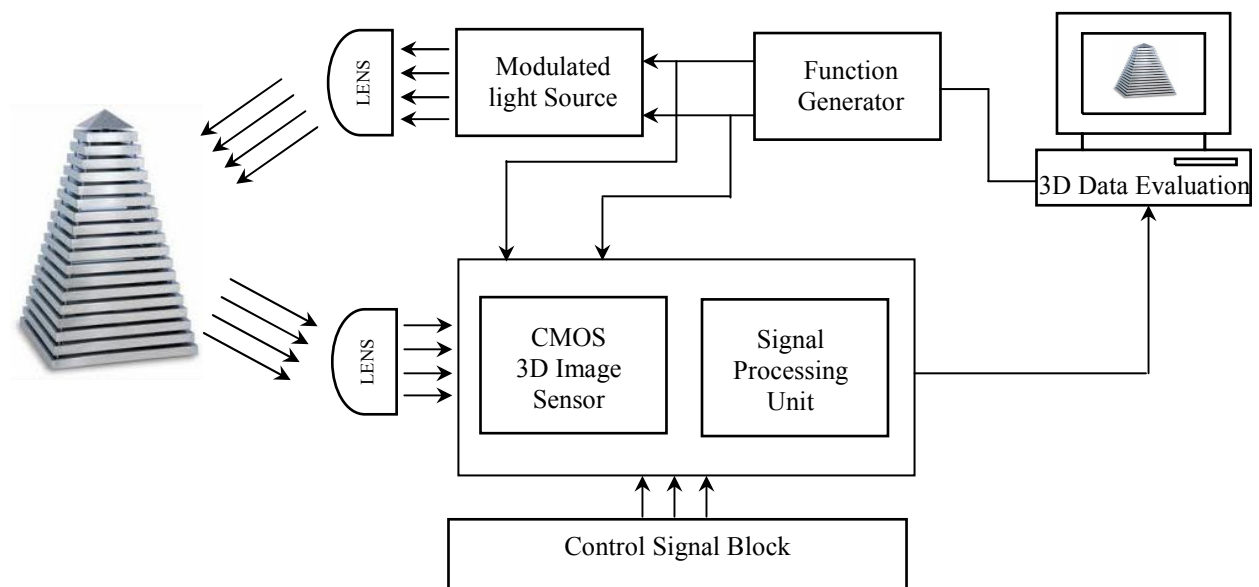


Fig. 1.1: Block diagram of 3D TOF ranging Imager.

One of the most exciting areas of CMOS imager's research is the integration of electronics with the sensor. Integration can be beneficial in two ways -- by integrating system functionally with the imager and several ICs can be replaced with a single chip camera. This reduces board design complexity and the cost of the system. These appealing advantages of CMOS 3D image sensors further expand their applications beyond traditional cameras into several fields such as PC cameras, mobile phones and automobiles. Fig. 1.1 shows the block diagram of a TOF based 3D CMOS Image Sensor.

The field of 3D optical imaging is based on three main techniques: triangulation, interferometry, and time-of-flight (TOF), using modulated and pulsed laser sources. All these methods have advantages and disadvantages and have widely been studied. Optical TOF rangefinders using highly collimated coherent light sources have been technologically feasible for decades. Such devices measure the distance of a target by calculating the time of an optical ray requires completing a round trip. Nowadays the field of 3D vision system is developing TOF based 3D image sensor because of the best performance of this technique in terms of acquisition speed, reliability and overall cost of the system.

Different types of photonic mixing devices have been proposed which employ the same demodulation principle, among them photo gate-PMD and metal-semiconductor-metal structures are implemented in CCD and hybrid CCD-CMOS technology. Other devices implemented in standard CMOS process technology have also been reported based on the modulation of multiple photo gates and inter-fingered photodiode structures. To enhance the photo detector properties, new emerging techniques have been introduced for specific functionality. This improves the device sensitivity, speed, demodulation bandwidth and allows gaining a large sensitive area. One very promising CMOS photonic demodulator based on substrate current modulation has recently been proposed; this device uses a modulated electric field to guide the photo generated charge carriers to different collection sites in the phase of modulation signal. The electric field penetrates deeper into the substrate, thus enhancing the charge separation and collection mechanism. A very good sensitivity and high demodulation efficiency can be achieved.

This thesis investigates the optical and electrical characteristics of a novel photodetector. A prototype imaging sensor is fabricated by using this device and the three dimensional distance measurement is determined. It is expected that the findings of this thesis can develop the performance of CMOS imagers and enabled them with the advantages of low power consumption, high integration and lower cost that can be realized in the imager market.

1.2 Thesis Objectives:

According to the state of art and the distance measurement system, the main concerns of this research is the realization of a TOF based (prototype) 3D CMOS image sensor which would explore a current assisted photo mixing demodulator (CAPD) having better performance in terms of the minimum pixel size, fill factor, maximum modulation frequency etc. The design will be followed by the characterization of both the developed device and the prototype camera. The main objectives and contributions of this thesis can be summarized as:

- i) Reviewing of the different types of optical techniques and TOF based 3D image sensors.
- ii) Design and characterization of a CAPD device to be applied in a TOF based 3D CMOS sensing system. For this purpose, different approaches are investigated. The device functionality is investigated using the finite element software ISE-TCAD in order to evaluate the capability of reaching the required high responsivity as well as high demodulation bandwidth of the device. Both DC and dynamic performance are simulated and optimized to reach the specific optical and electrical characteristics.
- iii) To get preliminary idea of the CAPD characteristics, different topological and geometrical structures are fabricated in a custom technology on the basis of the outcome of device simulation and the preliminary results. This technology is quite different from standard CMOS process technology, but it gives initial experience of the device characterizations that allows the simulations to be optimized.

iv) To improve the device performance, a CAPD is fabricated in a standard 0.18 μm CMOS process technology and a thorough characterization is carried out including electrical measurement of the test structures for the process parameters and electro-optical tests of the photo-demodulator. Critical parameters that is considered particularly: pixel area, fill factor, power consumption, demodulation efficiency, optical responsivity and maximum operating frequency.

v) The technological and physical parameters of the device simulator are tuned by exploiting the results of the test device chip. A good charge separation efficiency and demodulation capabilities are achieved up to modulation frequencies larger than 20 MHz. The impact of important parameters such as wavelength, modulation frequency and voltage on this test device is also experimentally evaluated.

vi) Finally, a prototype camera system with 120 \times 160 pixel array is fabricated, which is capable of providing real-time distance measurements of a scene through modulated-wave TOF measurements with a modulation frequency 20 MHz.

1.3 Thesis Overview:

The remaining portion of this thesis is organized as follows:

Chapter 2 is dedicated to a literature review, which describes the theory of photodetection in semiconductor devices, especially in CMOS compatible photodetectors, followed by a discussion of various CMOS compatible photosensor operation and comparing them in terms of their applicability in CMOS image sensor. It also gives a short overview and comparison of CCD and CMOS image sensors. To understand photodetector performance several conventional parameters including responsivity, quantum efficiency, leakage current, capacitance and noise sources are also described in this chapter.

Chapter 3 describes the basic operation principle as well as typical advantages and disadvantages of different optical measurement techniques and roughly compares Time-of-Flight measurement technique with other measurement principles--Interferometry and Triangulation methods. This chapter also discusses about the state of the art of TOF based 3D imagers for different types of photodetector used in the pixels and show the comparative study of several types of 3D image sensors that are reported in the literature.

Chapter 4 is devoted to describe the design and characterization of a current assisted photo mixing demodulator test structure that is fabricated in custom technology. Some photo demodulator test structures featuring of different topological, geometrical and process options have been designed and simulated by ISE-TCAD simulation software to understand the device functionality. Finally the electro-optical characterization of this test device is experimented.

Chapter 5 focuses on a current assisted photo mixing pixels having remarkably small pixel size of 10 \times 10 μm^2 designed and fabricated in 0.18 μm CMOS technology. In this chapter, the device charge separation efficiency and demodulation capabilities are described up to modulation frequencies larger than 20 MHz. The impact of important parameters such as wavelength, modulation frequency and voltage on this test device is also experimentally evaluated in this chapter.

Chapter 6 presents a detailed analysis on CMOS active pixel sensors. The pixel architecture and its schematic simulations are described in this chapter firstly. The description of the system architecture of CAPD ranging camera and the respective function modules of the ranging systems based on the CAPD device is explained. Finally, the results of some typical range measurements of the CAPD based prototype camera are presented.

Chapter 7 discusses the conclusions of the thesis and provides directions of the future work for further improvement of CMOS imagers.

Moreover, in the Appendices we describe some driver circuits that we used in the measurement setup for various experimental investigations and also define some useful terminology based on the image sensor.

Appendix-A 3D image sensor based terminology

Appendix-B Pseudo Differential Amplifier & Laser Driver Circuit

During my Ph.D. research activities it was possible to use some part of the scientific results of this dissertation in the following publications and conference presentations:

- [01] Gian-Franco Dalla Betta, Silvano Donati, Quazi Delwar Hossain, Giuseppe Martini, Lucio Pancheri, Davide Saguatti, David Stoppa, Giovanni Verzellesi, “Design and Characterization of Current Assisted Photonic Demodulators in 0.18- μm CMOS Technology” *IEEE Transactions on Electron Devices*, Submitted 26.08.2010.
- [02] G.-F Dalla Betta, Q.D.Hossain, S.Donati, G.Martini, M. Fathi, E.Randone, G.Verzellesi, D.Saguatti, D.Stoppa, L.Pancheri and N.Massari, “Dispositivo per la Ripresa di Immagini 3D Basato su Tecnologia CMOSnm e Telemetria a Modulazione Sinusoidale.(Device for the recovery of 3D images based on 180nm CMOS technology and Sinusoidal Telemetry)” *12th National Conference on Photonic Technology*, Photonics 2010, Pisa,Italy, 25-27 May 2010.
- [03] Quazi Delwar Hossain, Gian-Franco Dalla Betta, Lucio Pancheri, David Stoppa, “A 3D Image Sensor based on Current Assisted Photonic Mixing Demodulator in 0.18 μm CMOS Technology” 6th International Conference on Microelectronics & Electronics,Prime’2010, IMST GmbH, Berlin, Germany, ISBN number:978-3-9813754-1-1.
- [04] Lucio Pancheri, David Stoppa , Nicola Massari, Mattia Malfatti, Lorenzo Gonzo, Quazi Delwar Hossain, Gian-Franco Dalla Betta “A 160 \times 120 pixel CMOS range image sensor based on current Assisted photonic demodulators” SPIE Europe conference’2010, *SPIE Conference proceedings*, volume 7726, 772615(1-9) Brussels, Belgium, 2010.
- [05] Quazi Delwar Hossain, Gian-Franco Dalla Betta, Lucio Pancheri, David Stoppa, “Current Assisted Photonic Mixing Demodulator implemented in 0.18 μm Standard CMOS Technology”, 5th International Conference on Microelectronics & Electronics,Prime’2009, *Conference proceedings, IEEE* catalog Number: CFP09622-PRT, ISBN 978- 1-4244-3732-0 Page 212-215 University College Cork, Ireland.

Chapter 02

Theoretical Overview

Single-crystal semiconductors have a significant place in optoelectronics, a large number of optoelectronic devices consist of a *p*-type and *n*-type region, just like a regular p-n diode. The key difference is that there is an additional interaction between the electrons and holes in the semiconductor and light. The microscopic interaction between carriers and photons leading to photon absorption or emission and correspondingly to electron–hole (e-h) pair generation or recombination. In this chapter we start from the light and photon, energy band structure of semiconductors and explain the concept of interaction between light and semiconductor. We also show the different types of photodetectors and their performance parameters and finally we will discuss about the CCD and CMOS based image sensor in the following chapter.

2.1 Photon and Photo sensing physics in semiconductors:

When an electromagnetic wave hits a material surface, the photon interacts with matter, which contains electric charges. Regardless of whether the wave is partially absorbed or reflected, the electric field of light exerts forces on the electric charges and dipoles in atoms, molecules and solids, causing them to vibrate or accelerate. On the contrary, the vibrating electric charges emit light. We know from the quantum mechanics of principle- atom, molecules and solids have specific allowed energy band. A photon may interact with an atom if its energy matches with the difference between two energy levels. When the photons impart their energy to the atom and raising it to a higher energy level, it is said that the photon is absorbed. Then again, the atom can undergo a transition to a lower energy level thus resulting in the emission of a photon. In this section, we will briefly discuss about light and photon, the semiconductor structure and effect of light on semiconductors.

2.1.1 Description of light and photon:

Light is an electromagnetic radiation of wavelength that propagates in space and time. It carries radiant energy and exhibits properties of both wavelike and particle-like in space. The electromagnetic wave is periodic and propagates in a straight line with the speed of light (*c*) in a homogeneous medium. Given that the wavelength is λ , so the frequency *f* can be expressed by the relation-

$$f = \frac{c}{\lambda} \dots \dots \dots 2.1$$

Light consists of quantum particles called photons. Photons have zero rest mass, carry electromagnetic energy and momentum. They also carry an intrinsic angular momentum that directs its polarization properties. The photon can travel at the speed of light in vacuum but its speed is retarded in matter. The amount of energy carried by a photon along with an electromagnetic wave is E_{ph} that relates with its frequency *f* and wave length λ .

$$E_{ph} = h.f = h \frac{c}{\lambda} \dots \dots \dots 2.2$$

where *h* is the Planck’s constant [01]. This equation shows that the photon energy depends on its frequency. The interaction between an electromagnetic wave and a semiconductor can be analyzed at several levels. Fig. 2.1 shows the electromagnetic spectrum where energy decreases with respect to the increase of wavelength. Different types of semiconductors used in photo-detector are Silicon (Si), Germanium (Ge), Cadmium Zinc Telluride (CdZnTe), Gallium Nitride (GaN) etc [02]. This thesis concentrates on the basic mechanism of photo-detection using silicon for the visible light spectrum. The

Interaction between the photons and silicon is concerned with the attenuation of the incident beam as it penetrates through the semiconductor and the most important forms of interaction include absorption, refraction, transmission, angle and diffraction.

For each material, different wavelengths of optical signal are absorbed over different penetration depths. Thus different types of detector materials respond to specific spectral ranges. Another band is the frequency range corresponding to radio waves, micro waves or even millimeter waves. High speed electronic devices and circuits of the optoelectronic systems operate in this range.

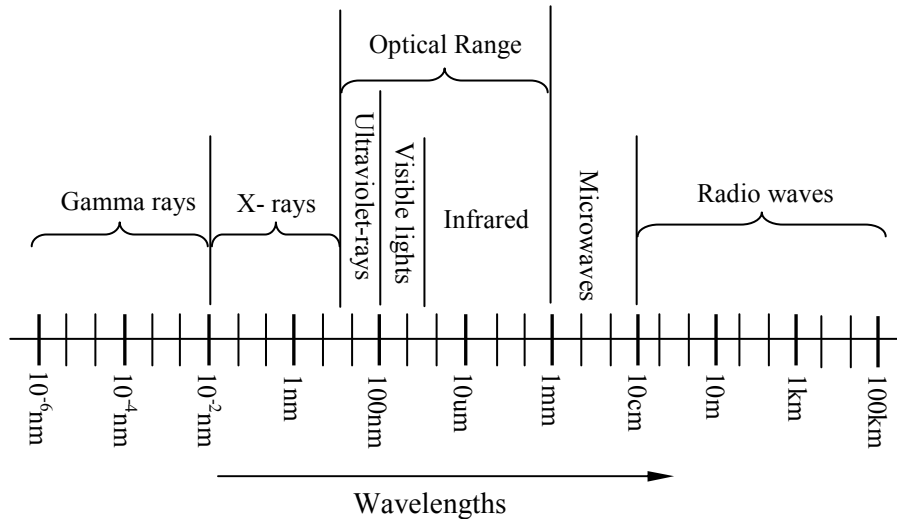


Fig. 2.1: Electromagnetic Spectrum

2.1.2 Energy band structure of semiconductors:

The energy regions of semiconductors take the form of groups of closely spaced levels that form bands. At the thermal excitation T=0K these bands are either completely occupied by electrons or completely empty. The highest filled band i.e. the lower energy band is called the valance band. The upper energy band; which is empty is called the conduction band. The separation between the energy of the highest valance band and that of the lowest conduction band is called the band gap E_g . The energy band gap plays an important role to determine the optical and electrical properties of the semiconductor materials. The band structure of a crystalline solid can be characterized by the energy-momentum (E-p) relationship in free space as follows:

$$E = \frac{p^2}{2m_0} = \frac{\hbar^2 k^2}{2m_0} \dots \dots \dots (2.3)$$

where p is the magnitude of the momentum and k is the magnitude of the wave vector $k = p/\hbar$ associated with the electrons wave function and m_0 is the electron mass.

The semiconductors in which the valance band maximum and the conduction band minimum correspond to the same momentum are called the direct band gap materials. On the other hand semiconductors in which this is not maintained are known as indirect band-gap materials. An indirect band gap requires a substantial change in the electron momentum. The direct band gap materials are often explain electronic and optical behaviour of a semiconductor. Gallium Arsenide (GaAs) is a typical example of direct band gap material and able to interact directly with photon. In GaAs, to promote an electron from valance band to conduction band, an energy larger than the band gap has to be provided but momentum is negligible. Since the interaction involves only one electron and one photon, the interaction probability is high. On the other hand, in Silicon (Si) the valance band and the conduction band maintain indirect-band gap. The Photon interaction leading to band-to-band processes requires a substantial amount of momentum. It also

maintains a direct band gap with high energy of 3.4eV. Germanium (Ge) has an indirect-band gap at the lowest conduction band point where the energy is 0.66 eV, but a direct band gap is also available with high energy of 0.9eV. The typical transport properties of Ge are as like as the indirect-band gap materials but optical properties can be influenced by the fact that high-energy photons can excite electrons directly from valance band to conduction band. Fig. 2.2 shows the simplified band structure of GaAs, Si and Ge. Many compound semiconductor families can be classified in direct and indirect band gap. For examples, compounds GaAs, InP, GaSb, InAs are the direct band gap materials and AlAs, GaP are indirect ones. These compound semiconductors are used for high-frequency electronics and optoelectronics.

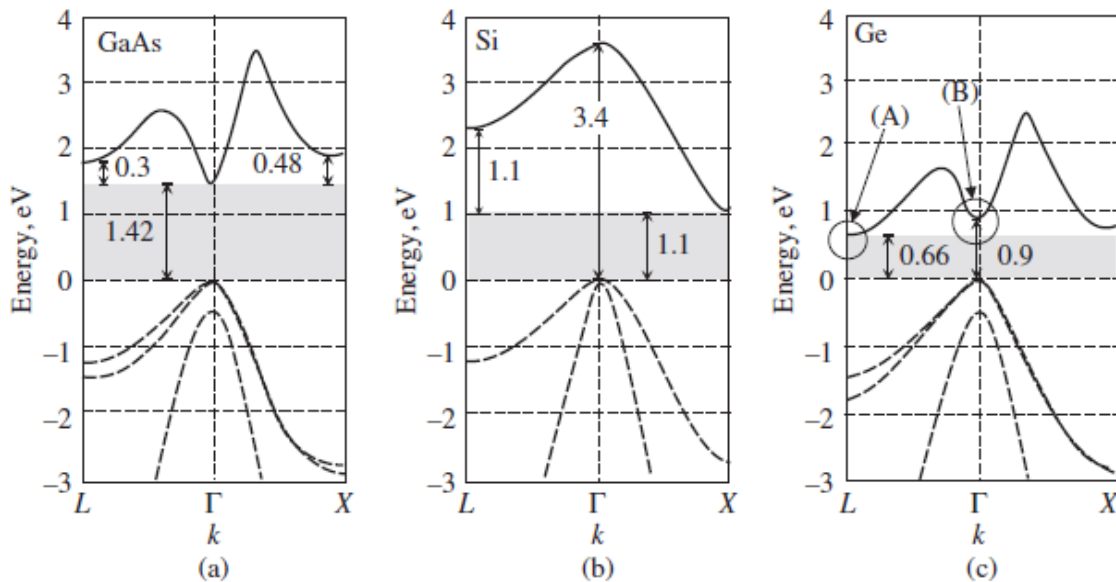


Fig. 2.2: Simplified band structure of (a) GaAs (b) Si (c) Ge [01]

2.1.3 Optical absorption in semiconductors:

In order for a semiconductor device to be useful as a detector, some property of the device should be affected by radiation. The most commonly used property is the conversion of light into electron-hole pairs. When light impinges on a semiconductor, it can scatter an electron in the valence band into conduction band. This process is called the absorption of a photon. In order to take the electron from the fully occupied valence band to the empty conduction band, the photon energy must be at least equal to the band gap of the semiconductor.

For silicon, when incident light impinges some portion of the original optical power is reflected due to the index of refraction change at the surface. The remaining light enters the silicon piece and gets absorbed by the material such that the amount of power decays exponentially from the surface. If $I(x)$ represents the power of the optical signal at depth x from the surface, $I(0)$ is the power level that enter the silicon surface. $I(x)$ is related to $I(0)$ by the Beer-Lambert law [03]:

$$I(x) = I(0)e^{-\alpha x} \dots \dots \dots (2.4)$$

where α is the absorption coefficient (m^{-1}) and is a function of the wavelength of the optical signal and x is the thickness of the semiconductor. α decreases as wavelength increases but in general α cannot be mathematically computed easily. A shorter wavelength signal at the blue end of the visible spectrum in fact might be more difficult for a photo-detector to sense depending on the design and architecture of the detector. We know that, the absorption of photons entering the semiconductor material is a statistical process and photon-absorption sites are statistically distributed with an exponential dependence of distance from the semiconductor surface and wavelength of the incoming light. The distance where an

amount of 37% of the total photon flux is already absorbed is called the *penetration depth* (L_α). That is the inverse of the *absorption-coefficient* α [01]. So we can write the above equation as:

$$I(x) = I(0)e^{-\frac{x}{L_\alpha}} \dots \dots \dots (2.5)$$

Fig. 2.3 shows the exponential attenuation of photon power.

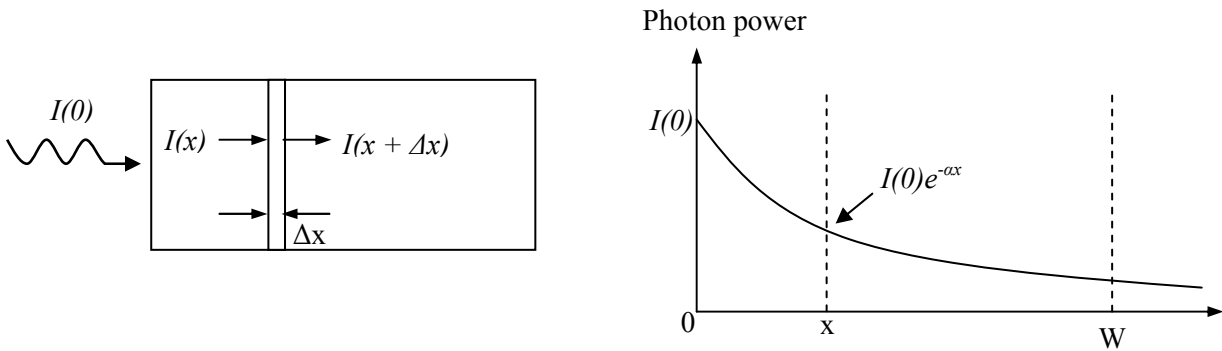


Fig.2.3: Semiconductor under incident light and exponential decay of photon power

Fig.2.4 shows the absorption spectra of a few semiconductors that are used for optoelectronic applications. In this figure, the band gap energies are indicated, along with the wavelength. The absorption coefficient drops off sharply at the band-gap energy, indicating negligible absorption for photons with energy smaller than E_g [04]. Thus, silicon absorbs photons with $\lambda \leq 1.1 \mu\text{m}$ and GaAs absorbs photons with $\lambda \leq 0.9 \mu\text{m}$.

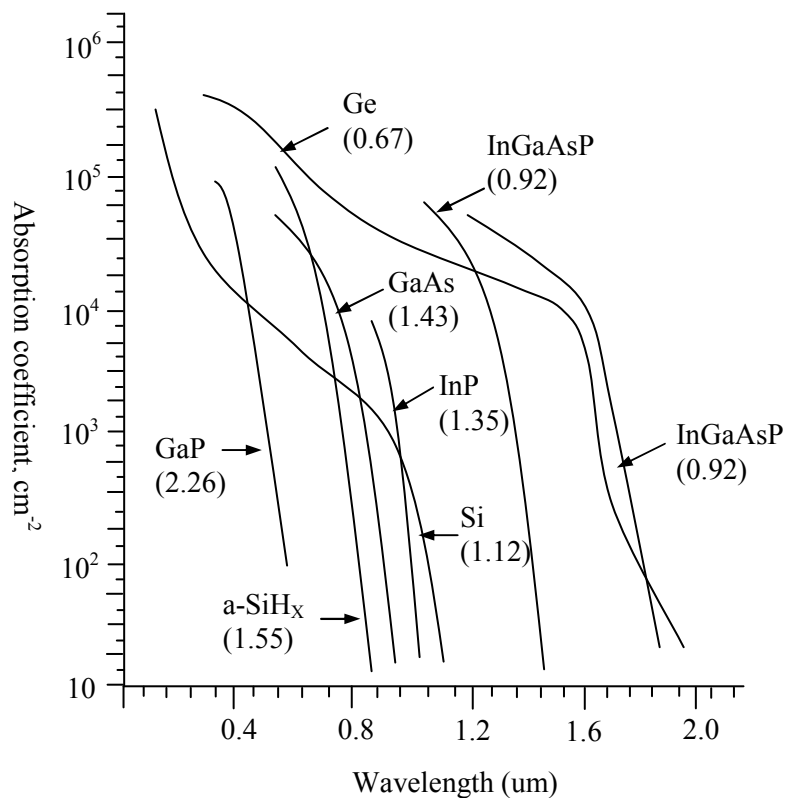


Fig. 2.4: Absorption coefficient of some optoelectronic Semiconductors

2.1.4 Photon-semiconductor interaction:

At a microscopic level, semiconductors are containers of charged particles (electrons and holes) that interact with the EM wave photons. We know, an EM wave with frequency f is interpreted as a collection of photons of energy $E_{ph} = hf$. The magnitude of the photons momentum is $2\pi/\lambda$. The possibility of interaction is quite obvious, since charged particles in motion are subject to the Coulomb force (EM wave electric field) and to the Lorentz force (magnetic field of the EM wave). The useful semiconductor response is dominated by the ability of radiation to cause band-to-band carrier transitions with corresponding emission or absorption of a photon. Equation 2.2 is the Planck's law, where a useful relation exists between the EM photon energy and the related wavelength.

$$E_{ph} = \frac{hc}{\lambda} = \frac{4.136 \times 10^{-15} eV_s \cdot 2.998 \times 10^8 m/s}{\lambda \times 10^{-6}} = \frac{1.24}{\lambda|_{\mu m}} eV \dots \dots \dots (2.6)$$

In the EM wave and semiconductor interaction, three cases are possible according to the value of photon energy E_{ph} and the energy band gap E_g when $E_{ph} < E_g$, as in RF, Microwave and far infrared, the interaction is weak and does not involve band-to-band processes but only the dielectric response and inter band processes, called free electron/hole absorption. If $E_{ph} \approx E_g$ and $E_{ph} > E_g$ as in the near infrared, visible light and ultra violet ray; in this case light interacts strongly through band-to-band processes leading to the generation of e-h pairs. Finally when $E_{ph} \gg E_g$, as for X-rays; high-energy ionizing interactions take place i.e., each photon causes the generation of a high-energy e-h pair which generates a large number of electron-hole pairs through avalanche processes. This case is exploited in high-energy particles and radiation detectors.

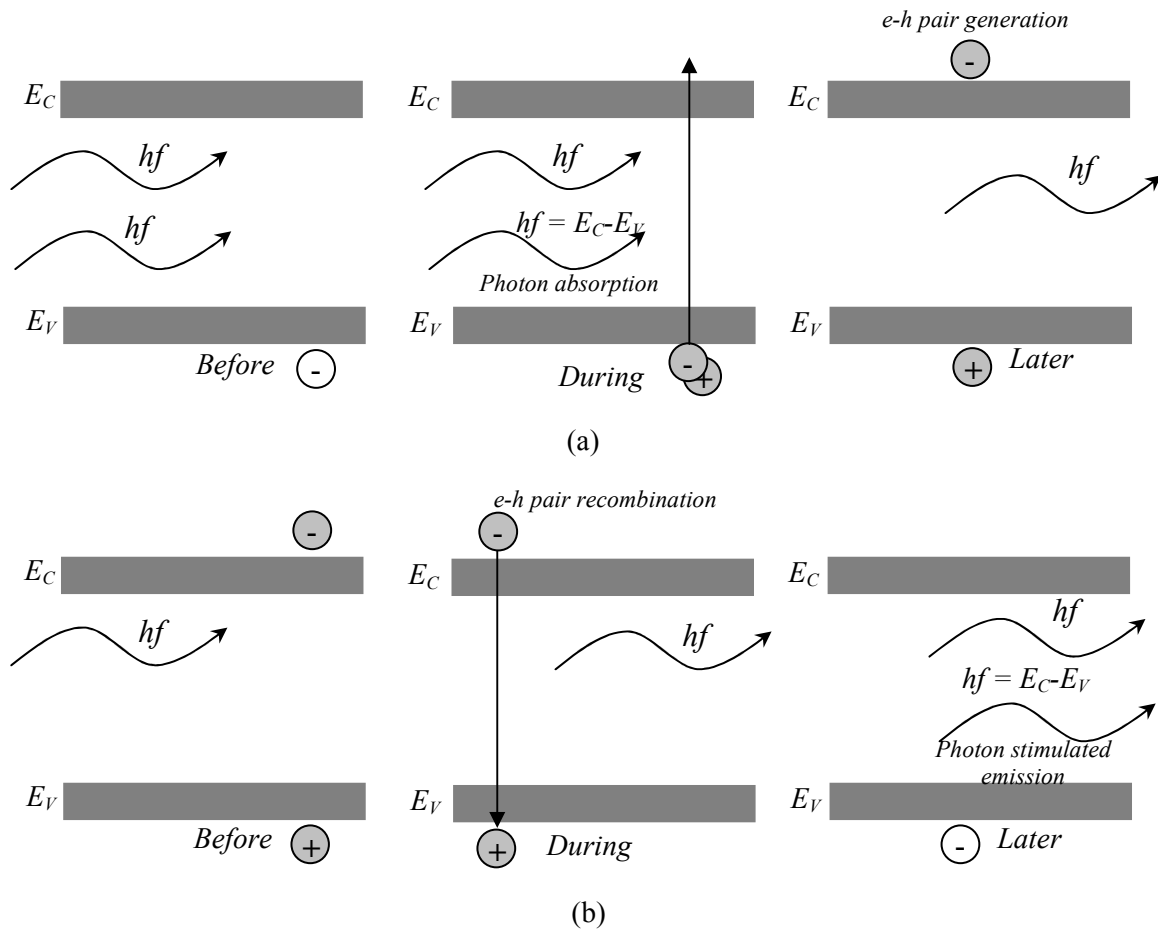


Fig. 2.5: Photon-semiconductor Interaction process (a) Photon absorption (b) Photon stimulated emission

In EM wave- semiconductor interaction, optical processes leading to band-to-band transitions involve at least one photon and one e-h pair. There are three basic processes: In photon absorption process; the photon energy is supplied to a valence band electron, which is promoted to the conduction band, leaving a free hole in the valence band. Because of the absorption process, the EM wave decreases its amplitude and power.

In photon stimulated emission process, a photon stimulates the emission of a second photon with the same frequency and wave vector; the e-h pair recombines to provide the photon energy. The emitted photon is coherent with the stimulating EM wave, i.e. it increases the amplitude of the EM field and the EM wave power through a gain process. The above Fig. 2.5 shows the photon-semiconductor interaction processes. Finally, photon spontaneous emission process, a photon is emitted spontaneously; the e-h pair recombines to provide the photon energy. Since the emitted photon is incoherent, the process does not imply the amplification of an already existing wave, but rather the excitation of an EM field with a possibly broad frequency spectrum.

2.2 Silicon based photodetectors and light detection:

A photodetector is a semiconductor device that can detect an optical signal and transduce into an electronic signal. The physical operation phenomena of the photodetector is as follows: (a) optical generation of free electron-hole pairs due to the absorption of incident light (b) the photo generated electron- hole pairs are then separated and collected by the external circuit with considerable gain. The current through the detector in the absence of light is called dark current. Dark current must be accounted for by calibration if a detector is used to make an accurate optical power measurement and it is also source of noise when used in optical communication systems. The figures of merit of a photodetector are photosensitivity of light at various wavelengths, response time, detector noise, dynamic range and so on.

The photodetectors are very important in various fields of applications such as: optical communication, digital photography, spectroscopy, night vision equipment and laser range finder. In this section different types of silicon-based photodetectors - photoconductor, photodiode, phototransistor and photo-gate are briefly described.

2.2.1 Photoconductor:

A photoconductor is a semiconductor light detector consisting of a piece of semiconductor with two ohmic contacts at opposite ends of the device. Fig. 2.6 shows the schematic diagram of a photoconductor [03]. Under illumination, the incident light passes through the material thus generating carriers and increasing the conductivity of the semiconductor.

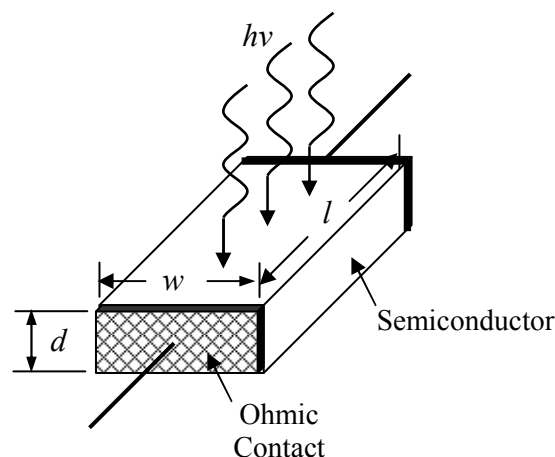


Fig. 2.6: Schematic of a photoconductor with semiconductor slab and two ohmic contacts.

The increase of conductivity under illumination is mainly due to the increase in the number of carriers. These carriers are generated either by the process of intrinsic or extrinsic photoexcitations. Consequently, the current flowing through the device in response to an applied voltage is a function of the incident optical power density P'_{opt} .

The performance of a photodetector is measured in terms of quantum efficiency, response time and sensitivity. Carriers in a semiconductor recombine at the rate $n(t)/\tau$, where $n(t)$ is the carrier concentration and τ is the lifetime of the carriers. At time zero, the number of generated carriers in a unit volume is n_0 . After time t in the same volume the number of generated carriers decay by recombination as $n = n_0 \exp(-t/\tau)$. For the monochromatic illumination the photon flux impinging uniformly on the surface of the photoconductor with area $A=WL$, where W and L is the width and length of the photodetector respectively. The generation rate of electron-hole pairs per unit volume is proportional to the optical power density and at the steady state the carrier generation rate must balance the recombination rate. Therefore,

$$R = \frac{\Delta p}{\tau} = \frac{\Delta n}{\tau} = G = \frac{\eta P'_{opt} WL}{\hbar \omega LWH} \dots \dots \dots (2.7)$$

where Δp and Δn are the generated hole and electron densities by photon absorption and H is the height of the photoconductor. These carriers increase the conductivity by $\Delta\sigma$,

Now,
$$\Delta\sigma = q\mu_n\Delta n + q\mu_p\Delta p \dots \dots \dots (2.8)$$

where μ_n and μ_p are the electron and hole mobility. For an applied voltage V_b , the photogenerated current density ΔJ is

$$\begin{aligned} \Delta J = \Delta\sigma \frac{V_b}{l} &= \left(\frac{q\mu_n\eta P'_{opt} WL\tau}{\hbar\omega LWH} + \frac{q\mu_p\eta P'_{opt} WL\tau}{\hbar\omega LWH} \right) \frac{V_b}{L} \\ &= \frac{q\eta P'_{opt}\mu_n}{\hbar\omega H} \left(1 + \frac{\mu_p}{\mu_n} \right) \frac{V_b\tau}{L} \dots \dots \dots (2.9) \end{aligned}$$

Now the induced current ΔI is the current density time the cross-sectional area of the photoconductor:

$$\Delta I = \Delta JWH = \frac{q\eta P'_{opt} W\mu_n}{\hbar\omega} \left(1 + \frac{\mu_p}{\mu_n} \right) \frac{V_b\tau}{L} \dots \dots \dots (2.10)$$

The primary photocurrent can be defined $I_{opt} = \eta q P_{opt} / \hbar \omega$, where; $P_{opt} = P'_{opt} LW$ is the total optical power impinging on the detector. Now the light induced current ΔI relates with the primary photocurrent, the carrier life time and bias voltage. It also inversely proportional to length can be expressed as the following:

$$\begin{aligned} \Delta I = I_{opt} \left(1 + \frac{\mu_p}{\mu_n} \right) \frac{V_b\mu_n\tau}{L^2} &= I_{opt} \left(1 + \frac{\mu_p}{\mu_n} \right) \frac{\mu_n E \tau}{L} \\ &= I_{opt} \left(1 + \frac{\mu_p}{\mu_n} \right) \frac{V_b\tau}{L} = I_{opt} \left(1 + \frac{\mu_p}{\mu_n} \right) \frac{\tau}{t_r} \dots \dots \dots (2.11) \end{aligned}$$

where t_r is the average time required for a carrier to pass through the length of the device called transit time [02]. The gain of the device is the rate of incremental light induced current ΔI to the primary current I_{opt} . The gain G depends on the lifetime of carriers relative to their transit time. The gain can assume a broad range of values, both below and above unity, depending on the parameters of the materials, size of the device and applied voltage. The gain of a photoconductor cannot generally exceed 10^6 , because of the constraint enforced by space charge limited current flow, impact ionization and dielectric breakdown.

2.2.2 Photodiode:

The photodiode is an important photo sensor for digital imaging, analytical instrumentation, laser range finder, optical communication and so on. A planar diffused silicon photodiode is simply a p-n junction diode. It can be formed by diffusing either an n-type impurity into a p-type bulk silicon wafer or a p-type impurity into an n-type bulk silicon wafer. The inter diffusion of electrons and holes between the n and p regions across the junction introduces a region with no free carriers, this is called depletion region. Any applied reverse bias can be added to increase the depletion region width. When light irradiates into a diode junction the electron-hole pairs are generated and swept away by drift in the depletion region and are collected by diffusion from the un-depleted region. The generated current is proportional to the incident light or radiation power. Fig. 2.7 shows a simple *p-n* photodiode.

The quantum efficiency of photodiode is one of the most important figures of merit. For larger quantum efficiency the depletion layer of the photodiode must be thick in order to take up as many photons as possible. On the other hand the thicker depletion layer increase carrier transit time, so the thickness of the depletion layer should be carefully chosen to achieve the best trade-off between the quantum efficiency and response time. The response speed of a photodiode is much faster than that of photoconductor due to the strong electric field inside the depletion region. Three factors limit the response speed of a photodiode: the diffusion time of carriers outside the depletion layer, the drift time inside the depletion layer and the capacitance of the depletion region.

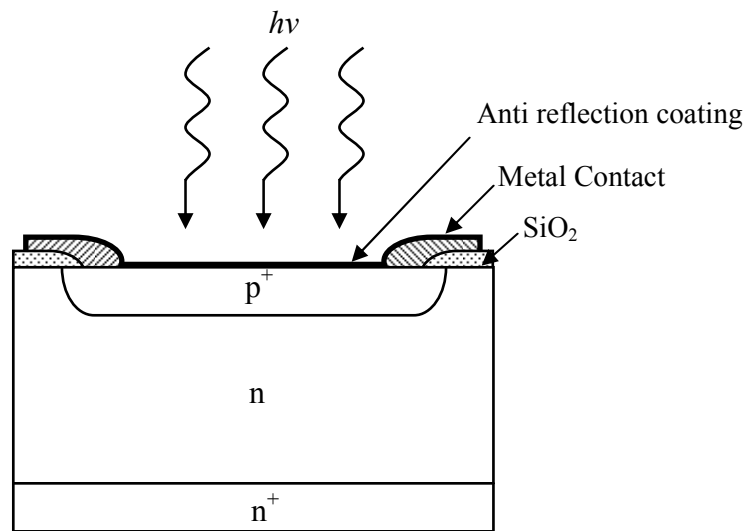


Fig.2.7: Device configuration of a *p-n* photodiode

Silicon photodiode can be operated in three different modes of operation: photovoltaic mode, photoconductive mode and integrating mode. In the photovoltaic mode the photodiode is unbiased; while for the photoconductive mode an external reverse bias is applied. Integrating mode is also known as storage mode; initially the photodiode is reverse biased then leaving it floating and making the photo charge be integrated onto the photodiode capacitance. The mode of selection depends upon the speed requirements of the application and the amount of dark current that is tolerable. In the photovoltaic mode

dark current is at a minimum level, on the other hand photodiodes exhibit their fastest switching speeds when operated in photoconductive mode.

Typically the photodiodes are operated in the photoconductive mode with reverse bias condition. Under the illumination, photons are absorbed everywhere with respect to absorption coefficient and the photocurrent is generated. The total photocurrent consists of drift current and diffusion current. The drift current produced due to the carriers generated inside the depletion layer. On the other hand the diffusion current is produced due to carriers generated outside the depletion region that diffuse into the reverse biased junction. Both generated photocurrents are dependent on the incident photon flux; therefore, the steady-state current density through the reverse-biased depletion layer can be expressed as

$$J_{total} = J_{drift} + J_{diffusion} \dots \dots \dots (2.12)$$

In the case of *p-n* diode, the two components of the photocurrent can be expressed from the electron-hole generation rate as:

$$G(x) = \phi_0 \alpha e^{-\alpha x} \dots \dots \dots (2.13)$$

where ϕ_0 is the incident photon flux per unit area given by $P_{opt} (1 - R) / A \hbar \omega$, where R is the reflection coefficient and A is the device area. So the drift current J_{drift} and the diffusion current $J_{diffusion}$ can be expressed as:

$$J_{drift} = q \phi_0 [1 - \exp(-\alpha W_d)] \dots \dots \dots (2.14)$$

and,

$$J_{diffusion} = q \phi_0 \frac{\alpha L_p}{1 + \alpha L_p} \exp(-\alpha W_d) + q P_{n0} \frac{D_p}{L_p} \dots \dots \dots (2.15)$$

So the total current density J_{total} which is the sum of drift and diffusion current densities turns out to be

$$J_{total} = q \phi_0 \left[1 - \frac{\exp(-\alpha W_d)}{1 + \alpha L_p} \right] + q P_{n0} \frac{D_p}{L_p} \dots \dots \dots (2.15)$$

where α is the absorption co-efficient, W_d is the depletion width and L_p , D_p and P_{n0} are the hole diffusion length, diffusion co-efficient and equilibrium minority-carrier concentration in the n-type region respectively [01]. In the absence of optical illumination, a current also flows as a result of leakage current is generally called dark current I_{dark} . Three different contribution phenomena are responsible for this dark current: firstly the contribution comes from the thermal generation of charge carriers within the depletion region, secondly, the diffusion of the minority carriers from the quasi-neutral region to the depletion region can drive the leakage current and finally the contribution is due to the generation of carriers to the depleted surface beneath the SiO_2 passivation layer.

For a planar photodiode, the active area is defined photo-lithographically after the pattern is etched through the initial oxide passivation layer. In the case of surface preparation some surface damage leaves which reduces the collection efficiency of the device. An additional oxide passivation layer is grown over the active area of the photodiodes to form an anti reflection coating. The photodiode response can be enhanced up to 25% by adjusting the anti-reflection coating to a particular wavelength, thus the photodiode performance can be increased.

2.2.3 Phototransistor:

A phototransistor is in essence nothing more than a bipolar transistor. It differs from a conventional bipolar transistor by having much larger base and collector area as the photon collecting element. These devices are generally made using diffusion or ion implantation. Phototransistor provides high levels of

gain and standard devices are low cost and can be used in many applications. Fig.2.8 shows the schematic of a p-n-p bipolar phototransistor. The collector-base junction area is large to increase the collection of photons. These devices are operated with the base terminal floating. The light enters the base-collector region of the device where it causes hole-electron pairs to be generated. The photogenerated holes in the reverse biased base-collector junction will be swept in to the collector and collected as photocurrent I_{ph} . The emitter-base potential is raised by electrons generated in the base region and swept into the base from the collector. The increase of emitter-base junction potential causes holes from the emitter to be injected into the base and pass through it by diffusion and appear as additional collector current [03]. Since the base is floating the emitter current I_E is equal to the collector current I_C as shown below:

$$I_C = I_E = I_{CEO} = (1 + h_{FE})(I_{ph} + I_{eq}) \dots \dots \dots (2.16)$$

where h_{FE} is the static common emitter current gain, I_{eq} represents the background current and dark current. I_{CEO} is the collector-emitter current open base

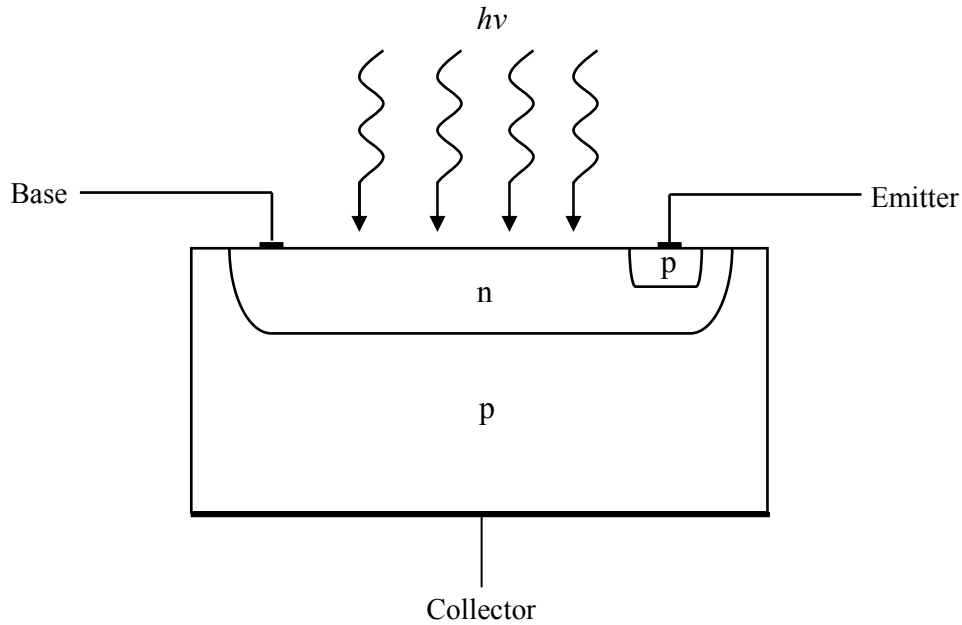


Fig.2.8: Schematic of a p-n-p phototransistor

The gain of the phototransistor is $(1+h_{FE})$, thus the effective quantum efficiency is $(1+h_{FE})$ times larger than that of the base-collector photodiode. As already mentioned the phototransistor has a high level of gain resulting from the transistor action. For homo-structure this may be the order of about 50 up to a few hundred [05]. However for the hetero-structure devices the levels of gain may rise to ten thousand. The response speed of the phototransistor is slow in comparison with the photodiode because of the large depletion capacitance from the large collector-base junction area.

2.2.4 Photo-gate:

The Physical basis of MOS photo-gate employs the principle of operation of CCD concerning integration transport and readout inside each pixel [01]. These devices can be either NMOS photo-gate or PMOS photo-gate depending on the fabrication process used. The photo-gate detector is a MOS capacitor with polysilicon at the top terminal and consists of a photo-gate (PG) with a floating diffusion (FD) output separated by a transfer gate (TX). Fig.2.9 shows the cross-sectional view of a photo-gate. The photo-gate transfer optical signals into stored charges rather than voltage or current signals. The stored charges subsequently interact with other components to generate voltage or current signals. When a positive

voltage is applied to the gate above the p-substrate, holes are pushed away from the surface and underneath of the photo-gate a depletion layer is formed. The photo-gate has different mode of operation. When no free charge carriers are available the depletion region extends deep into the semiconductor resulting in a deep space charge region. With the optical generation of electron-hole pairs free charge carriers become available. The electron-hole pairs are separated in such a way that the minority carriers, i.e. electrons are collected at the semiconductor surface while majority carriers, i.e. holes are rejected into the semiconductor bulk, where they recombine after a certain time [03].

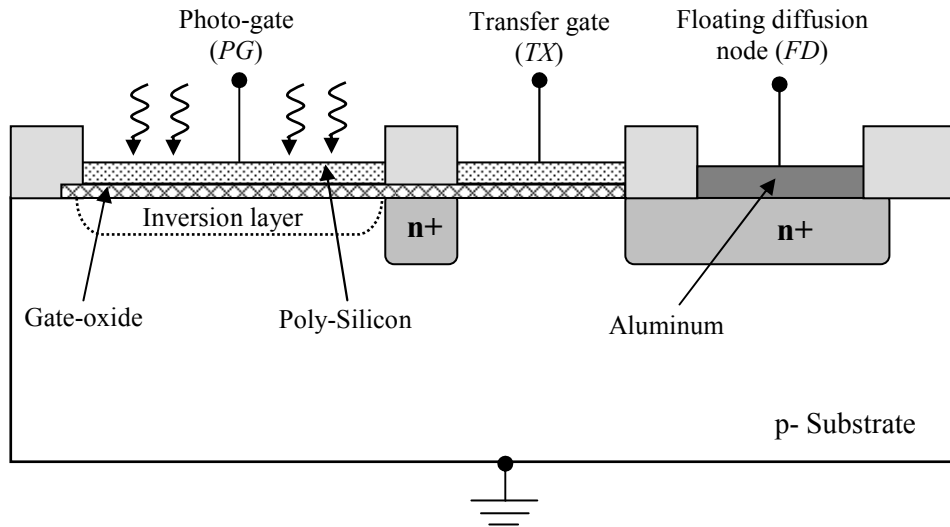


Fig.2.9: Cross-sectional view of Photo-gate structure

The electrons begin to form an inversion layer and at the same time decrease the depth of the space charge region, thus integrating the optically generated electrons. At the mode of strong inversion no more free charge carriers can be held by the MOS diode. It is the equilibrium condition of the MOS diode for the gate voltage applied. The merit of the photo-gate structure is that the sensing node and the integrating node are separate which allows true Correlated Double Sampling (CDS) operation to suppress kTC noise, $1/f$ noise and Fixed Pattern Noise (FPN) [06, 12]. Conversely, the demerit of the photo-gate structure is low spectral response because of the absorption in the polysilicon gate which has an absorption coefficient corresponding to that of crystalline silicon.

2.3 Different types of CMOS compatible photodiodes:

Photodiodes are the doorways to Image Sensors. The characteristics of the detectors, such as bandwidth, noise, linearity and dynamic range directly affect the performance of the system. Therefore, it is highly desirable to have as perfect a photodiode as possible. In a standard CMOS process, either p-well or n-well, several parasitic junction devices can be formed to convert light into an electrical signal. The n+/p-substrate photodiode, the p+/n-well photodiode and n-well/p-substrate photodiode are the three possible structures that can be implemented using p-substrate. The first two is “shallow” junction photodiodes whereas the third is a “deep” junction photodiodes. Fig.2.10 shows the cross sectional view of three CMOS compatible photodiodes [05, 07].

In the conventional CMOS process n-diffusion and p-substrate junction photodiode is the most widely used one due to its simple layout and less susceptible to lithographic variations that cause the fixed pattern noise. The quantum efficiency is better than that of p+/n-well photodiode due to the contribution of generated carriers in the bulk substrate and the wider depletion layer itself for the same pixel size. On the other hand, this diode introduces crosstalk and noise because of diffusion and leakage of carriers through the substrate [05, 07, 09]. As the carriers are generated in the bulk substrate the response time is expected to be longer than the p+/n-well junction device.

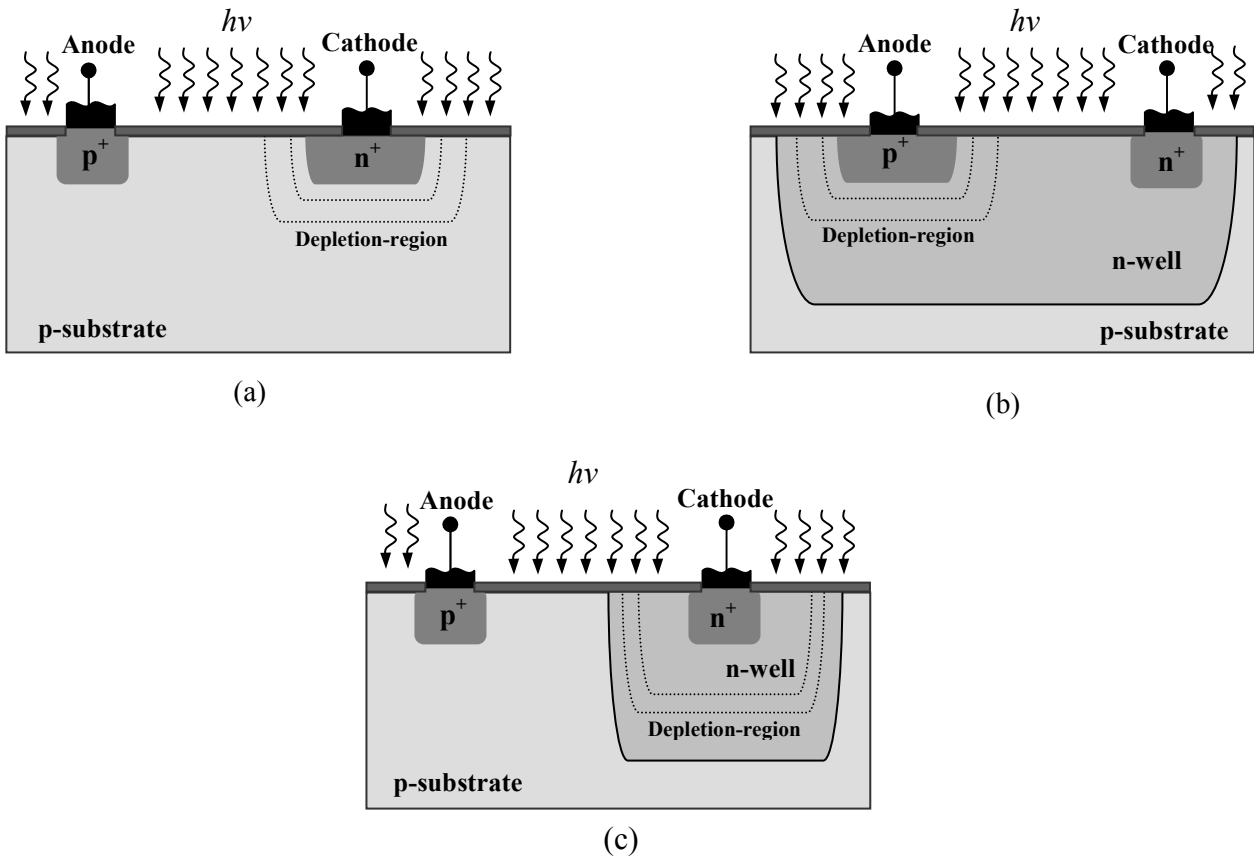


Fig.2.10: CMOS compatible photodiode structures (a) n+/p-substrate (b) p+/ n-well (c) n-well/p-substrate

The p+/n-well photodiode is formed with a p-diffusion in an n-well. The lower spectral response of this photodiode compared with the other devices due to the narrowness and shallowness of the p+/n-well junction. For the long wavelength optical signal the charge carriers generated outside the well are shielded by n-well/p-substrate junction, thus there is no chance to collect the charge carriers by the photodiode inside the well. As the n-well/p-substrate junction shielding will lead to better isolation for the photodiode, crosstalk between the neighbouring photodiodes are lower [11]. The maximum sensitivity occurs at 530nm wavelengths, reflecting the shallowness of the junction where most of the green-light is absorbed [10]. The diffusion-well diode has a better response in the green region than well-substrate diode because the junction is closer to the surface and therefore it can absorb more short-wavelength photons which have a high absorption co-efficient.

Finally, the well-substrate junction is formed between an n-well and a p-substrate. As it has a wide and deep depletion region, causes the best spectral response with respect to other photodiode structures. It also allows the collection of photogenerated minority carriers deeply inside the substrate. The capacitance of the well-substrate photodiodes is low, thus helps to achieve a high bandwidth of the device [05, 07, 09]. The disadvantage of this device is that, it offers higher crosstalk from the neighbouring photodiodes and substrate noise due to diffusion of the minority carriers. This photodiode junction has moderate dark current compared to the other photodiodes [10].

2.4 Considerable parameters of photodetector:

A number of important parameters are commonly used to describe the photodiode performance. These performance characteristics signify how a photodiode acts in response to an input of light energy. The photodiode parameters can be used to select an appropriate detector for a particular application. In general, one should give concentration on the following properties in a detector: i) a large response at the wavelength to be detected ii) a small value of the noise introduced by the detector iii) satisfactory speed

of response to follow variations in the optical signal being detected. To understand the descriptions of photodetector performance several conventional parameters are described in this section.

2.4.1 Responsivity:

The responsivity of a silicon photodetector gives a measure of the sensitivity to radiant energy. It can be defined as the ratio of the diode output to the incident power at a given wave length. Thus the responsivity is essentially a measure of the effectiveness of the device to transduce the electromagnetic radiation to electrical current or voltage. Responsivity varies with changes in wavelength, bias voltage and temperature. Since the reflection and absorption characteristics of the detector sensitive material change with wavelength thus changes the responsivity of the detector. The photodiode that generates a photocurrent can be derived by integrating the optical generation rate G_0 over the device active volume [14].

$$I_L = q \int_V G_0(x, P_{in}) dx \dots \dots \dots (2.17)$$

From I_L , the device responsivity can be obtained as

$$R = \frac{I_L}{P_{in}} \dots \dots \dots (2.18)$$

In the real device the number of electrons flowing in the external circuit is lower than the number of incident photons that lead the responsivity smaller than the ideal value. This happens due to the incident light has to undergo a number of steps before being converted into a current. Some non-idealities mechanisms limits the detector response in the following ways: the part of the optical power that is reflected at the photodiode interface due to dielectric mismatch; part of the power is absorbed in regions of where it does not contribute to useful output current and finally part of the power is transmitted through the PD without being absorbed.

2.4.2 Quantum efficiency:

It is defined as the number of incident photons that contribute to photocurrent divided by the number of the injected photons of specific wavelengths. Quantum efficiency is related to the responsivity as follows: it is equal to the current responsivity times the photon energy in electron-volts of the incident radiation. It can be expressed as a percentage,

$$Quantum\ Efficiency = R_\lambda \frac{1240}{\lambda} \times 100\% \dots \dots \dots (2.19)$$

where, the R_λ is the responsivity in A/W and λ is the wavelength in nm. The quantum efficiency is determined by three factors: the absorption coefficient of Si; the transmission co-efficient of the dielectric layers above silicon and the carrier collection efficiency of the sensor. The quantum efficiency decreases towards the short and long wavelengths that are caused by the reflections of the thin-film structure on the top of the silicon [14, 15]. So it is another parameter to measure the effectiveness of the basic radiant energy to produce electrical current in a detector.

2.4.3 Response time:

The dynamic performance is an important parameter of the photodiode. The photodiode response time is the root mean square sum of the charge collection time and the RC time constant arising from series plus load resistance and the junction and stray capacitance. The response time of a photodetector with output circuit depends on the following factors:

i) The transit time t_d of the photo carriers across the depletion region. This time depends on the carrier drift velocity v_s and depletion layer width W and it can be expressed by

$$t_d = \frac{W}{v_s} \dots \dots \dots (2.20)$$

ii) The diffusion time of the photo carriers which are absorbed outside the depletion region.

iii) The RC time constant of the circuit. The circuit after the photodiode acts like RC low pass filter with a pass band given by

$$B = \frac{1}{2\pi R_T C_T} \dots \dots \dots (2.21)$$

The capacitance of the photodiode must be kept small to prevent the RC time constant from limiting the response time. To achieve the higher quantum efficiency, the depletion layer width must be larger than l/α ; where α is the absorption coefficient, so that most of the light will be absorbed. At the same time, with large width the capacitance is small and RC time constant getting smaller leading to faster response but large width results in longer transit time. Therefore there is trade off between width and quantum efficiency.

2.4.4 Leakage current:

The dark current is the leakage current in photodiode and refers to the absorption of carriers that are not generated by photons but it flows when the reverse bias is applied on the photodiode. As the properties of leakage current carriers are intrinsically same as the photo-generated carriers, it is difficult to separate these two carriers from the mixture. It decreases the charge capacity that specified for photo-carriers. This current component introduces spatial and temporal variation of the output signals that contribute the fixed pattern noise and shot noise of the imagers respectively. Under the low illumination condition, the effect of leakage current is more severe because of the total amount of carriers becomes higher. The leakage current of a photodiode is essentially the same as that of the reverse-bias current for a p-n junction diode. The total reverse bias current can be approximately given by the sum of the generation current in the depletion region and the sum of the diffusion components in the neutral region [16]. This can be expressed as:

$$J_r = q \sqrt{\frac{D_n}{\tau_n}} \cdot \frac{n_i^2}{N_a} + \frac{qn_i W}{\tau_e} \dots \dots \dots (2.22)$$

where D_n is the diffusion co-efficient and τ_n is the lifetime of the electrons in the p-type region; n_i is the intrinsic carrier concentration; N_a is the doping concentration in the p-type region; W is the width of depletion region and τ_e denotes the effective lifetime in the depletion region. The first term of reverse current density equation comes from minority carrier diffusion from the charge neutral region and the second term is the generation current in the depletion region. The dark current is temperature dependent. In this equation the intrinsic carrier concentration n_i is strongly temperature dependent and the depletion layer width W is dependent on the bias voltage. At room temperature, for silicon junction diodes, the component of generation current usually dominates the reverse-bias current and the diffusion current dominates at high temperature.

2.4.5 Capacitance:

A capacitance is associated with the depletion region which exists at the p-n junction. The boundaries of the depletion region act as a parallel plate of the capacitor. The junction capacitance is directly proportional to the diffused area and inversely proportional to the width of the depletion region. The

width of the depletion region and the capacitance value can be determined by the doping profile. Using abrupt junction approximation, the width of the depletion region can be expressed:

$$W = \sqrt{\left[\frac{2\epsilon_s}{q} \left(\frac{1}{N_a} + \frac{1}{N_d} \right) (V_{bi} - V) \right]} \dots \dots \dots (2.23)$$

where ϵ_s is the permittivity of silicon; N_a and N_d are doping concentration of p-type and n-type region respectively; V_{bi} is the built-in potential and V is the applied bias voltage. The depletion capacitance per unit area can be defined

$$C_j \equiv \frac{dQ}{dV} = \frac{dQ}{W \frac{dQ}{\epsilon_s}} = \frac{\epsilon_s}{W} \dots \dots \dots (2.24)$$

where dQ is the incremental change in depletion layer charge per unit area and dV is the incremental applied voltage. So the capacitance can be expressed by using the above two equations

$$C_j = \sqrt{\left[\frac{\epsilon_s q N_a N_d}{2(N_a + N_d)(V_{bi} - V)} \right]} \dots \dots \dots (2.25)$$

We know the junction capacitance at the charge sensing node regulates the capacity and the charge-to-voltage conversion gain of the photo sensor device. In addition, the lower junction capacitance at the charge sensing node is usually favoured since it introduces a higher signal-to-noise ratio of the output signals. Moreover the capacitance is dependent on the reverse bias voltage; increase in the reverse bias voltage causes the depletion width to increase, thus the drift time of carriers becomes longer across the depletion region [17].

2.4.6 Noise:

Noise is a critical performance parameter for the photodetectors. There are several sources of noise in photodetectors. These include shot noise from detector photocurrent, shot noise from the dark current, Johnson noise due to the thermal fluctuation in the detector impedance and flicker noise that is inversely proportional to the measurement frequency [13].

Quantum shot noise arises from the statistical Poisson-distributed nature of the arrival process of photons and collection of photo generated electron. The standard deviation of the photon shot noise is

$$\langle i_Q^2 \rangle = \sigma_Q^2 = 2qI_p B M^2 F(M) \dots \dots \dots (2.26)$$

where I_p = Photo current
 B = Receiver bandwidth
 $F(M)$ is the noise figure and generally $F(M) \approx M^X$. For the *pin* photodetector M and $F(M)$ is equal to 1.

The current that continues to flow through the photodiode device in the absence of light is called dark current is responsible for dark current shot noise. It arises from electron and hole which is thermally

generated in the *pn* junction of the photodiode in the bulk area. The dark current shot noise can be expressed as:

$$\langle i_D^2 \rangle = \sigma_D^2 = 2qI_D BM^2 F(M) \dots \dots \dots (2.27)$$

where I_D is the dark current. Due to the surface area, surface defects and bias voltage a surface dark current flows in the device that introduces a noise is called surface dark current shot noise. It can be defined

$$\langle i_{DS}^2 \rangle = \sigma_{DS}^2 = 2qI_L B \dots \dots \dots (2.28)$$

where I_L is the surface dark current. The shot noise of the photodetectors limits the SNR when the detected signal is large. Thermal noise, also called Johnson noise or Nyquist noise generated by the thermal agitation of the electrons inside an electrical conductor at equilibrium, which happens regardless of any applied voltage. A photodetector thermal noise can be modelled as a voltage source in series with an ideal resistor R . In this case,

$$\langle V^2 \rangle = 4k_B TRB \dots \dots \dots (2.29)$$

It can also be modelled a current in parallel with R

$$\langle I^2 \rangle = \frac{4k_B TB}{R} \dots \dots \dots (2.30)$$

where, $k_B = 1.38 \times 10^{-23} \text{ JK}^{-1}$ is Boltzmann constant. This noise can be suppressed if the sensor is operated at low temperature.

2.5 Review of CCD and CMOS Image Sensor:

Solid-state optical sensors are used in a wide range of applications. Charge Coupled Device (CCD) technologies and image sensors have been discovered at the beginning of the seventies which can be found today in almost all electronic acquisition systems [18]. CCD image sensor is the first solid-state image sensor that offers good picture resolution, higher fill factor but on the other hand it requires more power and is generally more expensive. The Complementary Metal Oxide Semiconductor (CMOS) imaging detectors began to make their move into the CCD detector arena. While CMOS sensors have generally lagged behind CCD sensors in terms of image quality, it has been able to compete in the imaging market by taking advantage of standard CMOS process technology. The smaller device size, light weight and lower cost made CMOS sensors suitable for high-volume consumer and mobile applications. Traditionally, the CCD vs. CMOS battle has been a trade-off between image quality and quantity. CCD image sensors have delivered improved quality, while CMOS image sensors have provided better performance in terms of battery life and lower cost. CMOS image sensors are increasingly rivalling the image quality that CCD sensors have traditionally provided. Improved architecture and processes have to overcome to a large extent, the early weakness of CMOS imagers, most likely with respect to noise and sensitivity. To compete in the high volume marketplace, meanwhile, CCD sensors have responded by using new methods to reduce clocking voltages and power consumption reported in [19]. The overall architecture, operation and comparative performance of CCD and CMOS based image sensors are described in this section.

2.5.1 Charged-Coupled Device (CCD) Image Sensor:

A CCD pixel is basically a MOS capacitor [18], usually a buried channel type. Fig.2.11 shows a schematic cross section of such a capacitor. The device is typically built on a p-type silicon substrate with larger thickness and an n-type layer with small thickness grown up on the surface. A thin silicon dioxide

layer is formed followed by a metal electrode. When a positive voltage is applied to the electrode, due to the reverse bias action at the p-n junction a potential well is formed in the n-type silicon below the electrode. Electron-hole pairs are generated in the depletion region when light is incident on the CCD device. Due to the applied voltage the electrons migrate upwards into the n-type silicon layer and are trapped in the potential well. The build up of negative charge is thus directly proportional to the level of incident light.

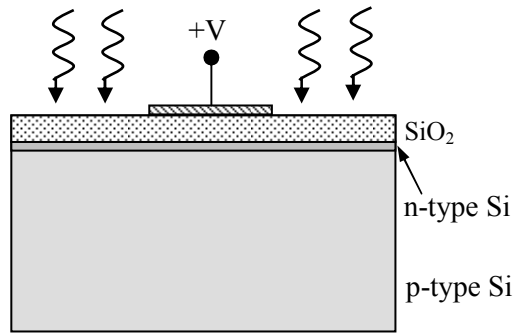


Fig.2.11: Charged-Coupled Device (CCD) Cell

Readout Process: Considering each pixel is divided into three different areas known as phases shown in the following Fig.2.12 given below. The integration periods, phi 1 and phi 2 are the charge holding modes, and phi 3 is the charge blocking mode. When light is incident on the CCD device the charge carriers are generated and restrained in a potential well below the surface. At the end of the integration period, when it is time to transfer the captured image out of the array, the following process takes place. After switching phi1, phi2 and phi3 at different potential by a clock signal the carriers are transported in a lateral direction.

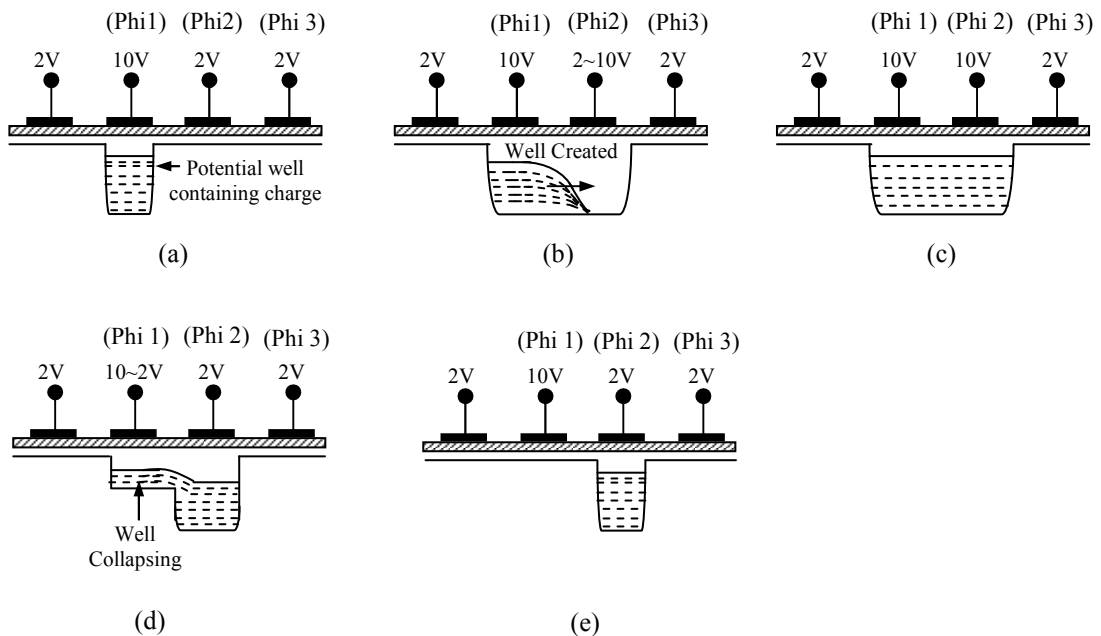


Fig.2.12: Charge transfer process

Firstly phi 1 is placed in charge blocking mode, which has the effect of transferring the total charge of phi 1 and phi 2 into only phi 2. Phi 3 is then placed in charge holding mode, which allows the charge in phi 2 to distribute itself evenly between phi 2 and phi 3. Next, phi 2 is placed in charge blocking mode, forcing charges into phi 3. This basic process of charge transport is repeated until the read out sequence is taking place. More elaborate analysis of operation and physics of Charge Coupled Device (CCD) are reported in [20, 21].

Area array of CCD Architecture:

Depending on the different applications the architecture of area array CCD generally falls into one of four categories: full frame array, frame transfer array, split frame transfer array and interlines transfer array (Fig. 2.13).

Full Frame array – The image is transferred directly one row at a time from the imaging region of the sensor to a serial register and finally feeding the charge to an output sense electrode. However, since only a single row can be transferred to the readout register at a time the rest of the imaging pixels must wait. Since during this period, pixels are being irradiated continuously this can lead to smearing and blurring of the final image. Another problem is raised during high-speed applications. In these situations, the integration time will be only a small percentage of the total time required to record and read out the total image from the array. This causes lower contrast since very little time is spent actually to record the image. These problems can be solved by using a mechanical or external electronic shutter to shield the sensitive area during readout time.

Frame Transfer Array – A frame transfer device utilises two identical arrays: one is the light shielded storage section and the other is the imaging section of the array. At the integration time, the captured image is quickly transferred to the adjacent storage section. The storage sections are covered with a metal shield to prevent them from being irradiated. While the next scene is being captured, the previous scene that held in the storage section is transferred to the readout register as described above. The use of this technique effectively increases the time available for integration and maintaining a high frame rate.

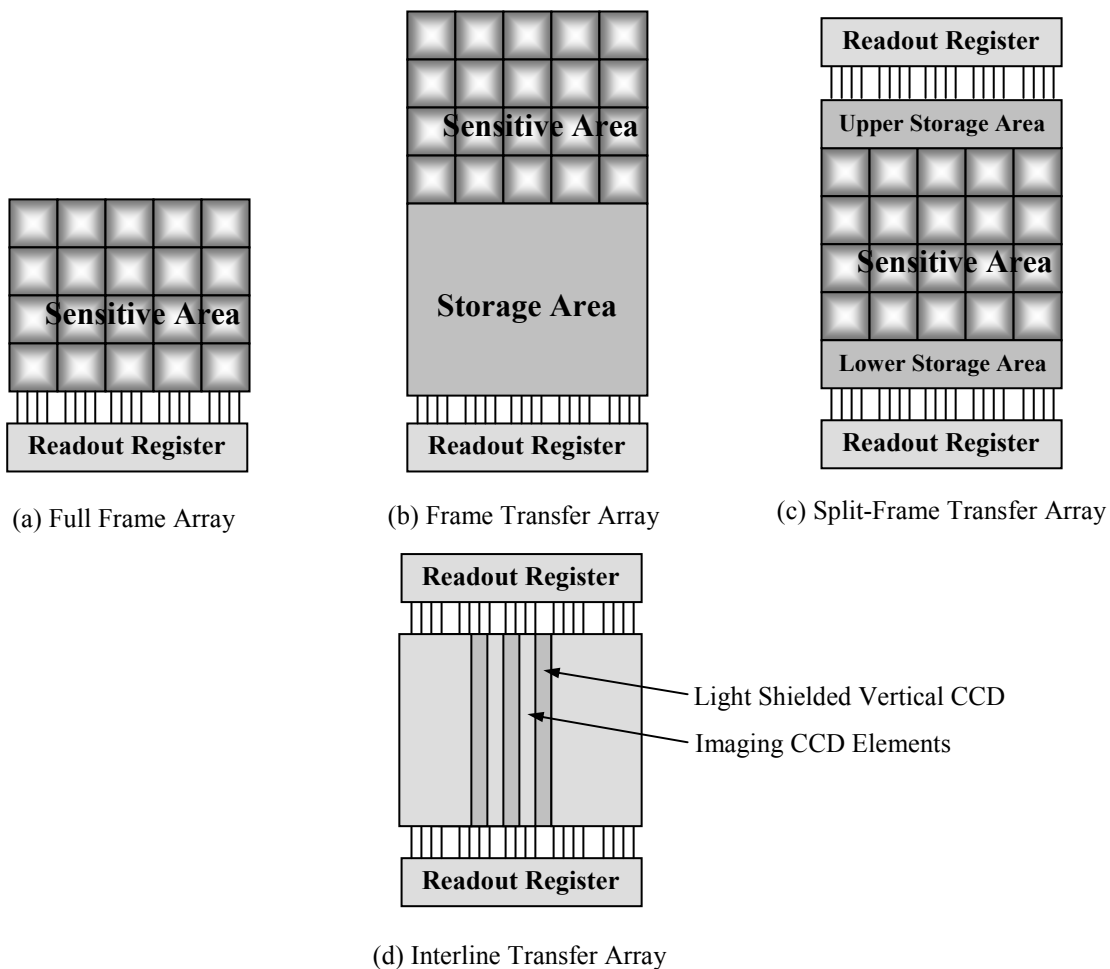


Fig.2.13: Area Array of CCD Architecture

Split Frame Transfer Array – The split frame transfer type device is essentially the same as a frame transfer device, except that the storage section is split into two equal parts, with each half being located above and below the imaging section. The advantage of this device is that it allows the image to be transferred out of the imaging section in half the time that is required for a frame transfer device.

Interline Transfer Array –In interline transfer device, within photosensitive matrix the columns of photosensitive elements are separated by columns of light shielded registers. At the end of the integration period, all of the photosensitive elements simultaneously transfer their accumulated charge to the adjacent storage registers. The light shielded registers then transfer the charge to the readout register in a very short time. This type of device has the significant drawback that a large proportion of the imaging section is not sensitive to light. To minimize the problems, micro lenses are often placed directly over the imaging section of the array that have the effect of focusing the incoming light onto just the light sensitive areas of each element.

2.5.2 CMOS based Image Sensor:

CMOS, Complimentary Metal Oxide Semiconductor, image sensors have been around for nearly as long as CCDs [22]. High performance CMOS image sensors [23] use active pixel structures invented at NASA Jet Propulsion Laboratory in 1993. CMOS sensors draw less power than CCD and use the same manufacturing technologies as microprocessors and memory modules, thus they are easier to produce. CMOS pixels can be divided into two main groups: Active Pixel Sensor (APS) and Passive Pixel Sensor (PPS). Like CCDs, they are formed from a grid of light sensitive elements, each capable of producing an electrical signal/charge proportional to the incident light. Each CMOS pixel employs a photodiode, a capacitor and the amplifier transistors for APS. Prior to the start of the integration period, the capacitor will be charged to some known voltage. When the integration period begins, the charge on the capacitor is allowed to slowly discharge through the photodiode, the rate of discharge being directly proportional to the level of incident light. At the end of the integration period, the charge remaining in the capacitor is read out and digitized. Fig.2.14 shows the most common three transistors Active Pixel Sensor (APS) [24]. The reset transistor (RES), acts as a switch to reset the floating diffusion which acts in this case as the photo diode. When the reset transistor is turned on, the photodiode effectively connects to the power supply clearing all integrated charges. The read-out transistor, SF is a source follower transistor amplifier which allows the pixel voltage to be observed without removing the accumulated charge. Finally the select transistor, SEL allows the signal to be read-out. The row decoder and column decoder select each pixel to read out for further Image processing.

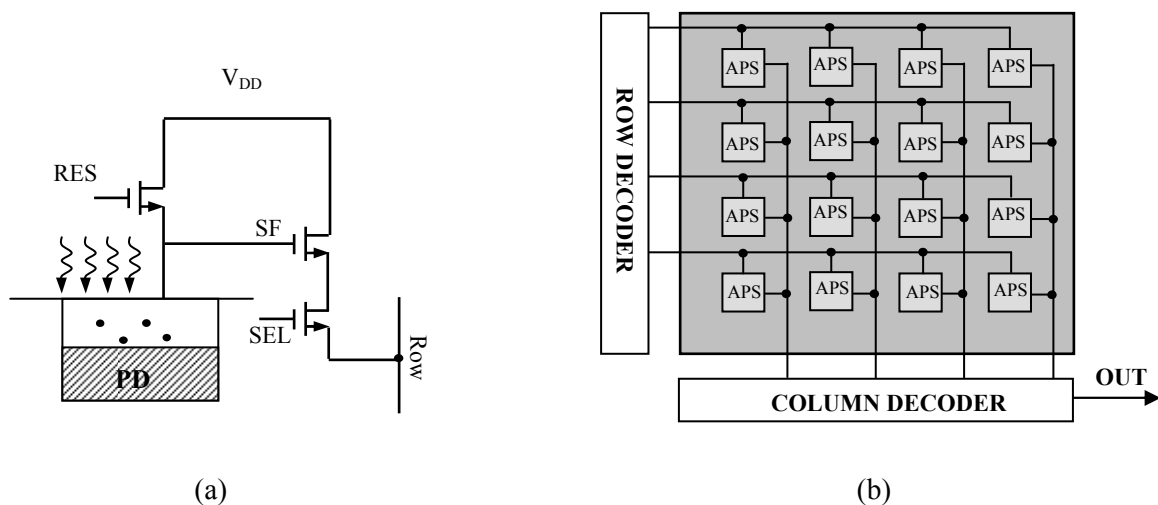


Fig.2.14: (a) CMOS based pixel (b) Pixel read out System

2.5.3 Comparison between CCD and CMOS Imagers:

CCD and CMOS image sensors are two different technologies for capturing images. Each has unique strengths and weaknesses giving advantages in different field of applications. Both CCD and CMOS imagers convert light into electric charge and process it into electronic signals. In a CCD sensor, the charge packet of every pixel is transferred through a very limited number of output nodes to be converted to voltage, buffered, and sent off-chip as an analog signal. All of the pixel can be dedicated to light capture, therefore the photo sensitive area is large and the output uniformity is high. In a CMOS sensor, each pixel has its own charge-to-voltage conversion, and also includes amplifiers, noise-correction, and digitization circuits, so that the chip output is digital bits. The other circuit functionalities enhance the design complexity and decrease the photosensitive area for light capture. Traditionally CCD imagers provided the performance benchmarks in the photographic, scientific, and industrial applications that demand the utmost image quality as measured in quantum efficiency and noise at the expense of system size. On the other hand CMOS imagers offer more functionality on the chip, lower power dissipation at the chip level and the possibility of smaller system size. Variations in device characteristics, such as feature dimensions and silicon doping levels, from pixel to pixel and column to column lead to substantial fixed pattern noise with CMOS. There is also a high temporal noise from thermal and 1/f sources with CMOS sensors due to using of multiple transistor stages. In CCD sensors fixed pattern noise and temporal noise is smaller because charge packets are transferred almost perfectly within the sensor and pass to the outside of the sensor area by a single output stage [13,23]. In CCD technology the fill factor of the sensor is high compared to CMOS technology, giving a better photosensitive efficiency. Furthermore, special attention is paid to minimizing dark current, a parasitic effect in photo detectors; so that it is lower with CCD technology than with CMOS [25].

Table-I is given below summarized the comparative study between CCD and CMOS image sensor.

Feature	CCD	CMOS
Signal out of pixel	Electron packet	Voltage
Signal out of chip	Voltage (analog)	Bits (digital)
Signal out of camera	Bits (Digital)	Bits (Digital)
Fill factor	High	Moderate
Amplifier mismatch	N/A	Moderate
System Noise	Low	Moderate
Responsivity	Moderate	Slightly better
Dynamic Range	High	Moderate
Uniformity	High	Low to Moderate
Uniform Shuttering	Fast, Common	Poor
Speed	Moderate to high	Higher
Biasing and Clocking	Multiple and higher Voltage	Single and Low Voltage
System Complexity	High	Low
Sensor Complexity	Low	High
Unit price	High	Comparatively low

2.6 Available technologies for Image Sensor:

Now a day different technologies are available to design of image sensor chips. CCD, CMOS, Bi-CMOS and GaAs (HEMT and MESFET) are the existing technologies that offer advantages and disadvantages in their limited technological process. CCD sensors have been used in cameras for more than 30 years and present many advantageous qualities: better light sensitivity than CMOS sensors that translates into better images in low light conditions, low noise, low non-uniformity, and low dark current. CCD sensors are, however, more expensive as they are made in a non-standard process and more complex to integrate into a camera. Over the last decade, CMOS imager technology made huge progress which drastically improved its performance. The most prominent was the CMOS Passive Pixel Sensor (PPS) fabricated by VLSI Vision Ltd. [26] and from 1992 to the present, the Active Pixel Sensor (APS) was and still under continuous development [27]. CMOS has been widely used in many designs and expanded the overall imaging market due to the development of new applications. Another technology is bipolar transistor in Bi-CMOS processes. It has better matching properties, and higher speeds but limited availability due to their complexity and cost. It also needs large silicon area, which makes them unattractive for large quantity vision chips [05]. In the commercial grade CMOS processes are accessible through fabrication foundries, such as TSMC, UMC and CMP etc. Finally, GaAs processes have been used only to a very limited extent due to technological immaturity and process and they are generally expensive. These opto-electronic devices are only available in very specialized processes [05]. In this section we will briefly discuss about CCD sensor technology and then CMOS imaging technology that is our Image sensor interest.

2.6.1 CCD Image Sensor technology:

Charged Coupled Devices are the dominant technology for image sensor. Therefore from the beginning research has been mainly focused on CCD technology. The device architecture based on series and parallel connection of capacitors, which are made using a dedicated semiconductor process and switched it by clocked signal at different phases. CCD technology has some limitations in its fundamental operation—the need of nearly perfect Transfer Efficiency (CTE) imposes a great impact on CCD performance. The other considerable limitations of CCD technologies are: [24, 28].

- a) Risk to radiation damage.
- b) Required complex high speed shifting clocks for its operation.
- c) Larger operational power required due to high speed switching.
- d) Difficulty in achieving large array size.
- e) Difficult to integrate on-chip electronics because of specialized non-standard.
- f) Limited frame-rate of CCD and difficult to extend the spectral range.

2.6.2 CMOS Image Sensor technology:

CMOS imagers began to be a well-built alternative of CCD since early nineties. The most important feature that would satisfy by this technology is the demand for low-power, miniaturised and cost-effective imaging systems. It also offered the possibility to monolithically integrate a significant amount of integrated electronics on-chip that incorporates all necessary camera functions and reduces component and packaging costs. CMOS processes are well established and continue to become more mature. The demand for digital applications has led to continuous development and attributed to down-scaling of CMOS processes. CMOS processes are now readily available for prototype designs through fabrication foundries, such as TSMC, UMC etc. Circuit and system design by this process is supported by CAD design software such as Cadence. Recently several modifications to standard CMOS technologies to improve their imaging performance have been reported [29]. To improve the photosensitivity, non-silicided deep junction diodes and integrated micro lenses are used. The doping profiles of these diodes are optimised to increase quantum efficiency at visible wavelengths and to lower capacitance. To minimize the dark non-silicided, double-diffused source/drain implantation is used. Besides these advantages of CMOS vision chip technology it has some disadvantages too.

- a) Leading-edge processes of the chip are driven by digital applications and less optimization for analog circuit design [05].
- b) As the gates of all pixels are connected in parallel on a given column that increase the column-bus capacitance, thus affects the read out speed and read out noise [30].
- c) Non- uniformity arises due to multiple levels of amplification at pixel and column level.
- d) Due to the mismatch of CMOS devices fixed pattern noise is introduced.

Chapter - 03

State of the art of 3D imaging

3D measurement techniques are concerned with extracting information from the geometric evaluation of three co-ordinates (x, y, z) and the texture of the visible surfaces in a scene. The complete 3D information can be realized acoustically by ultrasonic sound and radio frequency electromagnetic waves or optically with light. In all methods, a signal travels from the respective sources of the methods to a target and the distance measurement can be calculated based on the properties of the reflected signal from the target. Comparing with the acoustic and RF wave methods, the optical methods are more reliable in terms of high resolution and accuracy in the distance measurement [31].

Due to the drastic increase in demand of 3D imaging system, recently a lot of effort has been concentrated to develop a standard 3D imager. The 2D-imaging system can evaluate only the intensity projection of a scene, there is no information about the depth of the 3D objects. Several approaches have been proposed on image capturing techniques using specialized photo detector coupled with depth measurement system of 3D object. A much more practical range measurement method is the Time-Of-Flight (TOF) principle. In time-of-flight optical ranging, the phase information is used to plot the distance map of the observed scene, thus enabling the reconstruction of the shape and position of the observed objects[32]. TOF systems are further divided in different subcategories which are pulsed modulated, continuous wave modulated and pseudo-noise coded TOF. TOF technique provides the best performance in terms of acquisition speed, reliability, overall cost of the system and is most suited to integrate electronic circuitry with more functionality. Several studies on image capturing techniques using specialized pixels coupled with active illumination have reported to produce images with information even at a low intensity level [33, 34].

3.1 Different optical measurement techniques for 3D imaging:

The optical distance measurement methods for 3D range imaging can be classified into two ways, active range imaging and passive range imaging. The active method uses a coherent light source to project onto a target and determines the shape of the target by its reflections where as the passive rely on the ambient environment conditions to get the information of the object. There are some other methods for the distance measurement such as: the image based methods, the distance can be determined with some algorithm based on shapes and shades or the respective distances of the different points of the object. The computer vision research community is largely focused on these methods. Another one is the direct method that can give the instantly recognizable distance to some points in the object [35].

In optical distance measurement, several studies have reported to produce 3D information including stereo vision cameras [36], system based on structured light and laser scanner vision system [37]. The advantage and performance of these systems tend to be mutually exclusive by their own limited set of situations. Different types of optical techniques for 3D imaging range measurement are available in the literature. According to the working principle, range and accuracy it can be classified in three categories such as:

- 3.1.1 Triangular Method
- 3.1.2 Interferometry Method
- 3.1.3 Time-of-Flight Method

All of these above techniques mostly work with light in the 400 nm to 1000nm wavelength range belonging to visible light and near infrared region.

3.1.1 Triangular method:

The distance measurement by triangulation method analyzes a triangle by trigonometric approach. A target on a visible surface is one point of the triangle; the remaining two points are obtained by using two optical systems. The distance between two optical systems is the baseline of a triangle that can be calculated. So the two projection lines of two optical systems in the target can construct the triangle. These two optical systems can determine the two different angles between the baseline and projection line. The distance of the target can be determined using trigonometric formula. There are two main types in triangulation system

- 3.1.1.1 Passive triangular method [38]
- 3.1.1.2 Active triangular method [39]

3.1.1.1 Passive Triangular method:

In passive triangular method two optical systems observe the same target from two different points with respect to the same baseline. Two different points to measure must be identified from both viewing positions and it requires some good features in the scenes with high contrast. At least two cameras are necessary to observe the scene from different angles. Assuming that the two cameras are observing the scene from two different distance points x and y of known value α and the measured viewing angles between the baseline and the two projection lines of two optical systems are φ and θ . Fig.3.1 shows the passive triangulation method. The distance between the baseline and the target d can be determined by the trigonometric formula.

$$d = \frac{\alpha}{\frac{1}{\tan \varphi} + \frac{1}{\tan \theta}} \dots\dots\dots 3.1$$

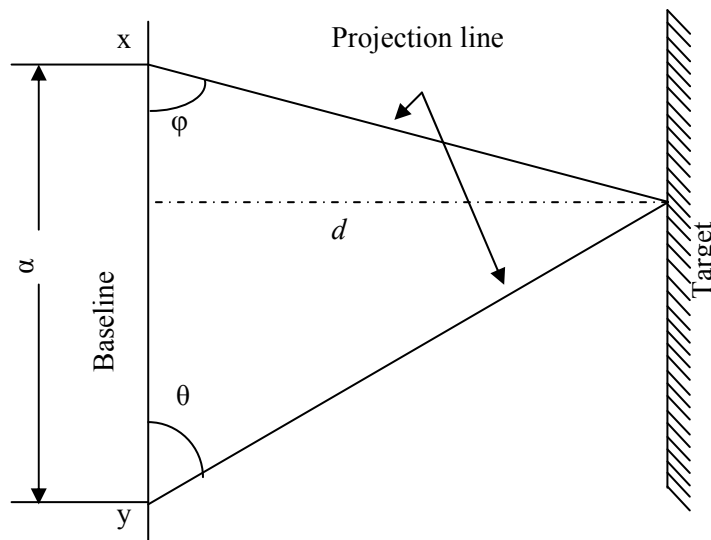


Fig. 3.1: Passive triangulation method.

Stereovision technique refers to the passive triangulation method [36] and produces 3D information from at least two slightly different 2D images. This technique is similar to aspects of the human visual process, where the human eyes are two view points used for the acquisition of images of the same scene. As the distance between the two eyes results in slightly different 2D images, this phenomenon is used in the

stereovision to construct the 3D images. The typical features of both images captured by two cameras are compared with the help of 2D correlation. The viewing angles between the baseline and projection line of the camera φ and θ can be deduced and the distance can be calculated using the equation 3.1. The stereovision system can build the dense depth maps. The system components are highly reliable since it requires no moving parts. It also captures the entire frame at the same time so that the depth of map of all pixels can be calculated from the same perspective. The shadowing effect is the typical disadvantage of the stereovision system like other triangular systems. Although it can be minimized by using more than two cameras in order to increase the multiple viewpoints, this improvement also increases the data processing and overall cost of the system.

3.1.1.2 Active Triangular method:

This technique consists of one light source and one camera [39]. The light source is projected to a target which is observed by a camera. In this method, two similar triangles are formed; based on the optical axis of the imaging device, the focal length of the system and the position of the projected point on the camera. Fig.3.2 shows the active triangulation method. Considering the distance between the light source and the camera is α , so the distance d of the target can be determined by

$$d = h \frac{\alpha}{\alpha'} \dots\dots\dots 3.2$$

where h is the focal length of the camera and α' is the projected distance.

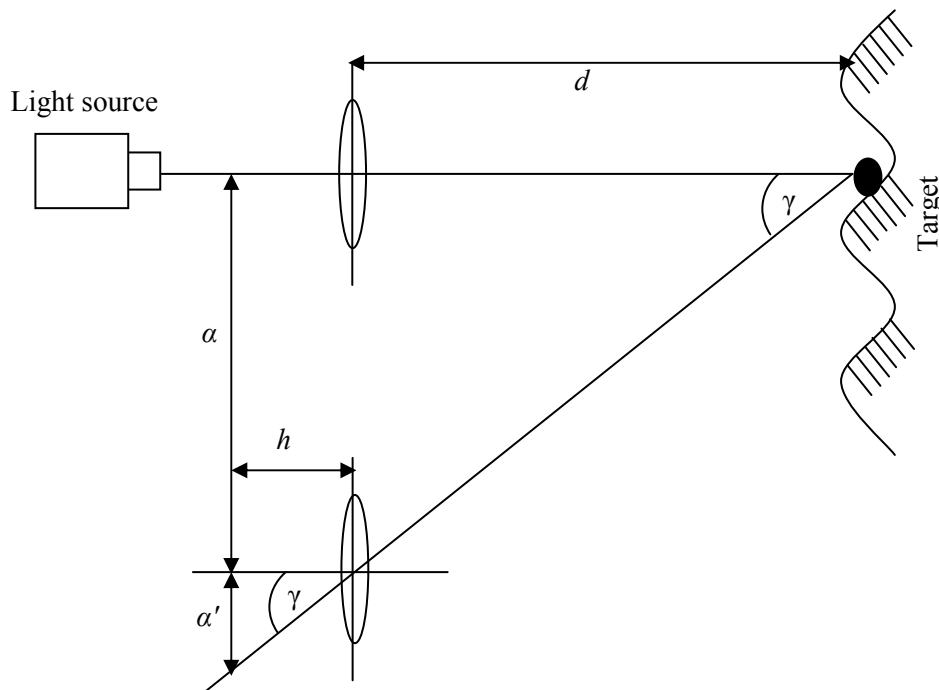


Fig.3.2: Active triangulation methods.

The basic phenomena of this method, a focused beam of light illuminates a tiny spot on the surface of the scene and a camera records an image of the spot. This technique gives a single range point. Moving the light spot using mirrors allows the surface of the object to be scanned. If the position of the light source, the orientation of the project plane and the triangulation distance (baseline separation) of the laser and camera are all known, the depth information from all points on the object can be determined. The limitation of this approach is that it needs to capture many frames while sweeping the light over the object and thus increasing the long processing time to get the full depth of information from the whole 3D scene.

3.1.2 Interferometry:

Interferometric distance is described by the superposition of two monochromatic waves of the frequency but with different amplitude and phase [40]. When two light waves are superimposed, the resultant intensity at any point depends on whether they reinforce or cancel each other. This is a well-known phenomenon of interference. Consider two monochromatic waves of complex amplitudes $X_1(\mathbf{r})$ and $X_2(\mathbf{r})$ are superposed, the result is a monochromatic wave of the same frequency and complex amplitude

$$X(r) = X_1(r) + X_2(r) \dots \dots \dots 3.3$$

where $X_1 = \sqrt{I_1} \exp(j\theta_1)$ and $X_2 = \sqrt{I_2} \exp(j\theta_2)$ are the complex amplitudes of the two waves. As we know that the optical intensity of a monochromatic wave is the absolute square of its complex amplitude, the resultant intensity is therefore

$$\begin{aligned} I &= |X|^2 \\ &= |X_1 + X_2|^2 \\ &= |X_1|^2 + |X_2|^2 + X_1^* X_2 + X_1 X_2^* \dots \dots \dots 3.4 \end{aligned}$$

The explicit dependence on r has been omitted for convenience. Substituting X_1 and X_2 in equation 3.4, we obtain

$$I = I_1 + I_2 + 2\sqrt{I_1 I_2} \cos \theta \dots \dots \dots 3.5$$

The above equation is called the interference equation, where I_1 and I_2 are the intensities due to the two waves acting separately and $\theta = \theta_1 - \theta_2$ is the difference between the two waves.

Interferometer is an optical instrument that split a light beam into two parts by a beam splitter and travels two different paths. One ray is projected to a mirror and the other is targeted on the object of variable distance. Both light beams are reflected back to the beam splitter and projected onto a camera. When those reflected beams are made to cross each other, the region of crossing will exhibit an interference fringe. By recording and counting the minimum and maximum transitions in the interference of light wavelength, the distance between the optical system and the target can be measured.

Consider the superposition of two plane waves, each of intensity I_0 , propagating in the z direction and assume that one wave is delayed by a distance l with respect to the other, so that $X_1 = \sqrt{I_0} \exp(-jkz)$ and $X_2 = \sqrt{I_0} \exp[-jk(z-l)]$. The intensity I of the sum of these two waves can be determined by substituting $I_1=I_2=I_0$ and $\theta=kl=2\pi l/\lambda$ in the equation 3.5,

$$I = 2I_0 \left[1 + \cos\left(2\pi \frac{l}{\lambda}\right) \right] \dots \dots \dots 3.6$$

The dependence of the intensity I is the superposition of two waves, each of intensity I_0 and on the delay distance l . When the delay distance is a multiple of λ , complete constructive interference occurs and the total intensity becomes $I=4I_0$. On the other hand, if l is an odd integer multiple of $\lambda/2$, thus the interference is destructive and the average intensity is the sum of the two intensities $2I_0$.

Some common types of interferometer setup can be found, for example the Rayleigh interferometer, the Michelson interferometer, the Mach-Zehnder interferometer and the Sagnac interferometer [41, 42]. The main disadvantage of classical interferometer is that the unambiguous distance range is as low as half of the wavelength and absolute distance measurements are not possible with this method. To overcome these drawbacks different types of techniques have been proposed in literature such as: Multiple-wavelength

Interferometry [40, 43], electronic speckle pattern Interferometry (ESPI) and white light Interferometry or low-coherence Interferometry [44]. Interferometry requires accurate optical alignment for precise measurements over small distances ranging from micrometers to several centimetres.

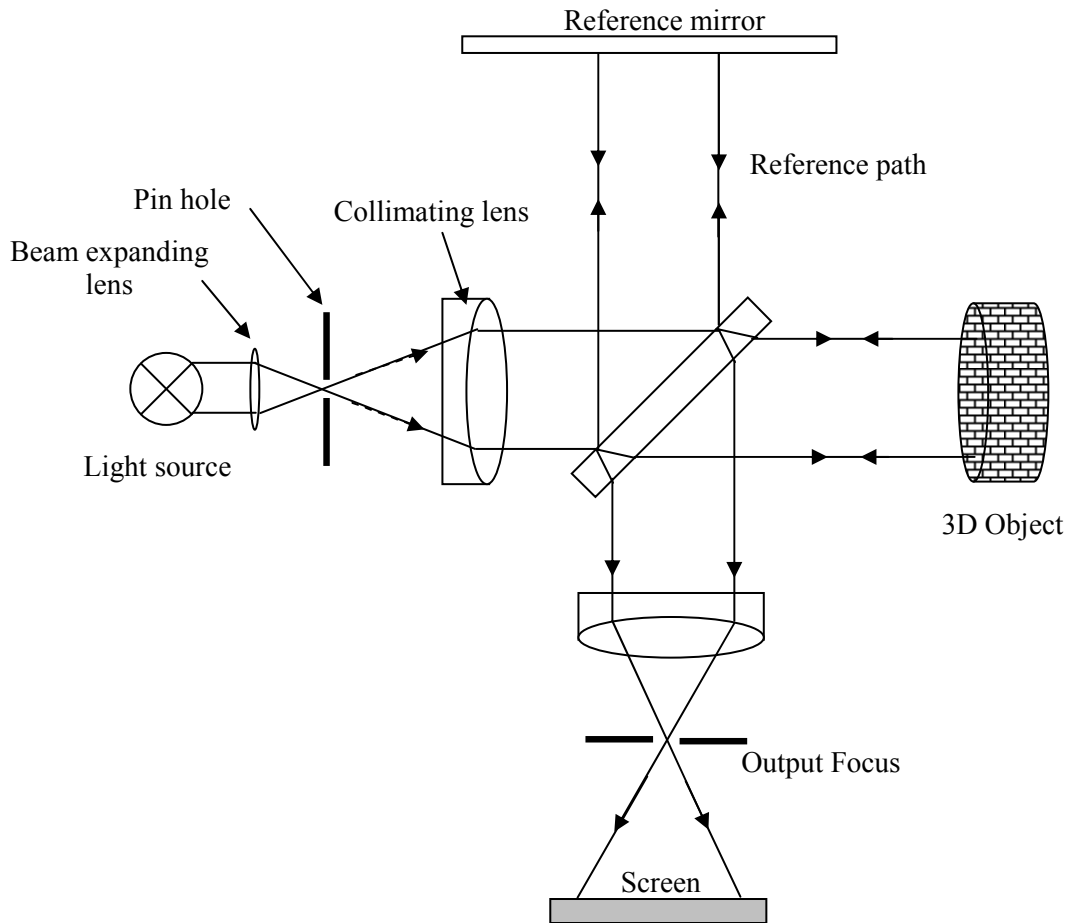


Fig.3.3: Set up of Interferometry Method

3.1.3 Time-of-Flight (TOF) method:

The distance measurement by the Time-of-flight method is an alternative to the triangulation method. TOF technique is based on the measurement (either direct or indirect method) of the time needed for an optical signal to travel from a source to a target and back to a sensor [37]. This is called the round trip transit time (t_r). Since the velocity of light is known, we can convert the time measurement into a two-way distance measurement according to the equation,

$$2d = ct_r \dots\dots\dots (3.7)$$

where d is the distance of the target and c is the speed of light. TOF systems are further divided in different subcategories; three methods to accomplished TOF range imaging which is pulsed modulated, continuous wave modulated and pseudo-noise coded TOF. The advantage TOF technique provides the best performance in terms of low cost, real time imaging, dynamic range and is most suited to integrate electronic circuitry with more functionality.

The distance measurement by the TOF method is an alternative to the triangulation method. This technique is based on the measurement of time; an optical signal is travel from a modulated light source

to a target and back to a sensor. Each pixel in the sensor device is capable to detect the phase of the reflected light. This range can be determined by measuring the phase angle (θ_r) between the transmitted signal and the received signal. This phase angle can be related to a time delay t_r . The relation between phase angle delay θ_r , modulation frequency f_{mod} and time delay t_r is

$$t_r = \frac{\theta_r}{2\pi f_{\text{mod}}} \dots \dots \dots (3.8)$$

where time delay t_r is equal to the round trip transmit time in second, θ_r is measured in radians and f_{mod} is in Hz .

The distance d between the sensor and the target is achieved according to the equation (3.7) and (3.8). So the distance d can be achieved by using the relation:

$$d = \frac{c\theta_r}{4\pi f_{\text{mod}}} \dots \dots \dots (3.9)$$

Fig.3.4 shows the TOF method for distance measurement. Therefore, as a general rule, it can be stated that the modulation frequency should be adjusted based on the maximum target distance, with considering that reflective object beyond the non-ambiguous range are frequently aliased [45].

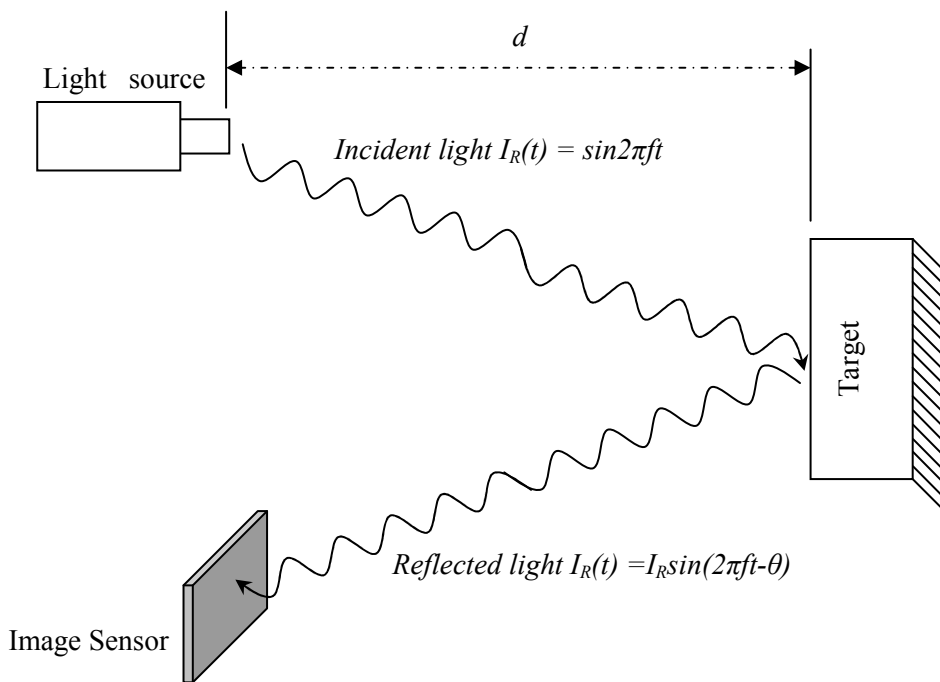


Fig.3.4: Time of Flight Principle

Fig.3.5 shows a scheme of the phase shift measurement principle. In this figure C is the amplitude of the transmitted modulated signal from a light source, B is the mean intensity of the received signal which is reflected from the object and A is its amplitude. The received signal is offset-shifted in intensity with respect to the emitted signal due to the additional background light [46].

A single phase measurement requires the acquisition of four amplitude measurements with four different phase delays applied to the received signal i.e. the signal is sampled four times in each cycle, at 90° phase angle. From the four samples (A_0, A_1, A_2, A_3), the parameters A and B and the phase ϕ can be calculated:

$$A = \frac{\sqrt{(A_0 - A_2)^2 + (A_1 - A_3)^2}}{2} \dots\dots\dots 3.10$$

$$B = \frac{A_0 + A_1 + A_2 + A_3}{4} \dots\dots\dots 3.11$$

$$\varphi = \arctan\left(\frac{A_0 - A_2}{A_1 - A_3}\right) \dots\dots\dots 3.12$$

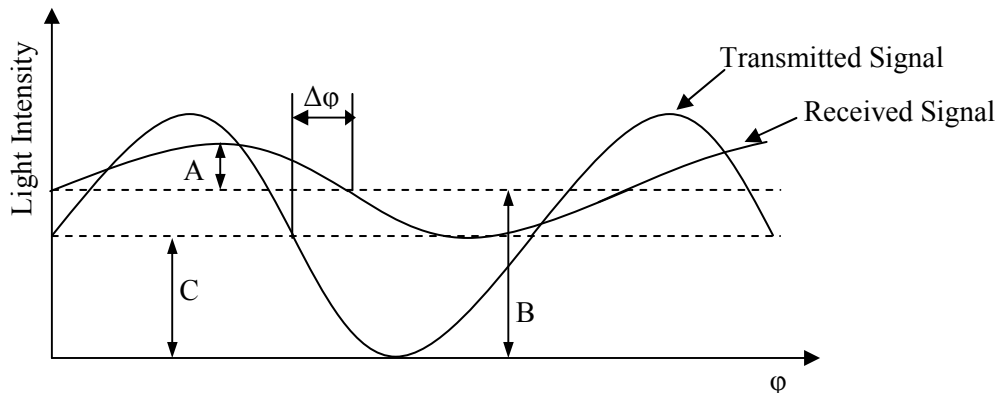


Fig.3.5: Phase shift measurement techniques

According to the different mode of operations the TOF measurement can be classified into three groups

- 3.1.3.1 Pulsed Modulation TOF technique
- 3.1.3.2 Continuous wave (CW) Modulation TOF technique
- 3.1.3.3 Pseudo-Noise Modulation TOF technique

3.1.3.1 Pulsed Modulation TOF technique:

The pulsed laser operation is the most useful method of operating a Time-of-Flight technique system. In this system there are devices with a pulsed laser and a custom imaging integrated circuit with a counter behind every pixel. A light pulse is sent out and its turn around time is measured by correlation of start and stop signal with the parallel running counter. This technique can produce depth values for each pixel on every frame. The advantage of using pulsed light technique is that a high amount of energy can be transmitted in a very short time. Thus the influence of background illumination can be reduced. It also attains a high short term optical signal-to-noise ratio while maintaining a low mean value of optical power. As the optical threshold is changed with the surface distance of the object and the atmospheric attenuation leads to dispersion and flattens the slope of the received pulse thus it makes the problem for the receiving path is to detect exactly the arrival time of the backscattered light pulse. The advantage of using pulsed light modulation is that it enables the measurement of the long distance. However it requires a receiver with high dynamics and a large bandwidth. Due to some advantages the TOF rangefinders are operated with pulsed modulation [47].

3.1.3.2 Continuous Wave (CW) modulation TOF technique:

Continuous wave (CW) modulation also is used in optical ranging systems. Different shapes of modulation signals such as sinusoidal waves or square waves can be used for this mode of operation and

extremely fast rise and fall times are not required like pulsed modulation. As we know the modulation frequency, the measured phase delay directly corresponds to time-of-flight. Compared to the pulsed modulation, the phase difference between the transmitted signal and received signal is usually measured rather than the directly measure the echo of light pulses turn-around time. As in the case of pulsed time-of-flight systems, continuous wave-modulation systems have a maximum unambiguous range. This range is limited to that which causes a phase delay in the sine wave of one complete cycle. The highly accurate ranging systems often have several modulation frequencies. The lower-frequencies are used to prevent an ambiguous range measurement. The higher-frequencies are used for more accuracy. Similar to the optical interferometry, the transmitted modulated light signals of a phase delay τ , reflected from the object is mixed and correlated with the reference signal at the receiver, thus we can have the total depth information of the target:

$$I(\tau) = s(t) * g(t-\tau) = \lim_{\Delta T \rightarrow \infty} \frac{1}{\Delta T} \int_{\Delta T} s(t).g(t-\tau)dt \dots \dots \dots (3.13)$$

Let's consider the reference signal and reflected light signal from the object is $s(t)$ and $g(t)$ respectively. If we ignore the nonlinear effects and the noise behaviour of the systems and assume the sine wave modulation

$$s(t) = a_0 + a_m \cdot \cos(\omega_0 t) \dots \dots \dots (3.14)$$

The reflected signal $g(t)$ can be written with the time delay τ .

$$g(t) = a'_0 + a'_m \cdot \cos[\omega_0(t-\tau)] \dots \dots \dots (3.15)$$

The correlation function $I(\tau)$ can be calculated as

$$\begin{aligned} &= A \cdot [a_0 + a_m \cdot \cos(\omega_0 t)] * [a'_0 + a'_m \cdot \cos(\omega_0(t-\tau))] \\ &= B \cdot [1 + M \cdot \cos(\omega_0 \tau)] \end{aligned}$$

where A defines the system attenuation factor and

$$\begin{aligned} B &= A \cdot a_0 \cdot a'_0 \\ M &= \frac{1}{2} \cdot \frac{a_m \cdot a'_m}{a_0 \cdot a_0} \end{aligned}$$

Different types of methods can be used to determine the time delay τ . Heterodyne technique (frequency shifting), homodyne technique (phase shifting) and FM-chirping modulation technique are the most applied CW- modulation techniques [48]. If we consider the ranging distance of the system less than the half of the RF-wavelength the ambiguity problem is reduced. The accuracy of CW ranging systems is limited by the frequency of the modulation signal; accuracy of the phase-measurement loop that depends on signal strength, noise, and so on; stability of the modulation oscillator and variations in the index of refraction of the air.

3.1.3.3 Pseudo-Noise Modulation TOF technique:

Pseudo-noise modulation technique is the combination of Pulsed modulation and Continuous wave modulation technique [49]. These are periodic, deterministic and binary sequences with a noise like waveform. As it also known pseudo-random, it looks randomly for the user who does not know the code. This Technique gives some advantages over the other two TOF techniques. It gives better optical signal-to-background ratio and larger freedom in choosing modulation signals and components. As it requires

the low mean value of optical power that increases the safety of eyes. Due to these features, Pseudo-noise modulation technique is widely used in the TOF ranging systems.

3.1.4 Comparison between the main optical techniques for Range measurement:

Optical techniques for 3D imaging according to the operation principle, the range and the accuracy can be grouped in the three categories: Triangulation, Interferometry and time-of-flight are described in the previous section. Table: II summarizes comparative study of the different optical measurement techniques. The most important parameters of these systems are the measurement interval and the depth resolution. By using the Interferometry technique the highest resolutions can be achieved and the measured range up to 10m using multi-wavelength technique. However, for this technique very accurate optical alignment is required and these are very expensive systems.

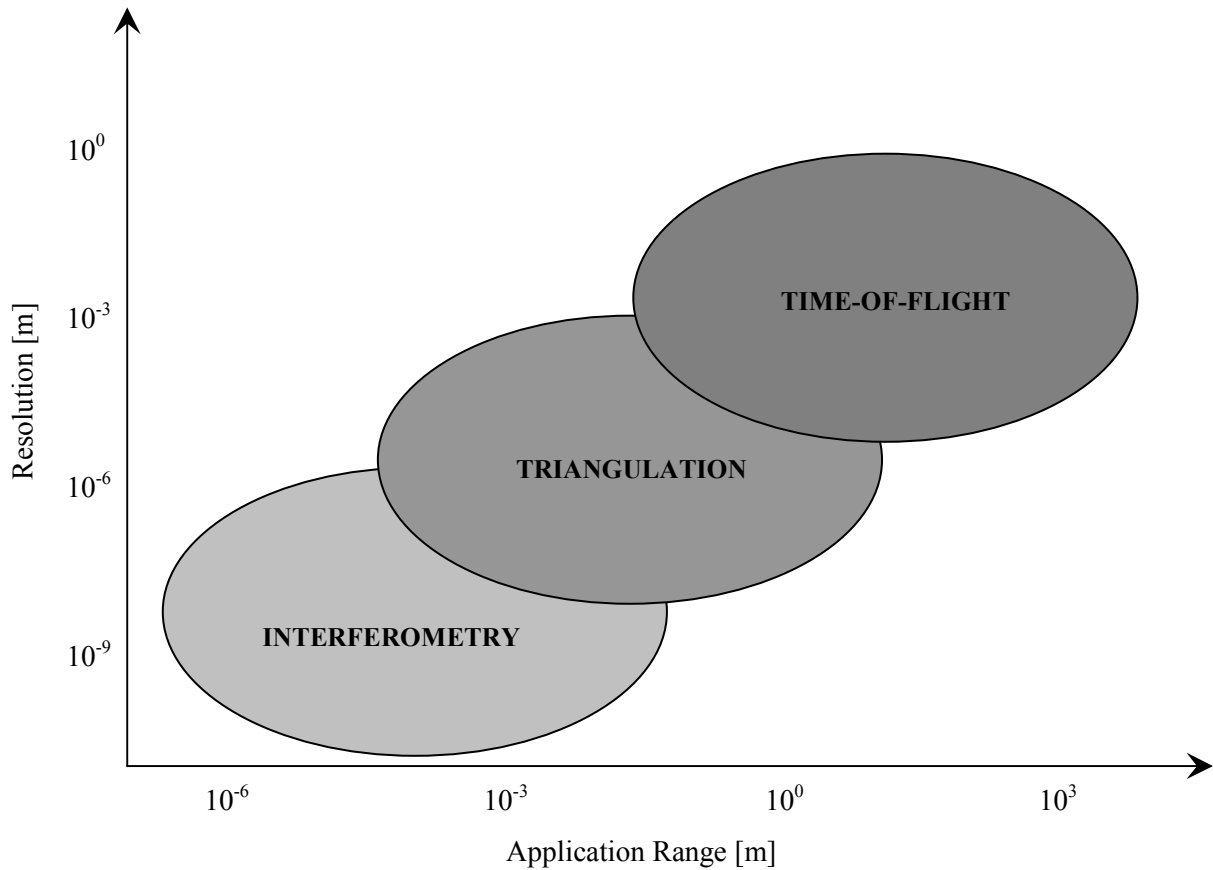


Fig.3.6: Relative resolutions of three types of 3D optical measurement methods.

In the case of triangular method the measurement range is up to several meters where the accuracy depends on the depth of field and it can be less than $10\mu\text{m}$ for small depths. The miniaturization of the complete system reduces the baseline of the triangular thus reducing the accuracy of the system. These systems with the scanner are also expensive and bulky. The time of Flight technique is completely different than other optical ranging measurements. These techniques allow the range measurement from tens of cm up to tens of km. Compare to the other techniques this system is compact, cheaper and the measurement accuracy is steadily improving. The advantage and performance of these ranging techniques presented here tend to be mutually exclusive by their own limited set of situations.

Table II. Comparison between three optical measurement systems

	Triangulation m/d	Interferometry m/d	Time-of-Flight m/d
Measurement Interval	1 mm~ 1km	1mm~1m	10cm~10km
Accuracy	100nm-10um	0.1nm~1um	1mm~1m
Advantages	Good accuracy	Excellent accuracy	Compact and rugged system, low cost, real time image is possible, High dynamic range.
Disadvantages	System with scanner, expensive, heavy and low acquisition speed.	Required accurate optical alignment, expensive, low acquisition speed	Low accuracy

3.2 Time-of-Flight (TOF) based 3D vision sensors:

In recent years, a new generation of active cameras based on the Time-of-Flight principle (TOF) has been developed. This technique acquires the possibility to get data at video frame rates and achieve 3D point clouds without scanning and from just one point of view. TOF based cameras usually deliver an amplitude image and a range image with infrared modulation intensities at video frame rates: the amplitude image contains for each pixel the strength of the reflected signal from the object, while the range image contains for each pixel the radial measured distance between the considered pixel and its projection on the target object. In some cases an intensity image is also delivered, which represents the mean of the total reflected modulated signal and background light of the observed scene incident on the sensor. Several types of TOF based 3D imaging techniques have been demonstrated in previous research works in the scientific literature. The state of the art of TOF based 3D imagers so far reported can be divided in different categories, differing for the type of photodetector use in the pixels:

3.2.1 Standard photodiode is coupled with complex processing circuit:

A standard photodiode coupled with complex readout circuitry is proposed and the indirect time-of-flight is used [50-53]. The scene is illuminated with a train of short (~10s of ns) LASER pulses; the back-reflected light pulses are acquired in each pixel of the sensor through one or more temporal integration windows synchronized with the LASER pulse trigger. This approach can yield an accuracy of a few cm over a maximum range of a few meters. The disadvantages of this approach are- the pixel size, that is quite large due to the number of transistors and capacitors required for signal read-out and processing circuits and the power consumption, so that it is impossible to realize large two-dimensional arrays.

Fig.3.7 shows an ITOF based real time 3D imaging system with standard CMOS photodiode [53]. The laser source is pulsed by the sensor, which is a bi-dimensional array of pixels. A lens is placed in front of the emitter to obtain the proper illumination of the scene, while a camera objective is used to focus the scene onto the detector matrix. A pulse train is emitted for pixel-level signal accumulation and white noise averaging. The first train is integrated according to the timing W_1 and the second one by means of the timing W_2 as shown in figure. Depending on the time-of-flight of the photons reflected by the points of the scene, pixels looking at close objects get their photons earlier than pixels focused on further details; in this case a bigger part of the reflected is lost. For a specific pixel the distance information can be easily extracted by dividing the signals collected after the integration of two pulses. Thus the measured results are independent from the reflectivity condition of the focused point.

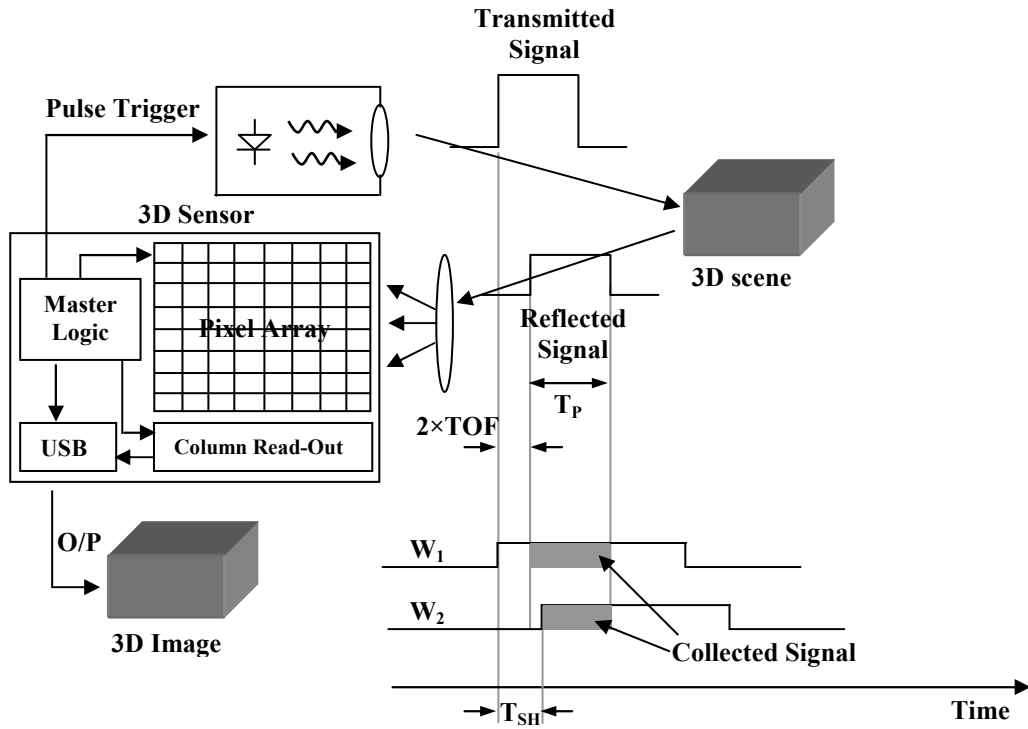


Fig.3.7: Pulsed I-TOF ranging Technique [53]

3.2.2 Photo-demodulator fabricated with special technologies:

The key element of 3D range camera, the photo demodulator is implemented with different types of special technologies such as: CMOS/CCD, CCD and non standard CMOS or hybrid approach. In this demodulator the photogenerated charge is ‘mixed’ on two or more photo-gates thus achieving an intrinsic demodulation effect [54-57]. The advantage is the read-out channel simplicity which results in a small pixel size. The disadvantages are the lower sensitivity due to the presence of the “photo-gate”, the lack of immunity to the ambient light and the cost of the non-standard technology. The CMOS/CCD based TOF range 3D imager is proposed [54]. The pixel size is $65\mu\text{m} \times 21\mu\text{m}$ and the optical fill factor is more than 20%. Fig.3.8 shows the cross sectional view with potential distribution. By applying the suitable gate voltages to the Photogates, the potential gradient in the semiconductor can be influenced. If the voltages of the photogates are changed synchronously with the modulated incoming light, the generated charge carriers can either be integrated under the integration gate or are dumped to the dump diffusion. This process can be repeated until the integration gate has accumulated a sufficiently large signal. Each pixel has its individual amplifier, which can be randomly accessed and reset over on chip address decoder. At 20 MHz modulation frequency, the maximum measurable range of this imager is 7.5m and the achievable ranging accuracy of better than 5cm over the full distance range.

A similar sensor fabricated in CMOS technology and consisting of 64×64 pixels with chip ADC has been developed and commercialized by Canesta Inc [58]. This sensor takes advantage of device-level charge processing to efficiently realize TOF. The sensor has a 64×64 pixel array and is fabricated on a single chip using ordinary, low-cost CMOS process. The sensor chip also integrates an ADC and circuitry to generate the high-speed modulation signals. The sensor achieves a depth resolution of a few millimeters and frame rates of up to 50fps. The sensing part of the imager design is the special pixel structure.

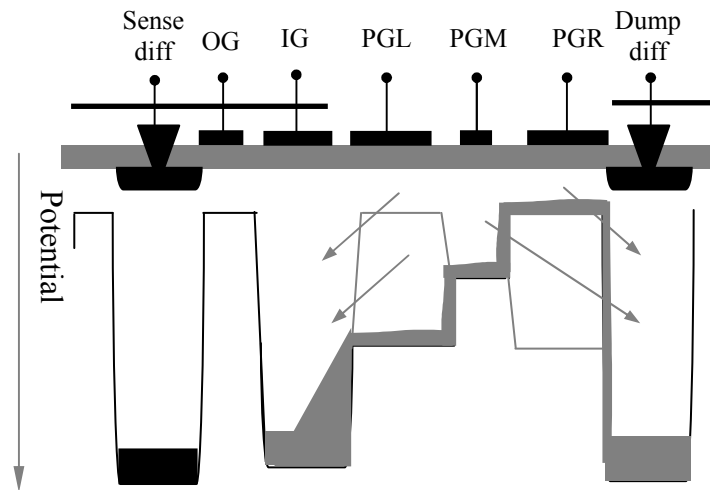


Fig.3.8: Cross sectional view of the CCD part (IG: integration gate PGL/PGM/PGR: left/middle and right photogate) [54]

Fig.3.9 shows the cross-section of the pixel. The differential structure accumulates photo-generated charges in two collection nodes using two modulated gates. The gate modulation signals are synchronized with the light source and depending on the phase of incoming light, one node collects more charges than the other. At the end of integration time, the voltage difference between the two nodes is read out as a measure of the phase of the reflected light. Thus the pixel simultaneously performs the function of mixing and low pass filtering.

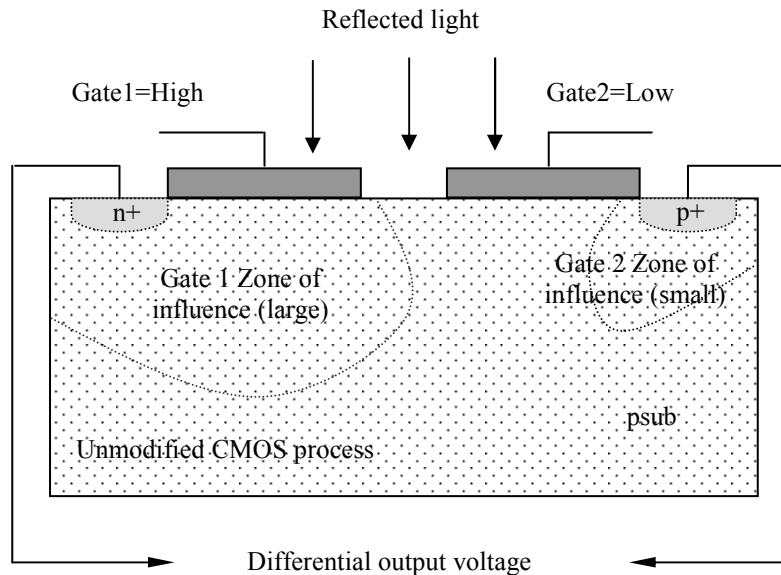


Fig.3.9: Cross section of a pixel [58]

Based on photo-demodulation a sensor is reported [59], which is fabricated by a modified CMOS process to improve the charge mixing efficiency. It provides very good results in terms of pixel size that is 15 μm pitch, 336 \times 252 array size and has an accuracy of about 5cm over a range up to 3m. A novel photo demodulator is proposed [60], which exploits the electric field resulting from the presence of different poly silicon gates each one biased at a different voltage, so as to rapidly mix the photo-generated charge carriers. The reported pixel, fabricated with a 0.6 μm CCD/CMOS technology, has a 40 μm pitch and a 25% fill factor; the distance measurements are achieved in the 50-350 cm range with an accuracy of about 15cm.

3.2.3 Single Photon Avalanche Diode (SPAD) based Imager:

The detector array based on single photon avalanche diodes (SPADs) operating in Geiger mode, measuring the arrival time of the detected photon accurately and are therefore effective in computing TOF of very small optical power even when the source is diffused over a wide cone of light. This approach becomes attractive with the recent integration of SPAD arrays in standard CMOS technology [61]. The cross section of a single photon avalanche diode with readout circuit is shown in Fig.3.10. A quenching resistor R-poly in series between the cathode of the diode and V_{DD} and a comparator are integrated with the SPAD. The diode is formed at p+/n-well junction, where avalanche multiplication takes place. A guard ring is surrounded around the junction to prevent edge breakdown which is obtained by inter diffusion of two n-wells. When a photon reaches the avalanche region a primary electron-hole pair is generated. After the beginning of the avalanche process begins a strong current flow in the junction causing a voltage drop across R-poly. Using the proper voltage V_A at node A, the inter logic switches state stop the avalanche. Once the avalanche current is quenched, the parasitic capacitance starts to recharge and the voltage V_A increases again to V_{DD} . The total time for the quenching and recharging process determines the lowest possible time interval between detectable photons. This time constant is called dead time.

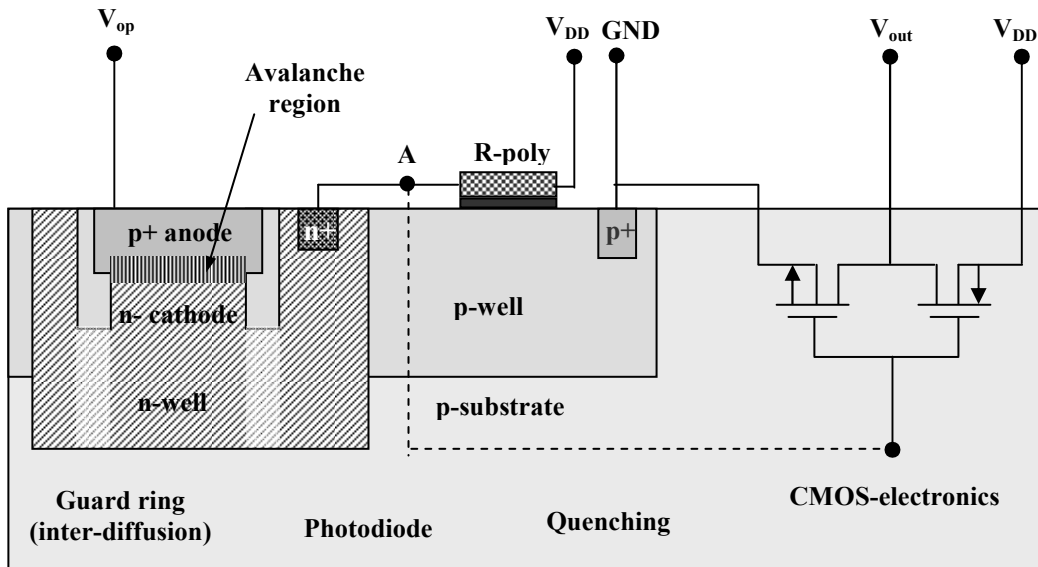


Fig.3.10: Pixel cross sectional views with Readout Circuit [61]

In [62] a 64×64 -pixel array is reported having a $58\mu\text{m}$ pitch but the fill factor is 1%. The distance can be measured on a range of 3.75m with an accuracy of about 2mm. The main limit is that each pixel must be addressed serially, thus delaying the measurement, along with the need for an external time-to-digital converter. The solution proposed in [63] solves these problems and present an analog time-measuring circuit in each pixel, but owing to the amount of processing electronics in the pixel only linear arrays are feasible. The pixel size is $38 \times 180 \mu\text{m}^2$ and each pixel consists of a single photon avalanche diode, a dedicated read out circuit for the arrival-time estimation of incident light pulses. The photodiode is biased above breakdown voltage so that high sensitivity can be achieved exploiting the avalanche phenomenon. The sensor array provides a range map from 2m to 5m with a precision better than 0.75% without external averaging operation.

3.2.4 Photo Mixing Device (PMD) based Imager:

A range of powerful contributions to dynamic 3D-vision, the Photonic Mixer Device (PMD) is an interesting solution that is reported in [64]. The Photo Mixer Device (PMD) combines the process of optical signal conversion and the mixing and correlation process that enables the detection and time of

flight measurement. The charge transfer mechanism of photo mixer device is comparable to that of surface channel charge coupled devices (CCD) with significant differences that have to be considered. In Charge Coupled Devices (CCD) the charge will only be moved in one direction. In the PMD the direction of the charge movement depends on the electrical reference signal. It is changed into push pull signals that are applied to the modulation electrodes. Photogate PMD doesn't storage charges; it serves for a very fast modulated transport and readout. Different implementations of the PMD principle are under development and provide a new family of PMD-detectors which are going to realize the dynamic 3D-vision. The Photo Gate (PG) -PMD is the first implementation of the PMD-principle in low cost CMOS technology. Fig.3.11 schematically illustrates the cross-section of a PMD receiver. The PG-PMD is a low-noise and low-dark-current device, being capable of demodulating very low optical signals at photo current levels.

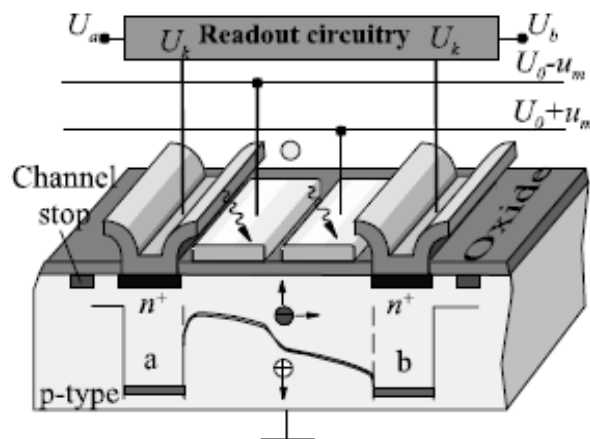


Fig.3.11: Schematic illustrates the cross-section of a PG-PMD receiver [64].

Another PMD implementation is described in which are similar to the PG-PMD but the photo gates are replaced by widening the metal shields ME (Metal Electrode) of the read out electrodes. The main advantage of the ME-PMD is the achievement of an optimized and more homogeneous drift field. It also increases the modulation bandwidth and the device sensitivity is improved by avoiding the optical attenuation of the semitransparent photogates.

Finally, another interesting solution employs a Metal-Semiconductor-Metal photo-detector [64, 65] having a high modulation bandwidth but the sensor is not compatible with CMOS technology and the pixel dimension is $250\mu\text{m}$ which is quite large with low fill factor. Typical MSM photodiodes implement in a slightly doped semiconductor bulk with interdigitated metal fingers on top. The selected semiconductor and metal have work functions leading to a Schottky contact. Fig.3.12 shows a schematic of a typical MSM PMD photodiode. Basically, modulation functionality is achieved by varying the applied bias voltage across the Schottky contact. This results in sensitivity or gain modulation of the device. The photo current polarity of this symmetrical photo diode depends on the polarity of the supply voltage $\pm u_m$. The average of photo current of the non-correlated background light goes to zero on both coupling capacitors C_m . The required correlated photo current leads to a unidirectional photo current causing an anti-symmetrical charge on C_{ma} and C_{mb} . This current is collected by the readout circuitry over a low pass filter to separate the high frequency modulation voltage.

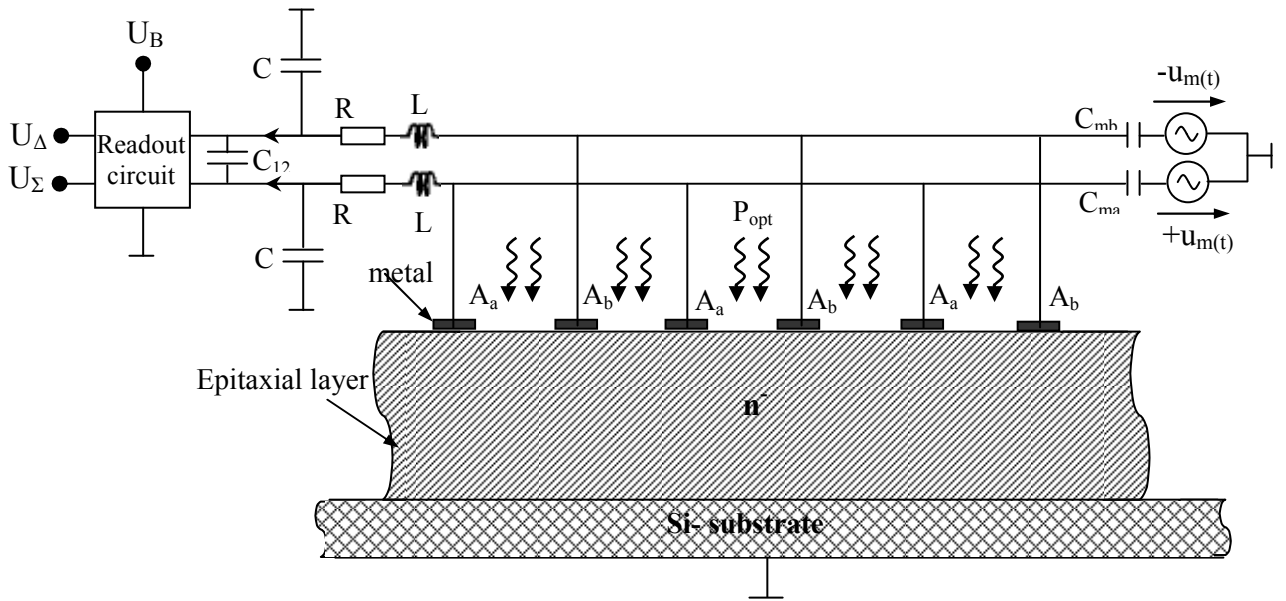


Fig.3.12: Cross-sectional view of finger structure MSM-PMD [64]

3.2.5 Gates-on-Field Oxide structure based CMOS Range Image Sensor:

To achieve TOF based charge integration, the proposed pixel utilizes polysilicon gates on field oxide to realize high-speed charge transfer structures, while maintaining the compatibility to standard CMOS process [66]. In the proposed charge draining structure, charge due to background light, which is mixed into the signal charge, is reduced by using a small duty-cycle light pulse and draining the charge for most of the time in one cycle. Fig.3.13 shows the cross-sectional view and layout design of the proposed device. The photogate, PG is the photosensitive region of the pixel. Aside from PG, the other gates are used to control the direction of photoelectron flow according to their TOF. TX1, TX2 and TXD are also polysilicon gates placed on field oxide. FD1 and FD2 are floating diffusions used to collect signal charges from PG through transfer gates TX1 and TX2 respectively. Unwanted background light induced photoelectrons are transferred to the two charge drains through the charge draining gates TXD.

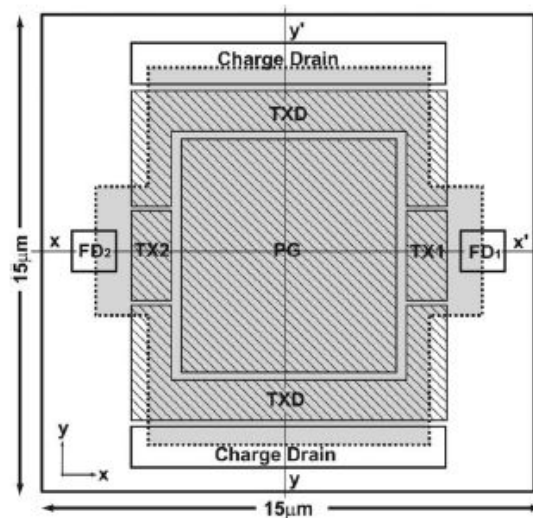


Fig.3.13 layout design of a Gates-on-Field Oxide structure based Imager [66]

The proposed CMOS TOF sensor consist of 84672 pixels with a gates-on-field oxide structure with fill factor of each pixel is 19%. Range measurements are achieved by TOF dependant charge separation. A new range equation is developed for this technique and for the first time the dependency on range resolution to PSN is mathematically derived, calculated, and proven through measurements. A linear distance range between 1.6–12.3m measured to 1.9% accuracy is achievable for a constant measured signal intensity of 0.55 V. The best range resolution measured is 2.35 cm with light pulse width of 100 ns at 30 fps.

3.2.6 Field Assisted CMOS Photo-Demodulator based 3D imaging:

In this novel device [67], owing to the presence of an electric field resulting from the flow of a majority carrier current between two modulation electrodes V_{md1} and V_{md2} , the photogenerated charge is guided towards two collection electrodes V_{cd1} and V_{cd2} . The majority carrier current and the electrical field are induced due to the potential difference between two modulation electrodes. The induced electric field is guided the photo generated charge towards one of the two collecting electrodes. A very good responsivity of 0.32 A/W at 860nm and high demodulation efficiency of about 99% at low frequency can be achieved. Fig.3.14 shows the schematic of a field assisted photo-demodulator.

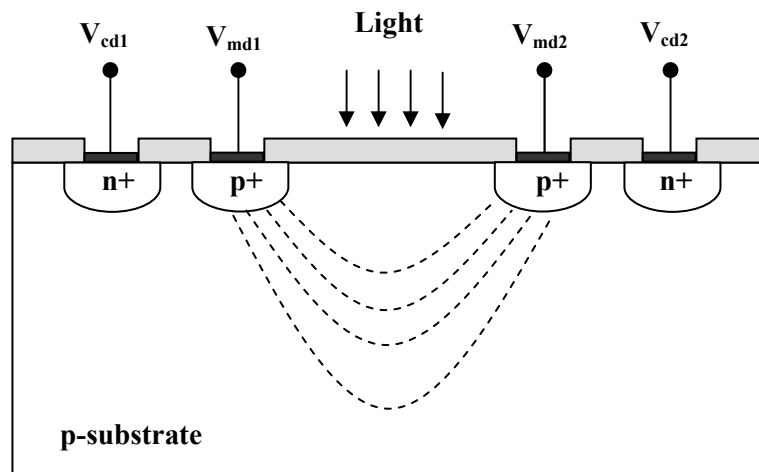


Fig.3.14 Schematic cross section of a Current Assisted Photonic Demodulator.

The readout of the collected charge at the two electrodes can be done in charge-integrating mode as in conventional photodiodes and the circuit complexity of the pixel can be reduced. The device sensitivity can be optimally adjusted as a function of the incident optical power by adding one control electrode that is particularly useful for imaging deep scenes [68]. The main drawback of this device is the power dissipation arising from the modulation current of the device. A trade off between speed of operation and power dissipation is necessary when dealing with large 2D pixel arrays. Another field-assisted charge collection mechanism has also been proposed for other active pixels to be used for charged particle tracking and electron microscopy [69].

Table -III: Performance Comparison Table different types of 3D imager research

Sensor Introduced by	Photodiode Type	Process Technology	Pixel Resolution	Pixel Size	Fill Factor	Advantages	Disadvantages
David Stoppa et.al.[53]	Standard Photodiode	0.35 μ m CMOS Technology	50 \times 30 array	81.9 \times 81.7 μ m ²	20%	Can yield an accuracy of few cm over a maximum range of few meters.	Large pixel size, Higher power consumption
Robert Lange et.al [54]	Photo gate type photodiode	CCD/CMOS hybrid technology	64 \times 25 array	21 \times 65 μ m ²	22%	Simplicity of readout channel, small pixel size	Lower sensitivity, costly because of non standard technology is used
Bernhard Buttgen et.al [60]	Photo-demodulator structure with poly Si gate	0.6 μ m CCD/CMOS technology	176 \times 144 array	40 \times 40 μ m ²	25%	Low power consumption, fast charge transportation and high optical fill factor.	Layout complexity
Cristiano Niclass et.al. [62]	Single photon avalanche Photodiode	0.80 μ m CMOS technology	64 \times 64 array	58 \times 58 μ m ²	1%	Distance can be measured on a range of 3.75m with an accuracy of about 2 mm	Each pixel must be addressed serially; thus delaying the measurement.
Shoji Kawahito et.al [66]	Gate-on-Field –Oxide structure	0.35 μ m CMOS technology	336 \times 252 array	15 \times 15 μ m ²	19%	Range resolution 2.35cm at 30fps	Lower modulation frequency
Daniel Van Nieuwenhove et.al [68]	Current Assisted Photonic Demodulator	0.35 μ m CMOS technology	N/D	30 \times 25 μ m ²	N/D	Very good sensitivity, high demodulation efficiency	Power dissipation arising from the modulation current.

Chapter 04

Test Structures and Characterizations

The test structures provide an easy way to investigate the initial characteristics of a new device. To get a preliminary idea of current assisted photo mixing demodulator characteristics different topological and geometrical structures are fabricated in custom process technology at Fondazione Bruno Kessler (FBK), Trento, Italy. Although this technology is quite different from standard CMOS process technology, the availability of the geometrical characterizations and process details will allow the simulations to be optimized. Once the test device satisfies the specific characteristics of operation, a prototype TOF based current assisted photo mixing demodulator 3D image sensor is designed incorporating full testability features at device and system levels and fabricated in standard CMOS technology. In the following section we will describe different types of photo mixing device, its optical and electrical characteristics fabricated in custom technology.

4.1 High Resistivity Current Assisted Photo mixing Device (CAPD):

The electro-optical mixer in different geometries and topologies based on substrate current modulation is fabricated in a custom technology on high resistivity silicon substrates [70]. A set of test devices was fabricated at FBK on high resistivity n-type silicon substrate with $2 \times 10^{12} \text{ cm}^{-3}$ doping concentration. The substrate doping is reduced in order to decrease the modulation current and thus the power dissipation. Although the use of p-type substrate could lead to a larger bandwidth, these test structures are fabricated on an n-type substrate in order to get the primary idea on current assisted photonic demodulator characteristics with a simple fabrication process. Different layouts of test devices are fabricated in FBK such as: linear shaped CAPD consisting of two collecting electrodes, square shaped CAPD device with single collecting electrode and multiple collecting electrodes based CAPD device.

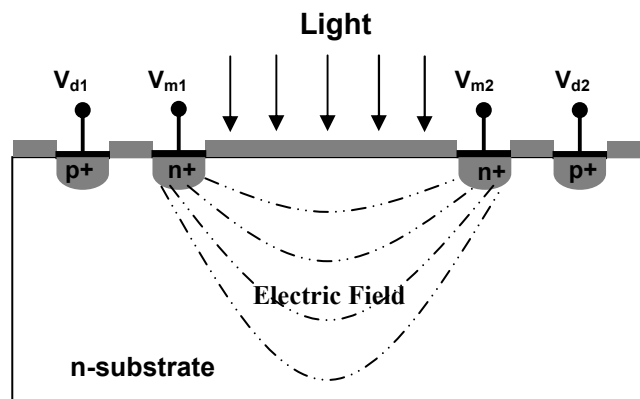


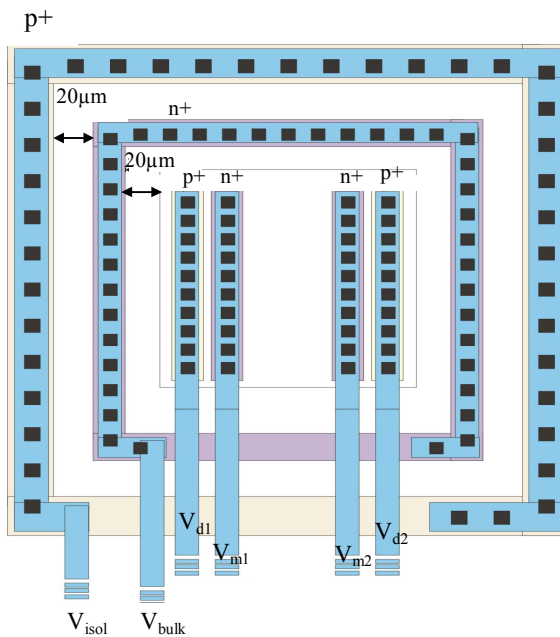
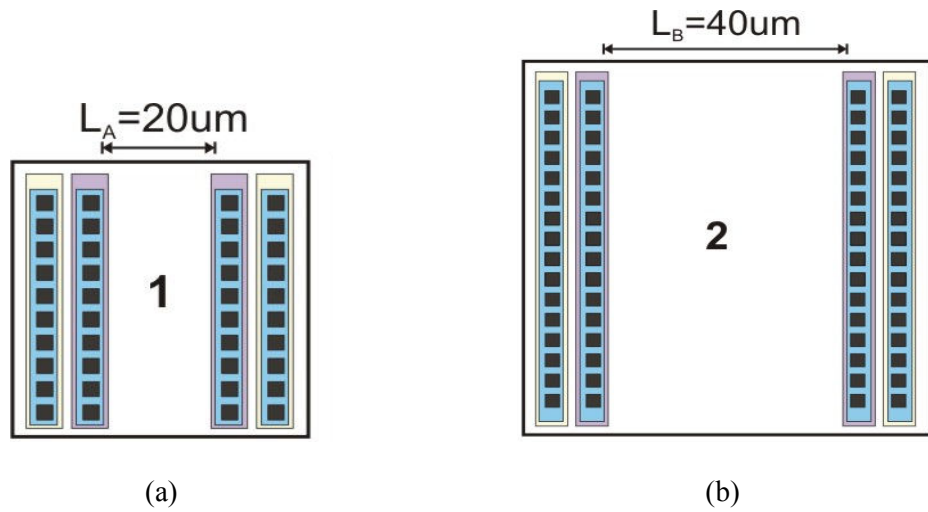
Fig.4.1: Cross sectional view of high resistivity linear-shaped CAPD

4.1.1 Device structure and operation of Linear-shaped CAPD:

The architecture of the linear-shaped demodulator is implemented in custom process technology at FBK. Two different configurations are fabricated; in one structure (CAPD1) the distance between two modulating electrodes is $20\mu\text{m}$ and in the second structure (CAPD2) the distance between two modulating electrodes is $40\mu\text{m}$. The width of both p+ and n+ implants is $5\mu\text{m}$.

Fig.4.1 shows the cross sectional view of the linear-shaped CAPD device. It contains four electrodes, V_{d1} and V_{d2} are the collecting electrodes to collect the photo generated charge carriers and V_{m1} and V_{m2} are modulating electrodes where the potential is applied. The substrate of this device is n-type high resistivity

silicon to reduce the high power consumption due to the majority current flow in the substrate. The collecting electrodes consist of two shallow p+ implantation and n+ implantation for the modulating electrodes. Each pixel must be surrounded by an n+ bulk-contact, shared along the array. This implant is placed at a minimum distance of about 20 μm from the pixel boundary. For the better isolation a p+ ring is also placed around the n+ bulk-contact maintaining the distance of about 20 μm . Fig.4.2 shows the layout design of the linear-shaped CAPD device.



(c)

Fig.4.2: Layout design of the linear-shaped CAPD (a) distance between two modulating electrodes is 20 μm (b) distance between two modulating electrodes is 40 μm (c) linear-shaped CAPD layout with bulk and isolation electrodes.

The electric field is formed in the substrate by applying a potential difference between the modulating electrodes. When the light impinges on the device, the electric field guides the photo-generated charge carriers towards one of the two collecting electrodes. In this structure the modulated electric field is not limited to the surface of the device, thus the collection charge carriers generated deep inside the substrate.

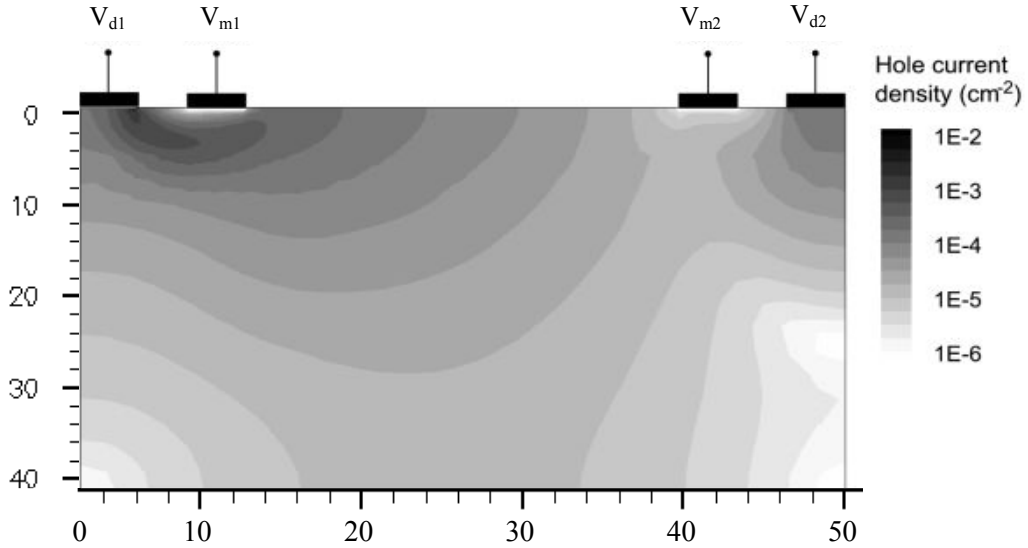


Fig.4.3: Hole current density of CAPD1

The behaviour of this device has been investigated by using the device simulator ISE-TCAD. Fig.4.3 shows the hole current density of CAPD1 with a 0.5V voltage difference applied to the modulating electrodes and a 780 nm light incident on the device surface. Most of the generated holes move toward the collecting electrode V_{d1} , guided by the electric field.

4.1.2 Characterization of Linear-shaped CAPD:

For the static characterization, the voltage applied to the modulating electrode V_{md2} is swept from 0V to 2V, while the voltage of modulating electrode V_{md1} is maintained at 1V. The collecting electrodes are biased at a constant voltage of 0V. A wide-spectrum lamp was used to illuminate the device. As can be seen in Fig.4.4, the transfer characteristic shows a good DC charge separation efficiency near to 100% for the CAPD1 device. The asymmetry in the electrical characteristics is due to the asymmetry to the device bias.

The average current measurement at the collecting electrodes and the dynamic demodulation contrast of the test devices CAPD1 and CAPD2 are characterized. In this measurement, the ring voltage (V_{bulk}) has been maintained constant at 1V. The guard ring (V_{isol}) and the collection diode were biased at 0V, which is shown in Fig.4.2(c). For this measurement two sine wave signals have been used with an arbitrary phase delay $\Delta\phi$ at different frequencies. A function generator is used to generate three sine wave signals with appropriate synchronization. One of the three signals is used to modulate a laser emitter with an arbitrary phase delay $\Delta\phi$. The other two signals are connected to the modulating electrodes V_{md1} and V_{md2} with 180° phase shift. Also in this case the collecting electrodes are biased at a constant voltage of 0V. To measure the average current, a 650nm red laser with a flat frequency response within the band of interest and 87% modulation depth was used to illuminate the test device.

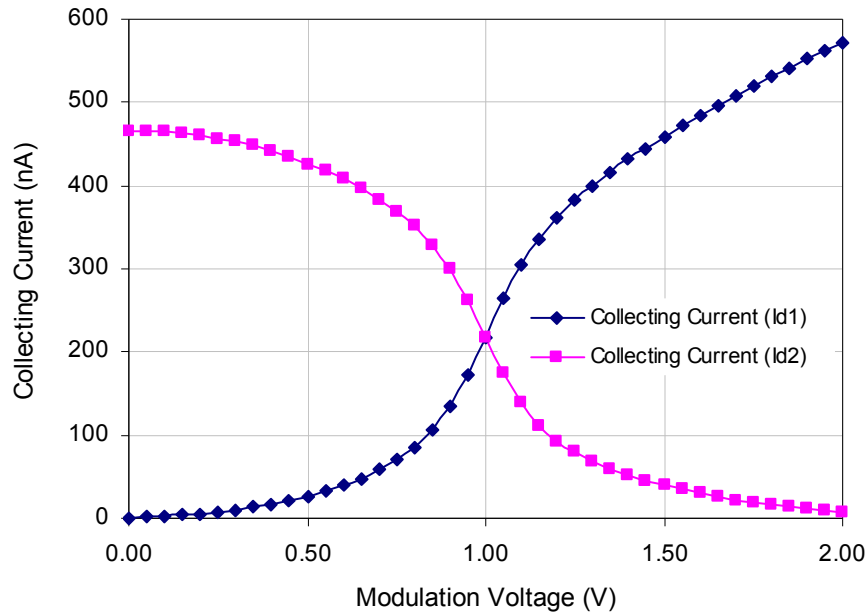


Fig.4.4: DC Charge transfer characteristic of CAPD1

The current flowing through the collecting electrode was read out with a Pico-ammeter at different modulation voltages and frequencies. Fig.4.5 shows the demodulation contrast of the photo mixing device CAPD1 at different voltages and frequencies. The Demodulation Contrast (DC) in optics is defined as the ratio between the amplitude and the average value of the measured signal.

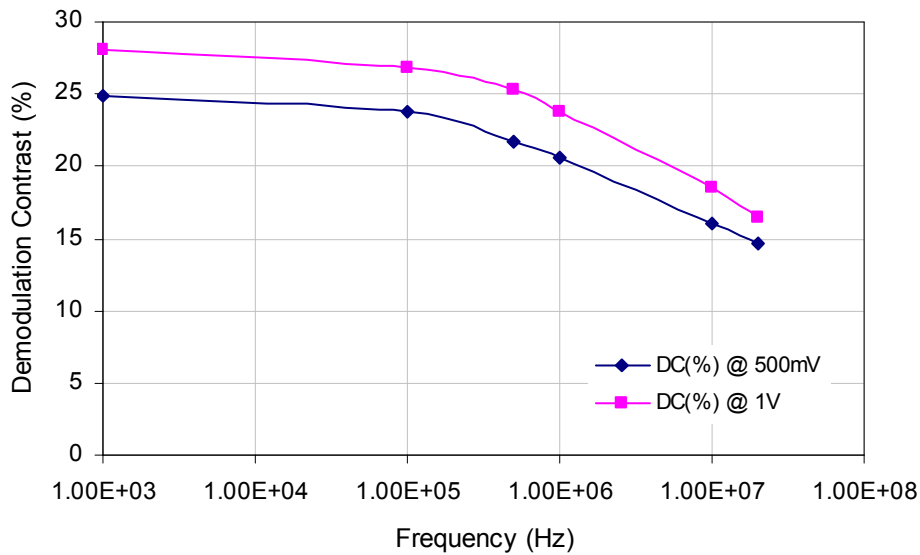


Fig.4.5: Dynamic Demodulation Contrast of CAPD1 at different Voltage

The above figure shows that the obtained demodulation contrast decreases at high frequencies. At long-wavelength, photoelectrons are generated deeper in the semiconductor which is far from the electrically active zone need time to reach the demodulating electric field. This temporal delay in arrival time leads to decrease in modulation contrast for high frequencies. At the same modulating voltage, increasing the active area of the CAPD basically increases the sensitivity of the device and thus clearly boosts up the modulation contrast of the device. Fig.4.6 shows the demodulation contrast of linear-shaped high resistivity CAPD at the different dimension.

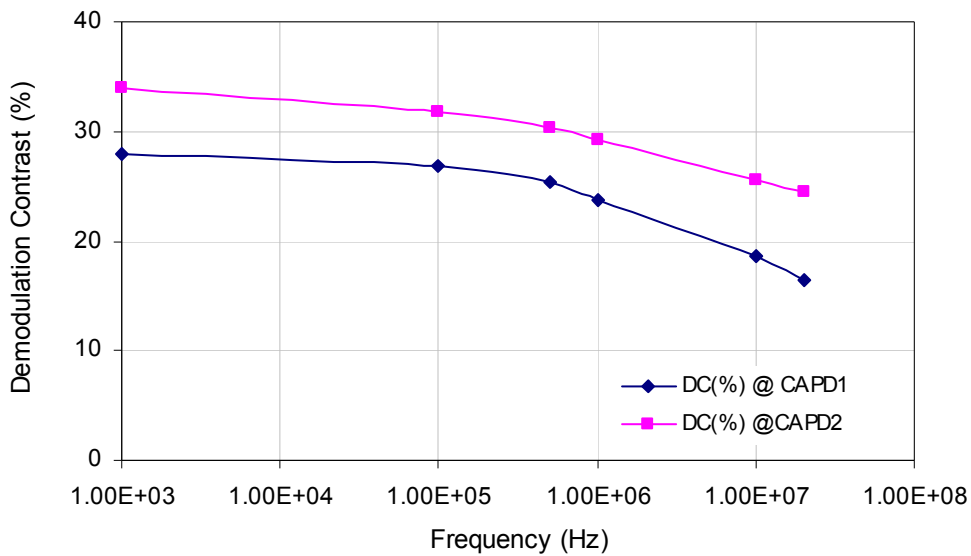
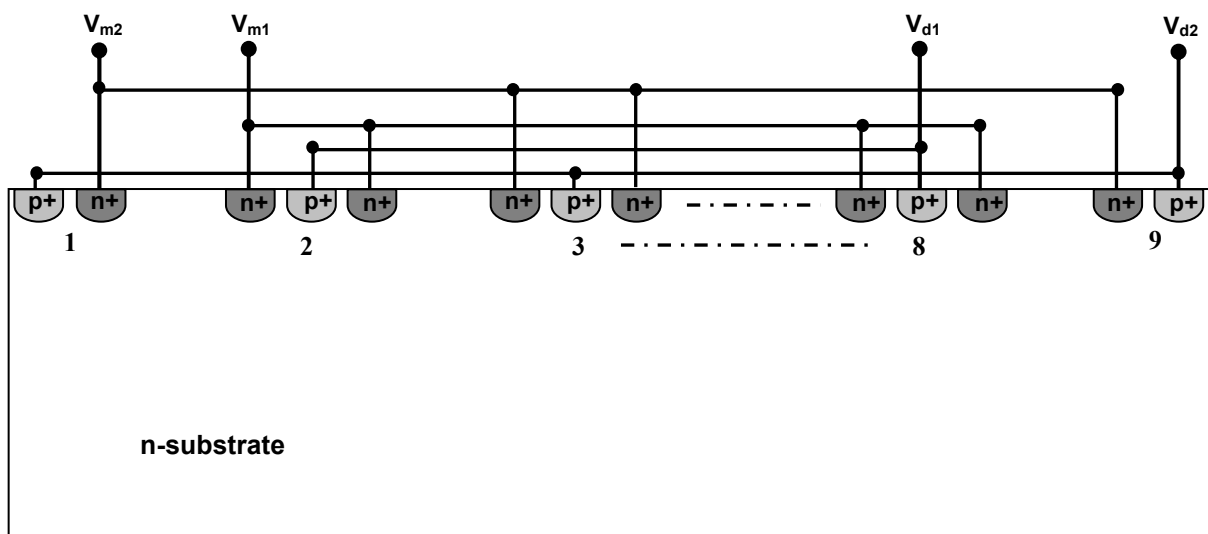


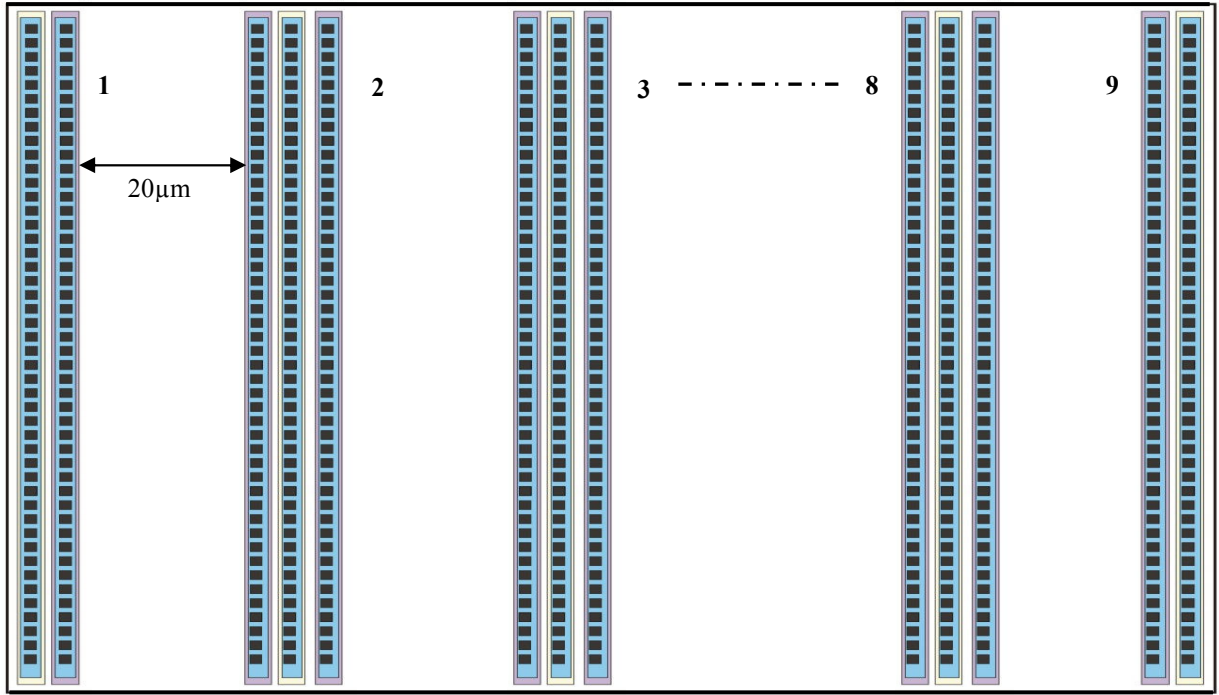
Fig.4.6: Dynamic Demodulation Contrast of two CAPD devices at different geometries

4.1.3 Device structure, operation and characteristics of a Multiple-strip based CAPD:

This device consists of fingered type electrodes i.e. multi tap CAPD device. Fig.4.7 (a) and (b) shows the cross sectional view and the layout of the device, respectively. It consists of nine detection electrodes. Among these detection electrodes, the seven central regions (as shown in Fig.4.7 from region 2 to region 8) consist of a detection junction and two substrate contacts. The rest of detection regions contain one detection junction and one substrate contact, like the region 1 and 9 shown in Fig.4.7.



(a)



(b)

Fig.4.7: (a) Cross sectional view of multiple strip CAPD and (b) Device layout

All of the substrate contacts and the detection junctions are connected as shown in the device cross sectional diagram. Finally this device has four electrodes, two collecting electrodes (V_{d1} and V_{d2}) that are connected to the detection junction and two modulating electrodes (V_{m1} and V_{m2}) that are connected to the device substrate. The collecting electrode V_{d1} and the modulating electrode V_{m1} are connected to the 2, 4, 6 and 8 regions according to the detection junctions and substrate contacts.

On the other hand, the collecting electrode V_{id2} and the modulating electrode V_{mod2} are connected to the region 1, 3, 5, 7 and 9 accordingly. This device is also surrounded by an n+ bulk-contact, shared along the array and placed at a minimum distance of about $20\mu\text{m}$ from the pixel boundary. A p+ ring is placed surround the n+ bulk-contact maintaining the distance of about $20\mu\text{m}$ for better isolation. The total area of this device is $400\mu\text{m} \times 400\mu\text{m}$. The distance between the adjacent modulating electrodes is $20\mu\text{m}$.

In this device an effective potential gradient is applied to the multiple modulating electrodes that speed up the signal charges transferring to the detection regions. The potential $\Delta V = V_{m2} \sim V_{m1}$ defines at which region the hole current is detected. The operational behaviour of the multi tap device is investigated by using the device simulation software ISE-TCAD. Fig.4.8 shows the hole current density of this device with a voltage difference applied between two modulating electrodes and a 780 nm light incident on the device surface. Most of the generated holes move toward the collecting electrode V_{d1} , guided by the electric field. In this simulation picture, it shows the region 1, 2 and 3 according to the cross sectional view of the device shown in Fig.4.7.

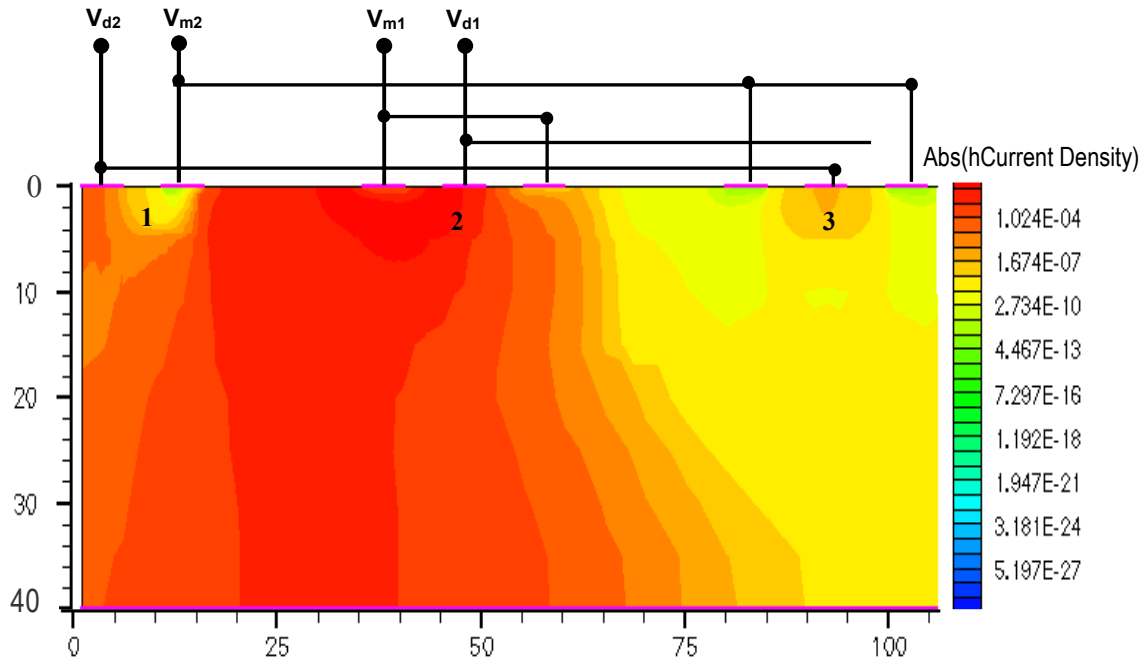


Fig.4.8: Hole current density of Multiple CAPD device

The modulating voltage ΔV allows demodulation of the photonic signal, without having to switch the totality of the electric field. These results in an increase of the demodulation speed: the carriers are always guided towards the centre of the device and demodulated there. If $V_{mod2} > V_{mod1}$ the hole current is detected in V_{id2} region, for $V_{mod1} > V_{mod2}$ it moves to the opposite detection region. As the collecting electrodes for V_{id1} and V_{id2} are not equal, the DC characteristics of this device are not symmetrical as linear-shaped CAPD. Fig.4.9 shows the DC characteristics of the device under the illumination of wide spectrum light, it illustrates a good DC charge separation efficiency.

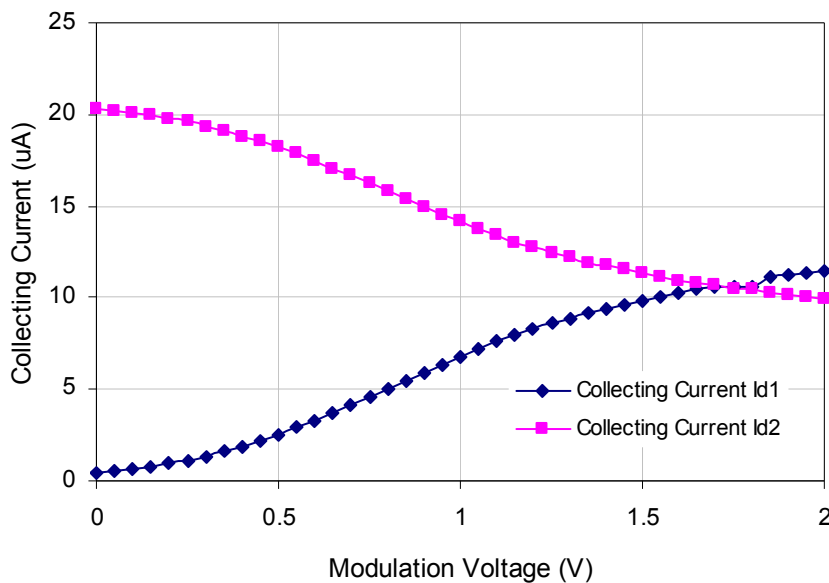


Fig.4.9: DC characteristics of the device under the illumination of wide spectrum light.

Fig.4.10 shows the growth of demodulation contrast for the multi-tap device as a function of different modulation voltage. Different demodulation frequencies are considered in this case. Increasing the modulation voltage in essence increases strength of the electric field and it clearly enhances the modulation contrast of the device. The area of the multi tap device is larger than the linear shaped CAPD

device and its modulating potential is distributed over the whole substrate, thus increasing the charge transfer efficiency and demodulation contrast of this device.

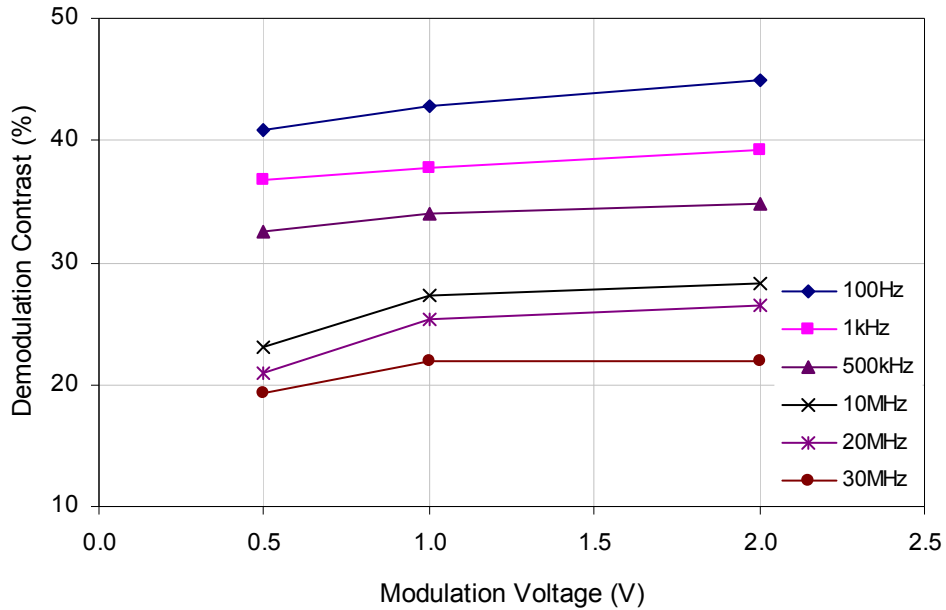
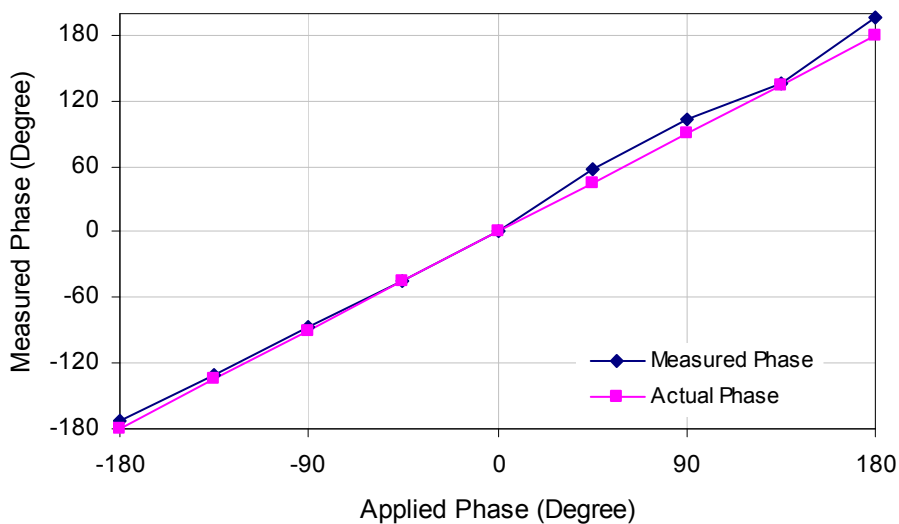


Fig.4.10: Growth of demodulation contrast for multi-strip device as a function of different modulation voltage

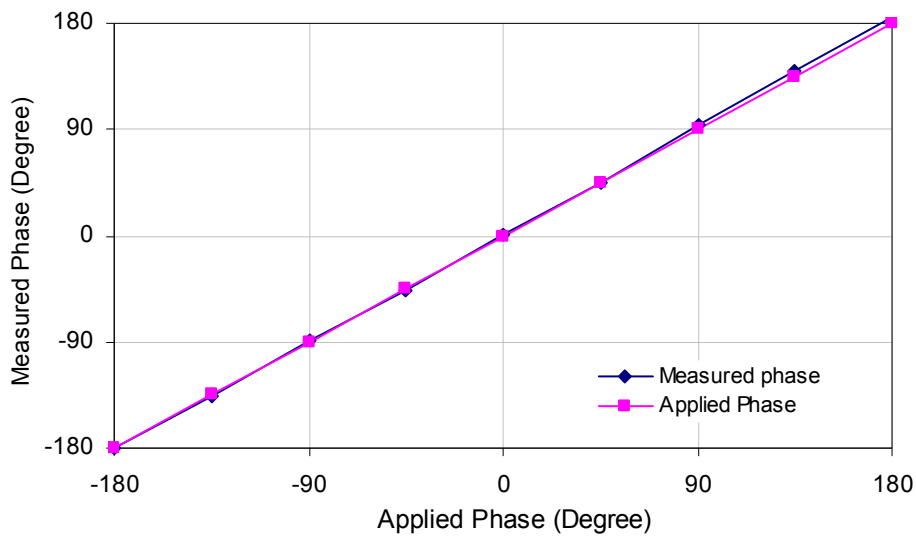
4.1.4 Non-linearity measurement of the linear-shaped CAPD and Multi-tap CAPD:

A set of phase measurements is performed on the device CAPD1 and multiple strip CAPD devices. In these measurements a variable phase delay $\Delta\varphi$ is applied between two modulating electrodes and the laser input to illuminate the device. The value $\Delta\varphi$ can be recovered acquiring four amplitude measurements with four different phase shifts $\theta_1 - \theta_4$ applied to the modulated laser signal. These phase shifts were $-180^\circ, -90^\circ, 0^\circ$ and $+90^\circ$, respectively, and the four amplitudes measured, represented by the average DC currents, $I(\theta_1) - I(\theta_4)$, are used in Equation given below to calculate the phase delay $\Delta\varphi$:

$$\Delta\varphi = \arctan \frac{I(\theta_1) - I(\theta_3)}{I(\theta_2) - I(\theta_4)}$$



(a)



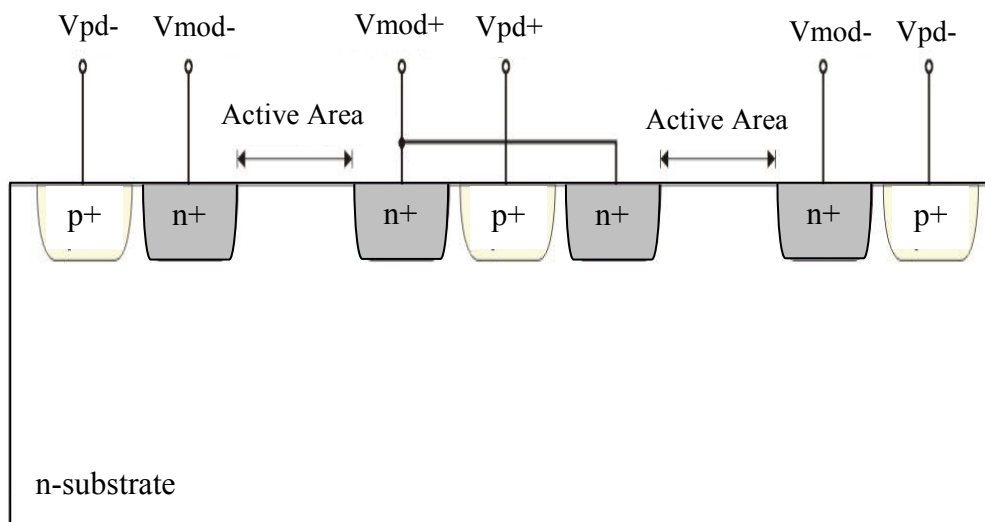
(b)

Fig.4.11: Phase linearity measurement (a) for Linear shaped CPAD1 (b) Multiple Strip CAPD

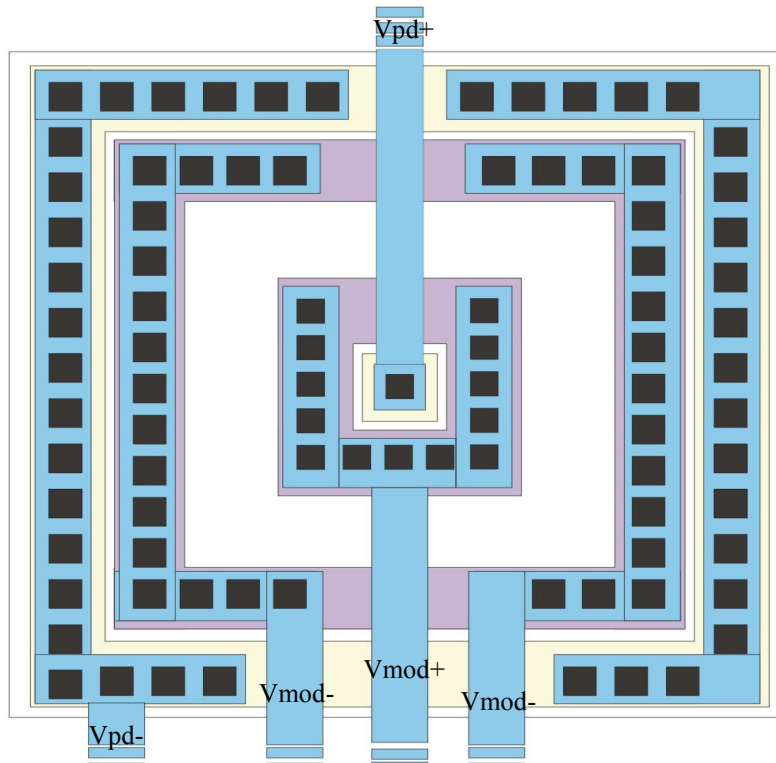
The measurement is performed considering sinusoidal wave modulation signals at 20 MHz, and the resulting phase is reported in Fig.4.11 (a) and (b) for CAPD1 and Multiple strips CAPD respectively. The maximum linearity error of linear shaped and multi strip CAPD device is 28% and 3.9 % for sinusoidal wave modulation respectively.

4.1.5 Device architecture and Operation characteristics of a Square shaped CAPD:

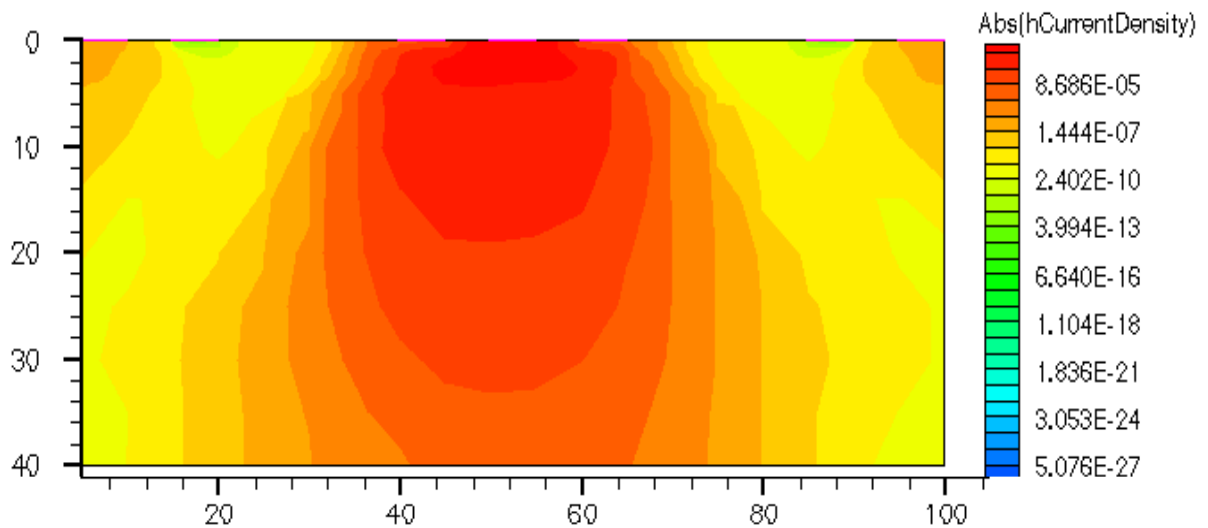
In Fig.4.12 (a) cross sectional view and layouts are shown for the square shaped CAPD implementations. It consists of a detection region at the centre of the device. This detection region consists of a detection junction and two substrate contacts. The rest of detection regions contain one detection junction and one substrate contact. The distance between two substrate contacts, i.e. the modulation electrode, is $20\mu\text{m}$. As the substrate contact of this device is not uniform, the applied drift field will not be spread equally over the sensitive area, thus lowering the speed of the device.



(a)



(b)



(c)

Fig.4.12: Square shaped CAPD Device (a) Cross sectional View (b) Device layout (c) Hole current density for square shaped CAPD

This device is surrounded by an n+ bulk ring apart from the pixel boundary of about 20 μ m. A p+ ring is also placed surround the n+ bulk-contact keeping a distance of about 20 μ m for device isolation as shown in Fig.4.2 for linear shaped CPAD. Based on the operation characteristics of the square shaped CAPD device, Fig.4.12(c) shows the hole current density of the device when the voltage at Vmod+ is greater than Vmod-. According to the CAPD principle and depending on the modulating voltage, holes are generated by light impinging on the substrate are transferred to the detecting junction. The transfer mechanism is drift, provided by the electric field induced in the substrate.

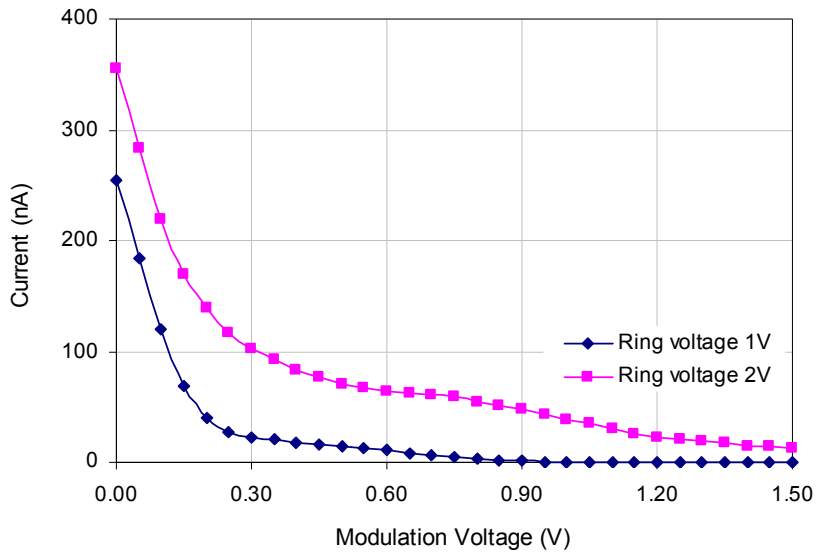
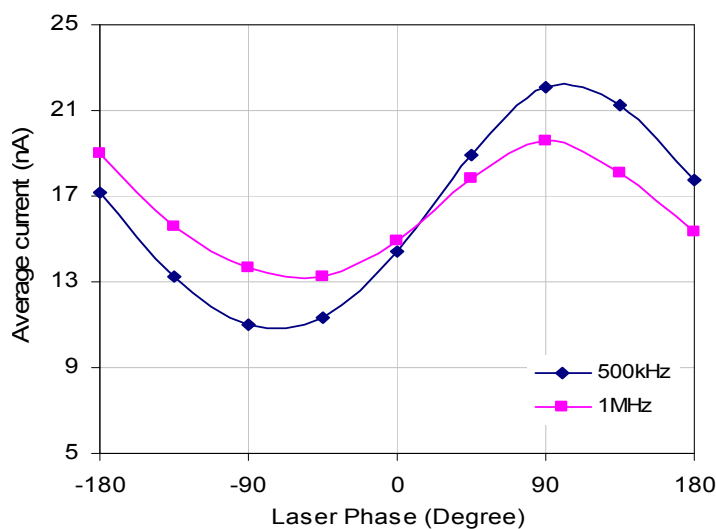


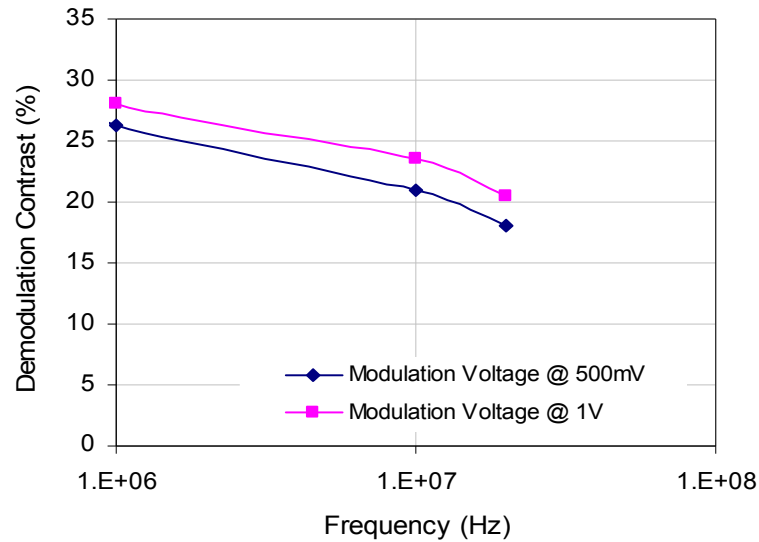
Fig.4.13: DC current at the collection diode of device at two different ring voltages.

The current measured at the collection electrode (Vpd+) of square shaped device under wide spectrum illumination lamp is shown in Fig.4.13. In this measurement, the ring voltage is maintained constant, while the modulation voltage is swept from 0V to 1.5V. The collection electrodes are biased at 0V. The effect of an increase in the ring voltage is a shift of the curve to the right. Also in this case the DC charge separation efficiency can reach values more than 90%.

The dynamic demodulation contrast is characterized of this device same as before for the other two devices. A dual-output function generator is used to generate two sine-wave signals with an arbitrary phase delay $\Delta\phi$. One of the two signals has been used to modulate a laser emitter, while the other is connected to the input of the dual output pseudo differential amplifier to get an output of 180° phase shift. The output of this amplifier is connected to the modulation electrode of the square shaped CAPD device. The DC current flowing through the collection electrode is read out with a Pico-ammeter. The electrodes are biased as in dc measurements. A 650nm red laser with a flat frequency response from in the band of interest and near to 90% modulation depth is used to illuminate the test device. A sine-wave modulation voltage with 500mV and 1V amplitude is applied to the device. The DC current measured at several phases of the laser modulated signal is reported in Fig.4.14 (a) at 500 kHz and 1 MHz modulation frequency. In both cases an excellent fit is obtained using a sine-wave signal.



(a)



(b)

Fig.4.14: (a) Measured average current at two modulation frequencies (b) Measured Demodulation Contrast

The ratio between the amplitude and the average value of the measured sine-wave known as demodulation contrast is reported in Fig.4.14 (b) as a function of frequency, taking into account the effect of the laser modulation depth. The low value of dynamic demodulation contrast with respect to measured DC contrast could be explained by the presence of holes generated in the chip outside the active device area reaching the collection electrode by diffusion. A metal screening of the other light sensitive areas would therefore improve the measured device characteristics.

On the basis of the outcome of device simulation and the preliminary results of the test devices, which were fabricated by FBK, a linear-shaped demodulator model seemed suitable for further investigation in terms of small device size, moderate fill factor and overall device performance. A behavioural model has been developed for the current demodulator, suitable to be incorporated into a circuit simulator cadence and adopted for simulating at circuit level with read out channel. The numerical device simulation results and the results from the circuit simulations have shown a very good agreement in both DC and transient analysis. The result of the electrical and optical characterizations will be used to optimize the devices, and also it helped us to design a CMOS based current assisted photo mixing demodulator.

Chapter-05

Current Assisted Photo mixing Demodulator in standard CMOS Technology

CMOS imaging technology provides the potential to integrate image processing and it is capable of achieving substantial image data. The presented CMOS optical ranging sensor makes use of a current assisted photonic mixing device with an integrated circuit to measure time-of-flight. In this device, an electric field is used to drive photo generated minority carriers from deep into the substrate towards a collecting junction. This picks up detector sensitivity and speed, and allows large sensitive area. As a test vehicle, 10×10 pixel arrays have been fabricated with a $0.18 \mu\text{m}$ CMOS technology. Remarkably, small pixel size of $10 \times 10 \mu\text{m}^2$ has been achieved. In this chapter, the device charge separation efficiency and demodulation capabilities are described up to modulation frequency larger than 20 MHz. The impact of important parameters such as wavelength, modulation frequency and voltage on this test device is also experimentally evaluated in this chapter.

5.1 Device Architecture:

The device functionality of the Current Assisted Photon Mixing Demodulator is investigated using the finite element software ISE-TCAD and the code DESSIS 8.0 (Synopsys Inc.) in order to evaluate the device capability of reaching the required high responsivity as well as high demodulation bandwidth. Both DC and dynamic performance are simulated. This simulation is adopted, in particular for, i) the comparative evaluation of different technological options, such as substrate doping for power consumption reduction and junction depth ii) the device geometry and layout, by comparing different layout topologies including linear, interdigitated and circular structures with optimizing of each topology in dimension and spacing of charge collecting and charge modulating electrodes and iii) finally predict the effect of an additional n-type electrode for sensitivity control and dynamic range enhancement.

A schematic cross section of the fabricated device is shown in Fig.5.1. It contains four electrodes: C1 and C2 are the electrodes aimed at collecting the photo generated charge carriers, whereas M1 and M2 are the modulating electrodes where the potential is applied.

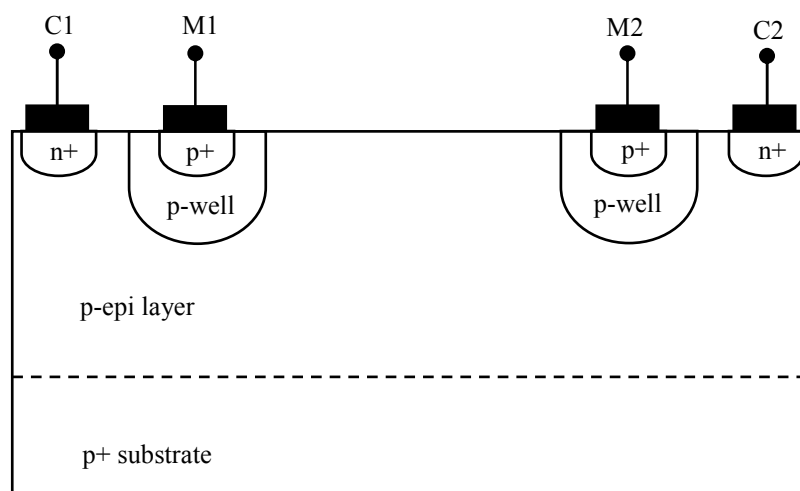


Fig.5.1: Device Cross sectional view (not to scale).

The simulator solves the drift-diffusion transport model. Photo-generation effects are accounted for by including appropriate terms into the carrier continuity equations [71]. The photonic mixing demodulator is fabricated in $0.18 \mu\text{m}$ standard CMOS technology. Process details such as layer thicknesses, junction

depths and sheet resistances have been integrated into simulations as accurately as possible, by relying on information provided by the silicon foundry. The 3D simulation domain of a photodetector is shown in Fig.5.2 (b) for a $10 \times 10 \mu\text{m}^2$ pixel. Fig.5.2 (c) and Fig.5.2 (a) show the corresponding top and ISE-TCAD cross-sectional views respectively. Thickness and resistivity of the p-type epitaxial layer are $7 \mu\text{m}$ and $20 \Omega\text{cm}$ respectively. The distance between the two modulation junctions is $4 \mu\text{m}$ for the $10 \times 10 \mu\text{m}^2$ pixel. Detecting junctions are kept at the minimum distance from the adjacent modulation junctions allowed by the technology. The area of the optical window is $6 \times 4 \mu\text{m}^2$, the remaining pixel area being covered by a metal light shield. The fill factor is 24%. Different structures have been evaluated, having different pixel pitch and corresponding M1-M2 and C1-C2 distances. The $10 \times 10 \mu\text{m}^2$ pixel shown in Fig. 5.2(b) is the smallest that has been taken into consideration. Decreasing the distance between M1 and M2 increases the device bandwidth [67]. This allows the higher frequency operation. This comes, however, at the expense of reduced DC demodulation contrast (for same power consumption) as a consequence of the decreased ohmic drop and electric field between the two modulation electrodes.

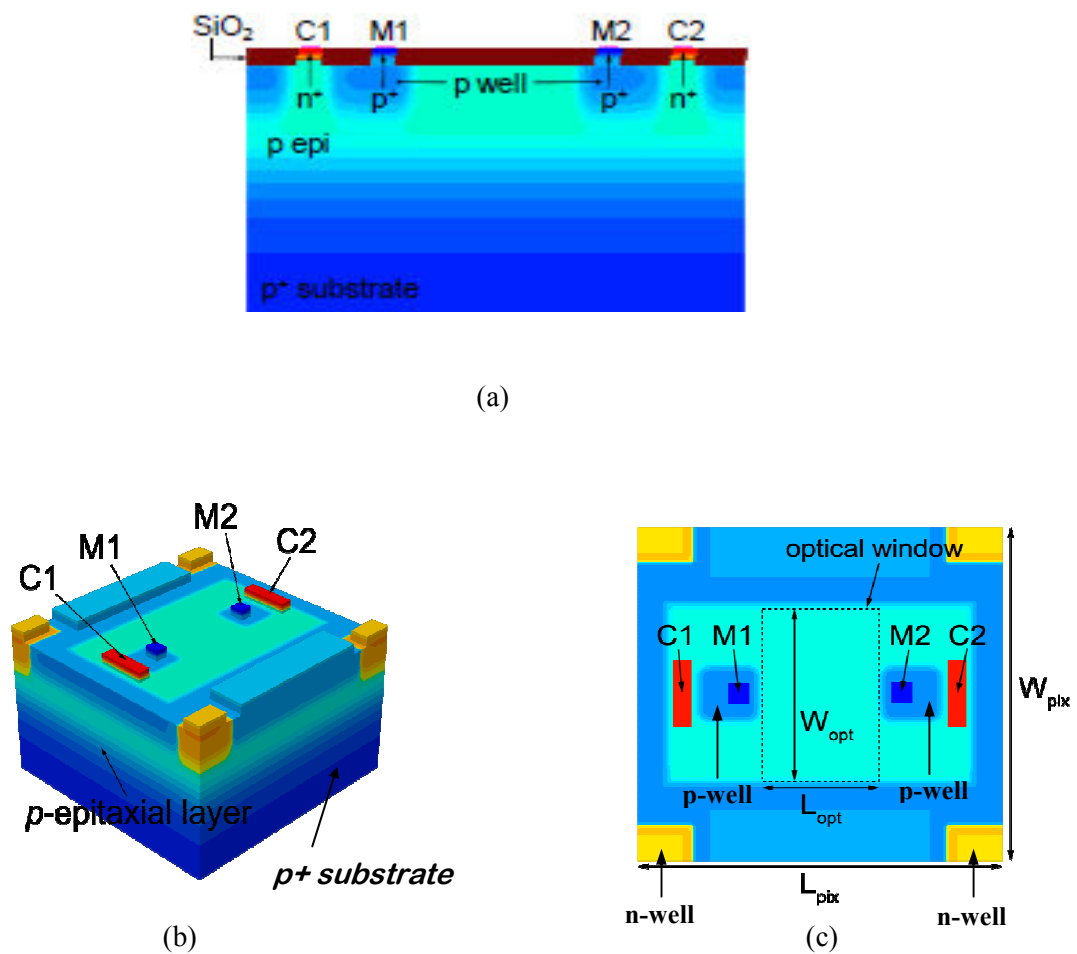


Fig.5.2: (a) Cross-sectional view (b) 3D geometry of CAPD and (c) top view of the CAPD pixel. In (a) the SiO₂ passivation layer is omitted.

As shown in Fig.5.2 a p-well region surrounds the CAPD, while n-well regions are placed at the four corners of the simulated structure. In actual pixels, these p- and n-well regions contain readout transistors accomplishing output current integration. It is important to include the effects of p and n-well regions into simulations for two reasons: (i) n-well regions act as electron collecting junctions potentially competing with C1 and C2; (ii) p-well regions perturb the demodulating electric field applied through M1 and M2 and can therefore adversely impact the demodulation contrast. Device simulations actually allowed us to define a pixel geometry that minimizes the detrimental effects resulting from both (i) and (ii).

5.2 Operation principle and Charge transfer:

The Current Assisted Photonic Mixing device is based on a majority current associated drift field. With zero voltage applied between M1 and M2, due to the symmetry of the structure, equal amounts of photogenerated electrons are collected by C1 and C2. If a voltage is applied between M1 and M2, a hole current is induced between the two modulation electrodes, generating an ohmic drop through the p-type epitaxial layer. The resulting electric field guides the photogenerated electrons preferentially towards either C1 or C2 depending on the applied voltage polarity. When $V_{M1} > V_{M2}$, a majority current carrier generates and forms an electric field in the substrate. When the light impinges on the device, the majority current and the induced electric field separate the photo-generated electron-hole pairs. The separated hole becomes the part of the majority hole current which is generated by the applied voltage on modulating electrode. The hole current moves towards the p+ region and the electron is guided by the same electric field to the collecting electrode C1 and thus the charge is detected. Fig.5.3 shows the simulated electron current density with a voltage difference applied to the modulating electrodes (M1 & M2) and a 780 nm light beam incident on the device surface. At the reverse potential ($V_{M1} < V_{M2}$) the photo-generated charge carriers are swept away from the collecting electrode C1 to C2.

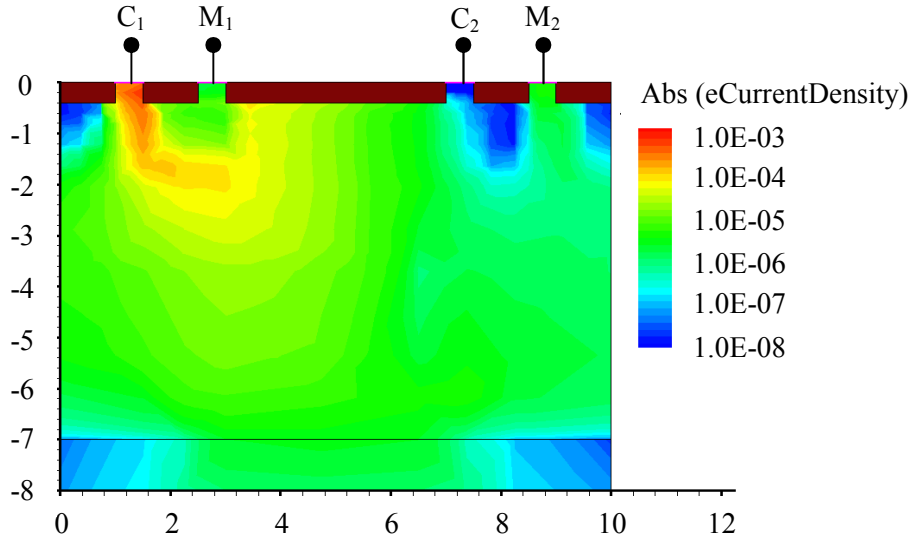


Fig.5.3: Simulated electron current density under illumination

To get a relationship between AC and DC demodulation contrast, assuming no extra collecting junctions compete with C1 and C2 within the pixel structure and no considerable photocurrent is collected from adjacent pixels, currents at the C1 and C2 terminals can be written as:

$$I_{C1} = f_{C1} I_{TOT} \quad (5.1)$$

$$I_{C2} = (1 - f_{C1}) I_{TOT}$$

where, I_{TOT} is the total pixel photocurrent ($I_{TOT} = I_{C1} + I_{C2}$) and f_{C1} is the fraction of I_{TOT} that is collected by C1.

If a sinusoidal-modulated light is used to illuminate the scene, then I_{TOT} can be written as:

$$I_{TOT} = I_{TOT}^{DC} + I_{TOT}^{AC} \sin(2\pi ft - \varphi) \quad (5.2)$$

where, I_{TOT}^{DC} and I_{TOT}^{AC} are the amplitudes of the DC and AC components of I_{TOT} , f is the modulation

frequency, and φ is the phase difference between the light detected by the sensor and the one emitted by the illuminator. Ideally, $I_{TOT}^{DC} = I_{TOT}^{AC}$. In practice, background light, non-unity modulation depth of the illuminator, and roll-off of the AC component amplitude at high modulation frequencies make $I_{TOT}^{AC} < I_{TOT}^{DC}$. From φ , the distance d of the illuminated scene point is readily obtained as:

$$d = \frac{c\varphi}{4\pi f} \quad (5.3)$$

where, c is the light velocity.

When a sinusoidal voltage (V_{M12}) is applied between M1 and M2, also f_{C1} varies with time, alternately transferring photocurrent from C1 to C2 and vice versa. V_{M12} is generated of the same frequency and in phase with the modulated light used to illuminate the scene, i.e.

$$V_{M12} = V_{M12}^{AC} \sin(2\pi ft). \quad (5.4)$$

In the approximation that f_{C1} depends linearly on V_{M12} (valid rigorously for small V_{M12} values only), the time dependence of f_{C1} is sinusoidal too and can be expressed as

$$f_{C1} \approx \frac{1}{2} + f_{C1}^{AC} \sin(2\pi ft), \quad (5.5)$$

where, f_{C1}^{AC} is the amplitude of the AC component of f_{C1} . The DC component of f_{C1} is 0.5, so that, as imposed by the CAPD symmetry, $I_{C1} = I_{C2}$ at time instants when $V_{M12} = 0$.

Introducing (5.2) and (5.5) into (6.1) yields:

$$\begin{aligned} I_{C1} &= \left[\frac{1}{2} + f_{C1}^{AC} \sin(2\pi ft) \right] \cdot \left[I_{TOT}^{DC} + I_{TOT}^{AC} \sin(2\pi ft - \varphi) \right] \\ I_{C2} &= \left[\frac{1}{2} - f_{C1}^{AC} \sin(2\pi ft) \right] \cdot \left[I_{TOT}^{DC} + I_{TOT}^{AC} \sin(2\pi ft - \varphi) \right] \end{aligned} \quad (5.6)$$

From (5.6), the DC component of I_{C1} and I_{C2} can be obtained as:

$$\begin{aligned} \langle I_{C1} \rangle &= \frac{1}{2} I_{TOT}^{DC} + \frac{1}{2} f_{C1}^{AC} I_{TOT}^{AC} \cos \varphi \\ \langle I_{C2} \rangle &= \frac{1}{2} I_{TOT}^{DC} - \frac{1}{2} f_{C1}^{AC} I_{TOT}^{AC} \cos \varphi \end{aligned} \quad (5.7)$$

As can be noted, both $\langle I_{C1} \rangle$ and $\langle I_{C2} \rangle$ directly contain the distance information φ . They can be obtained from the output currents I_{C1} and I_{C2} by filtering out their AC components at frequencies f and $2f$. This low-pass filtering can be accomplished at pixel level by simply integrating the output currents (5.6). Either a single-ended or a differential readout scheme can be adopted.

The demodulation contrast is the total output-signal change normalized to the output-signal average. From (5.7), it can be expressed as (5.8) regardless of whether either $\langle I_{C1} \rangle$ or $\langle I_{C2} \rangle$ is adopted as output

signal.

$$C_d = f_{C1}^{AC} \frac{I_{TOT}^{AC}}{I_{TOT}^{DC}} \quad (5.8)$$

5.3 Device performance and Experimental results:

The electro-optical characteristics are performed on a current assisted photonic mixing demodulator implemented in standard CMOS 0.18 μ m technology. The layout of the single device and a 10 \times 10 array is shown in Fig.5.4 (a) and 5.4(b), respectively.

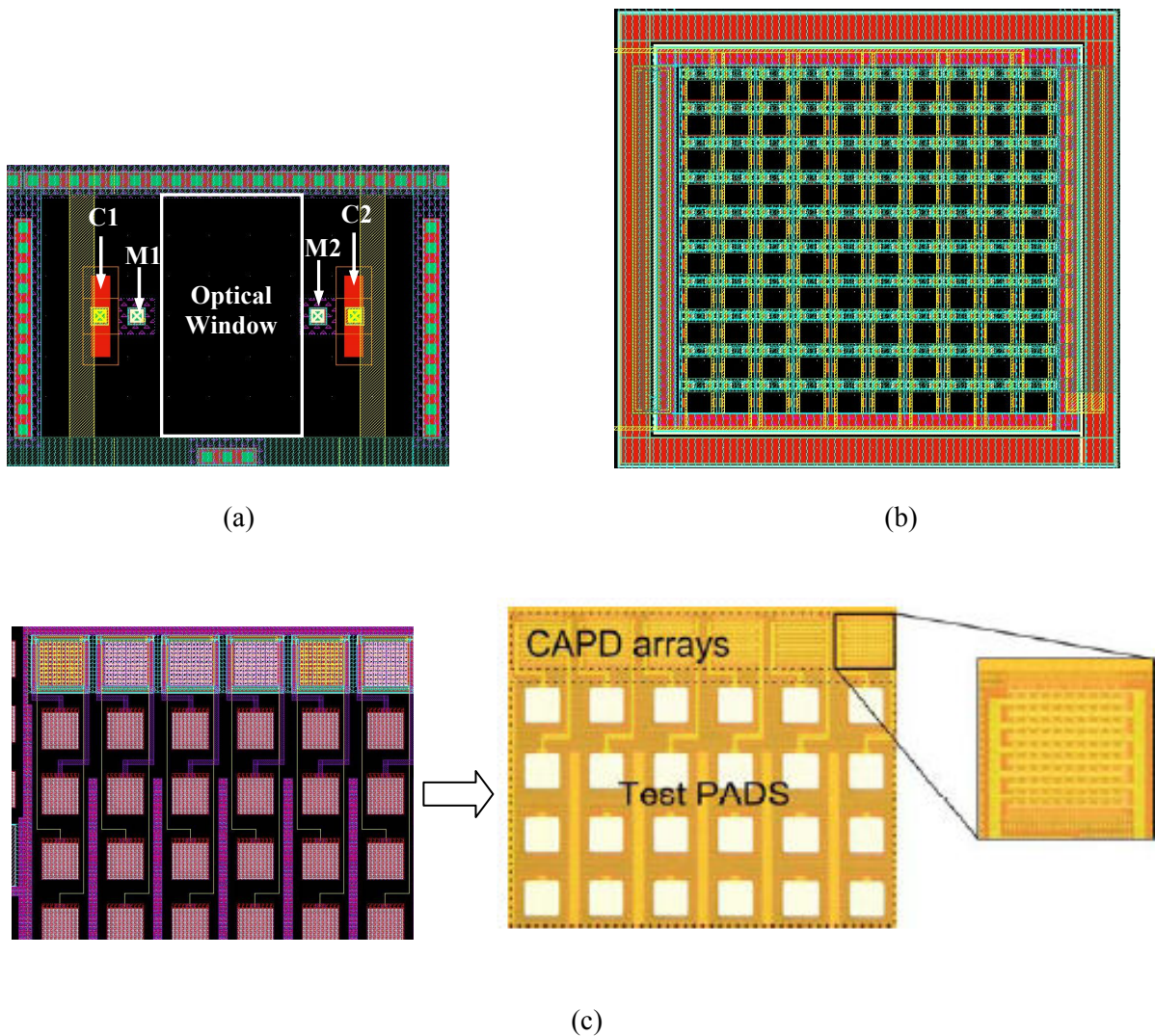


Fig.5.4: (a) single device layout (b) 10 \times 10 pixel array layout and (c) Layout and Micro-photograph of the fabricated test structure.

A microphotograph of the fabricated test structures is shown in Fig.5.4(c). To ease readout of detected currents, several 10 \times 10 arrays of 10- μ m CAPD arranged in serpentine as shown in the inset of Fig.5.4(c) and wired in parallel were included in the test chip. In this way, the currents to be measured are 100 times larger and the information about the average behaviour of a single device is easily retrieved. The

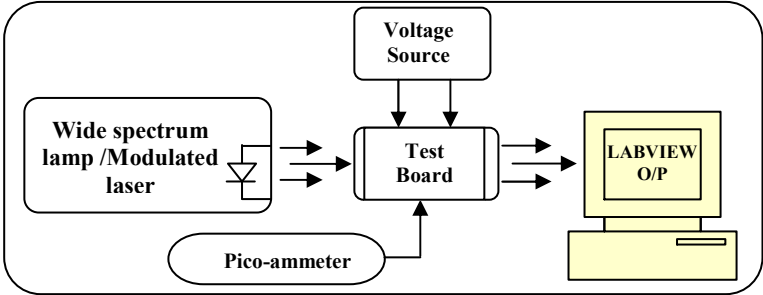
resistance between the modulation electrodes of the current assisted photo mixing demodulator is 250Ω. In these structures the applied drift field will spread equally over the sensitive area.

5.3.1 Device Characterizations:

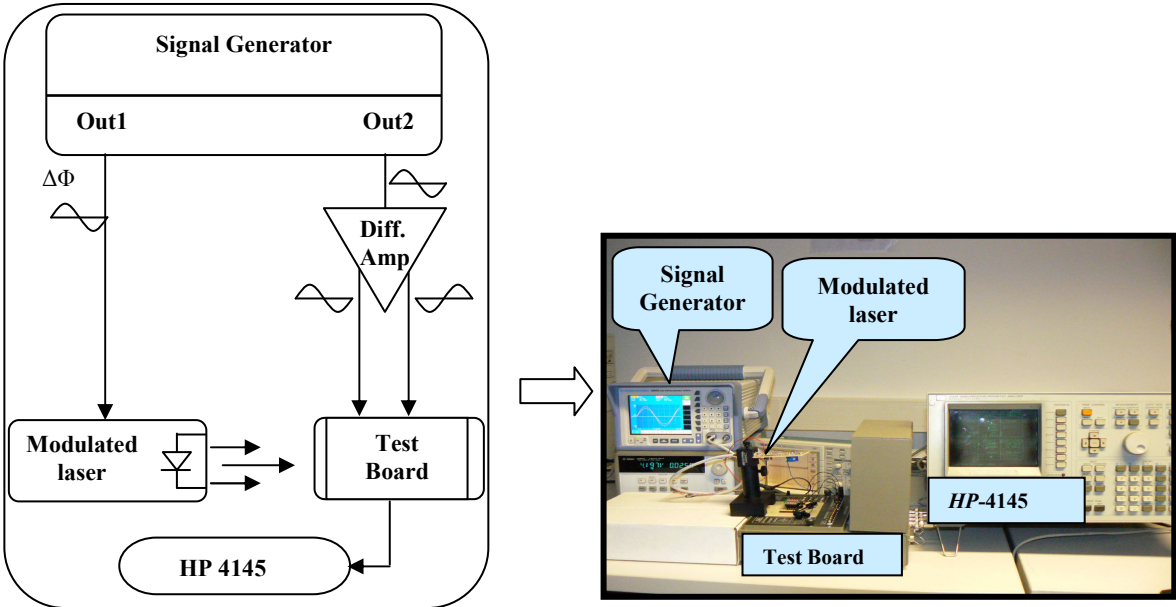
After the fabrication of the test device chip at a commercial silicon foundry by using 0.18μm CMOS process technology, a thorough characterization is carried out including: electrical measurement of the test structures for the process parameters, electro-optical tests of the photo-demodulator such as static and dynamic characteristics.

5.3.1.1 Measurement setup:

Fig.5.5 (a) shows the set up for the measurement of DC characterization of the test device. For the DC characteristics analysis the device is illuminated with a wide spectrum lamp. In this measurement the required voltage at different electrodes can be supplied by a voltage source. A Pico ammeter is used to read out the detection current.



(a)



(b)

Fig.5.5: Experimental setup for (a) DC characterizations & (b) Dynamic characterizations

The average current measurement at the collecting electrodes and the dynamic demodulation contrast is characterized for the test device by using the set up is shown in Fig.5.5 (b). A dual output signal generator is used to generate two sine wave signals. One of the two signals is used to modulate a laser emitter and the other is connected to the input of a differential amplifier. Two output signals of the amplifier with 180° phase shift are connected to the modulating of electrodes. The detection current through the collecting electrodes are read out by a *HP 4145* Semiconductor Parameter Analyzer. For this measurement, three sine wave signals are used with an appropriate synchronization. For this purpose, the optimal design solutions are implemented at different levels. At first the test bench is setup; the PCB board for the electro-optical characterization of the device and circuit is designed, realized and tested. The software programs for the interface with PC and the data acquisition is developed with LABVIEW.

5.3.1.2 Optical input and modulation signal:

In this measurement, stable and high quality optical and modulation signals are required. Both optical and modulation signals are sine-wave providing a wide range frequency modulation more than 40MHz with high accurate phase shifting. It is quite difficult to get the satisfactory modulated optical output signal within the whole modulation frequency range. The average current is measured under a 650nm red laser with 90% modulation depth used to illuminate the test device at different modulation frequencies. Fig.5.6 shows the different signals for laser and modulation electrodes. Here (a) is the modulation signal for Laser input and (b) is the device modulation input.

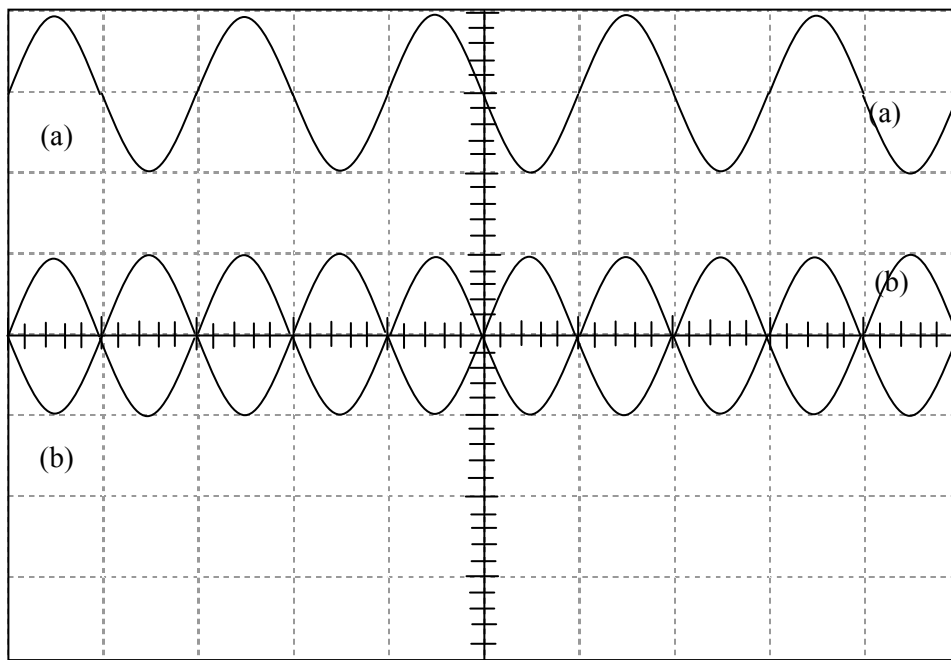


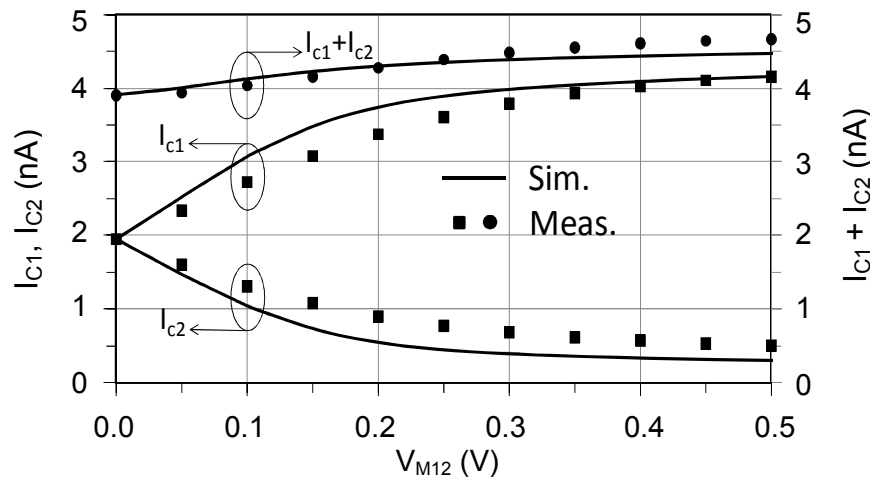
Fig.5.6: Optical signal (a) Modulation signals for Laser and (b) Device Modulation Input.

5.3.1.3 Static and Dynamic performance:

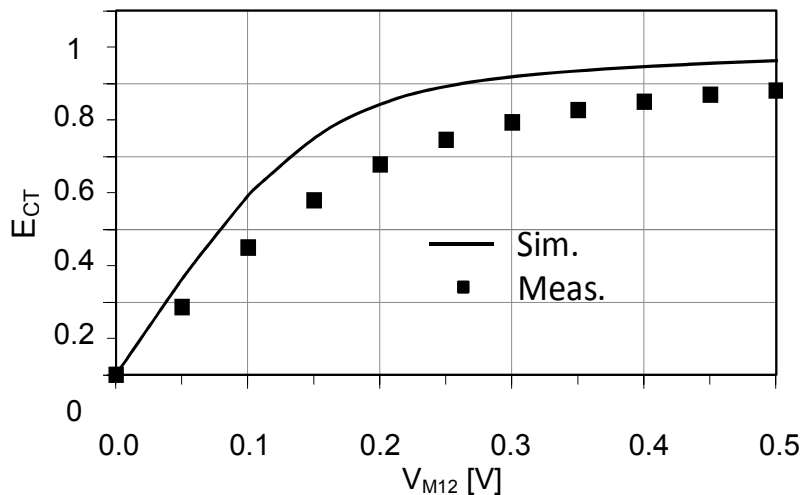
For the DC characteristics of the device, the experimental set up is configured as shown in Fig.5.5 (a). Static Characterization of the CAPD structures has been carried out, using a 650-nm laser to illuminate the device. The voltage applied to the modulating electrode M1 has been swept from -0.5V to 0.5V. Another modulating electrode V_{M2} has been maintained at 0V and the collecting electrodes C1 and C2 are biased at 1V. Fig. 5.7 (a) shows the typical results of two collecting currents I_{C1} , I_{C2} and their sum I_{TOT} plotted with respect to the voltage between M1 and M2 (V_{M12}) for a minimum size CAPD. Here the positive part of the modulating voltage V_{M12} values are reported in the graph, I_{C1} and I_{C2} being

symmetrical with respect to the point where they intersect the y-axis while I_{TOT} being symmetrical with respect to the y-axis. In Fig. 5.7 (a) the solid lines represent the simulation results for DC performance of the device. In the simulations, the light intensity has then been adjusted to fit I_{C1} and I_{C2} measured at $V_{M12}=0$ V. The overall agreement between measurements and simulations is satisfactory and acceptable; indicating that the charge transfer mechanism operates in actual devices closely to theoretical predictions. As can be noted, I_{TOT} slightly increases at increasing V_{M12} . This can be explained to photocurrents that are collected by the n-well junctions at the four corners of the pixel when $V_{M12}=0$ V, while they are progressively transferred to C1 for increasing V_{M12} due to the increasing modulation electric field. Starting from I_{C1} and I_{C2} curves like those shown in Fig.5.7 (a), the charge transfer efficiency (E_{CT}), i.e., the CAPD capability of redirecting photogenerated charge towards one of the two collecting junctions under static conditions, can be quantified as [75]

$$E_{CT} = \frac{I_{C1} - I_{C2}}{I_{C1} + I_{C2}} \quad (5.9)$$



(a)



(b)

Fig.5.7: Simulated (solid line) and experimental (dotted line) DC characterizations of CAPD 10×10 array (a) DC current at the collecting electrodes I_{C1} and I_{C2} and total current I_{TOT} and (b) Corresponding Charge transfer efficiency.

Experimental and simulated values of E_{CT} are plotted in Fig. 5.7(b) for the same CAPD considered for Fig. 5.7(a). As can be noted, an E_{CT} of 80% is achieved for $V_{M12}=0.5$ V. The corresponding power consumption is 10 μ W (deriving from a modulation current of 20 μ A through the 25-k Ω resistance existing between M1 and M2).

The peak value (E_{CT}^{\max}) reached by E_{CT} during the V_{M12} cycle limits the maximum demodulation contrast achievable with the CAPD. Introducing (5.6) into (5.9) actually yields

$$E_{CT} = 2f_{C1} - 1 = 2f_{C1}^{AC} \sin 2\pi ft \quad (5.10)$$

from, which it follows that

$$E_{CT}^{\max} = 2f_{C1}^{AC} . \quad (5.11)$$

By using (5.11), the demodulation contrast (5.8) can be rewritten as

$$C_d = \frac{E_{CT}^{\max}}{2} \cdot \frac{I_{TOT}^{AC}}{I_{TOT}^{DC}} . \quad (5.12)$$

and is seen to approach the theoretical limit 0.5 of the sine wave modulation when the charge transfer E_{CT}^{\max} approaches unity (besides for low frequency and 100% laser modulation depth).

The dynamic demodulation contrast of the device is another feature to judge the performance of the charge separation in the device. The sensor ability to separate and transfer the charges to the corresponding output node can be expressed as a demodulation contrast. It should be as high as possible in order to large signal amplitude and hence a good signal-to-noise ratio for the phase detection. In optics the demodulation contrast is defined as follows:

$$\text{Demodulation Contrast } C_d (\%) = \frac{I_{\max} - I_{\min}}{I_{\max} + I_{\min}} \times 100\%$$

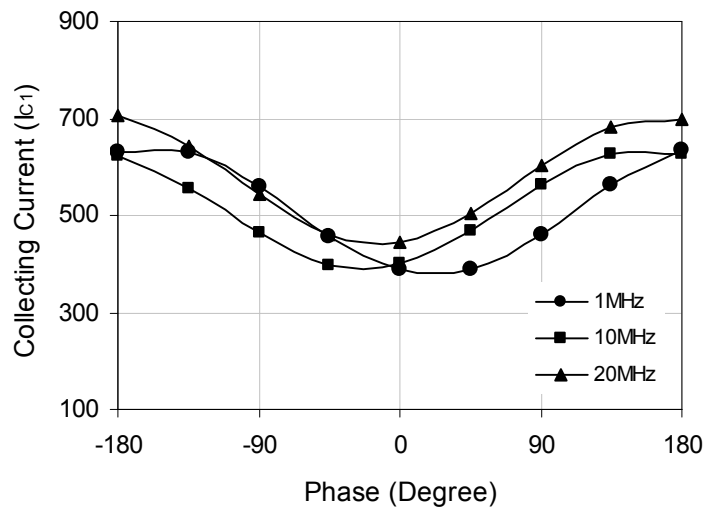
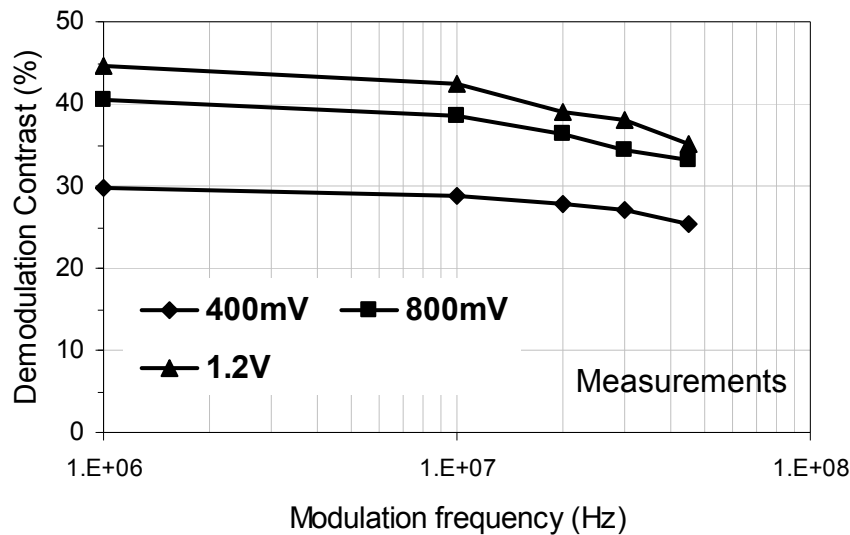


Fig.5.8: Average Current measured at collecting electrode at different modulation frequencies.

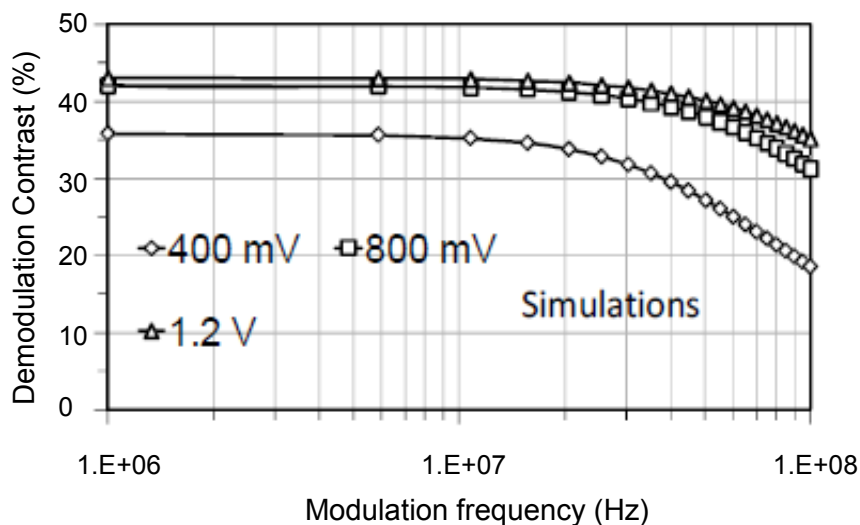
The dynamic demodulation contrast and the average current measurement at the detection electrodes are characterized for this device by using the setup shown in Fig.5.5 (b). One of the two signals of a signal

generator is used to modulate a laser emitter. Another one is passed through a differential amplifier generating two 180°-shifted voltages that are sent to the modulation electrodes M1 and M2 of the CAPD under test. A constant potential 1V is biased the collecting electrodes C1 and C2. A differential sine wave modulation signal with 400mV amplitude is applied to the modulating electrode of the device array.

The average current is measured under a 650nm red laser with a flat frequency response from the band of interest and near about 90% modulation depth used to illuminate the test device. The phase delay $\Delta\phi$ of the laser modulating signal with respect to the CAPD modulation voltages can be varied arbitrarily. Since, under operating conditions, the illuminator is modulated with a signal in phase with the CAPD modulation voltage, $\Delta\phi$ plays the same role as ϕ used in (5.6)-(5.7). The average currents flowing out of the CAPD detection electrodes is directly readout by using a semiconductor parameter analyzer (HP4145), automatically providing the required low-pass filtering. The average current of the device array at different laser phase is shown in Fig.5.8. The obtained curve is turned out from the convolution of optical and electrical modulated signals and depends on the cosine of the phase difference $\Delta\phi$ between the two signals [54]. In agreement with (5.7), the measured I_{Cl} vs. $\Delta\phi$ curves shown in Fig.5.8 contain a constant plus a term proportional to $\cos(\Delta\phi)$.



(a)



(b)

Fig.5.9: Demodulation Contrast (a) Experimental and (b) simulated demodulation contrast as a function of modulation frequency. The laser wavelength is 650 nm.

Experimental and theoretical values for C_d are plotted in Figs. 5.9(a) and (b) as a function of the modulation frequency for different modulation voltage amplitudes. Experimental C_d values are obtained from measurements like those shown in Fig.5.8. Theoretical C_d values can be calculated by plugging simulated E_{CT}^{\max} , I_{TOT}^{DC} and I_{TOT}^{AC} values into (5.12). E_{CT}^{\max} and I_{TOT}^{DC} are obtained but DC simulations, whereas I_{TOT}^{AC} is derived from small-signal AC simulations driven by a monochromatic optical stimulus at the adopted laser wavelength. As can be inferred from Fig.5.9(a), the -3dB bandwidth of the demodulation contrast is, for all the modulation voltage amplitudes considered, larger than the highest modulation frequency adopted experimentally (45MHz).

Raising the modulation voltage amplitude boosts C_d over the entire frequency range, as a result of the increased E_{CT}^{\max} . However, the obtained incremental enhancement reduces progressively as the theoretical limit of 0.5 is approached. Results shown in Fig.5.9(a), if compared with previous works on CAPD demodulators [67,68] demonstrate that shrinking the pixel dimensions both reduces the power consumption of a single pixel and enhances the bandwidth of the device, thus enabling the implementation of moderate sized arrays with a standard process without substrate doping modifications. The proposed solution can be competitive with existing photo-gate-based mixer technologies [54, 60, 72, 73] because it offers a larger demodulation contrast and a bandwidth comparable with the best devices presented so far.

5.3.2 Influence of wavelength on the device:

Light absorption length in silicon is strongly dependent on the wavelength. At 650 nm wavelength, photons are absorbed within a few μm from the surface. The charge carriers that are optically generated in these regions can be collected easily by the detection electrodes, thus increasing the demodulation contrast of the device, defined as the sensor ability to separate and transfer the charges to the corresponding output node.

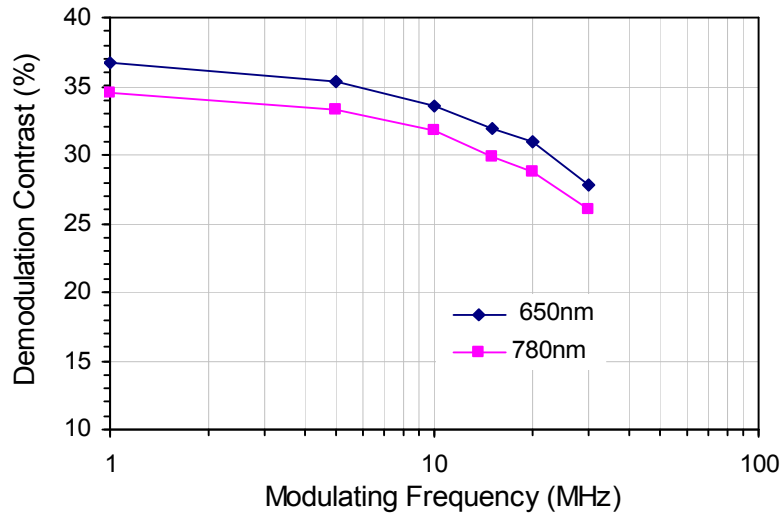


Fig.5.10: Demodulation Contrast as a function of the modulation frequency at two different wavelengths.

On the other hand, higher wavelength photons can penetrate deeper in the device. The photoelectrons generated far from the surface need more time to reach the demodulating electrical field. This causes long diffusion times and blurred diffusion directions, thus degrading the device crosstalk and leading to a lower demodulation contrast. The long diffusion times lower the demodulation cut-off frequency, while the blurring effect also appears at low modulation frequencies. These effects are confirmed by experimental results of Fig.5.10, which shows the demodulation contrast as a function of the modulation frequency in the range from 1MHz to 30 MHz at two wavelengths 650nm and 780nm.

5.3.3 Influence of modulation frequency on the device:

We know that the photon absorption length in silicon at 650 nm is few micrometers, the decrease in the demodulation contrast with frequency can be evaluated with respect to time that photoelectrons generated deeper in the epitaxial layer of the device. The higher the demodulation frequency, the shorter is the time available for the single charge carriers to travel from their site of optical generation to the storage area. If they do not reach the right storage site in time, they will contribute to a wrong sampling point and lower the demodulation contrast. Fig.5.10 shows the demodulation contrast at different frequencies and wavelengths. Demodulation contrast is decreased with the increasing of modulation frequency.

5.3.4 Demodulation Contrast vs. Modulation voltage of the device:

We know that the demodulation contrast is an important feature to quantify the perfection of charge separation in the device. The sensor ability to separate and transfer the charges to the corresponding output node can be expressed as a demodulation contrast. It should be as high as possible in order to large signal amplitude and hence a good signal-to-noise ratio for the phase detection.

It is obvious that the demodulation contrast depends on the amplitudes of the modulation voltages. By using a driver circuit we can control the signal amplitude of the modulation signal. By the exact adjustment of the modulation voltage of the device at a fixed frequency we can get the optimal demodulation contrast of the device. Fig.5.11 shows the evolution of demodulation contrast for the device as a function of the modulation voltage amplitude. Here we considered the different demodulation frequencies. Increasing the modulation voltage basically increases the majority current that cause the drift of the minority carriers, namely electrons. As the modulation voltage is applied to the modulating electrodes, the photo generated electrons arrive at the detector node of the device. When applying the still larger voltages the electrical field extends deeper in the substrate so that more electrons reach detection node resulting in a higher demodulation contrast. However, it should be stressed that at the same time this increases the power consumption in the device, so the value of the modulation voltage amplitude should be carefully chosen.

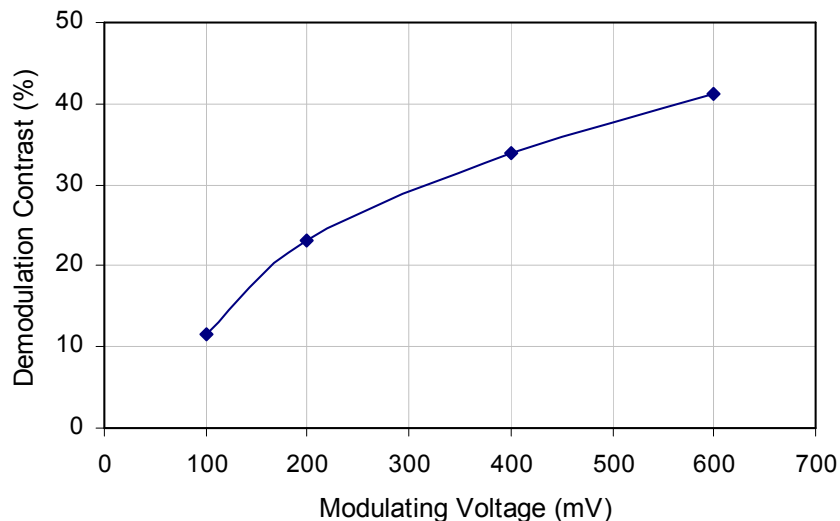


Fig.5.11: Demodulation Contrast as a function of the modulation voltage for CAPD device.

5.3.5 Spectral responsivity and Quantum Efficiency:

We know that responsivity measures the effectiveness of the detector for converting electromagnetic radiation to electrical current or voltage. The responsivity is the ratio of the rms value of a current signal generated by the detector to the incident radiant power at the entrance to the detector.

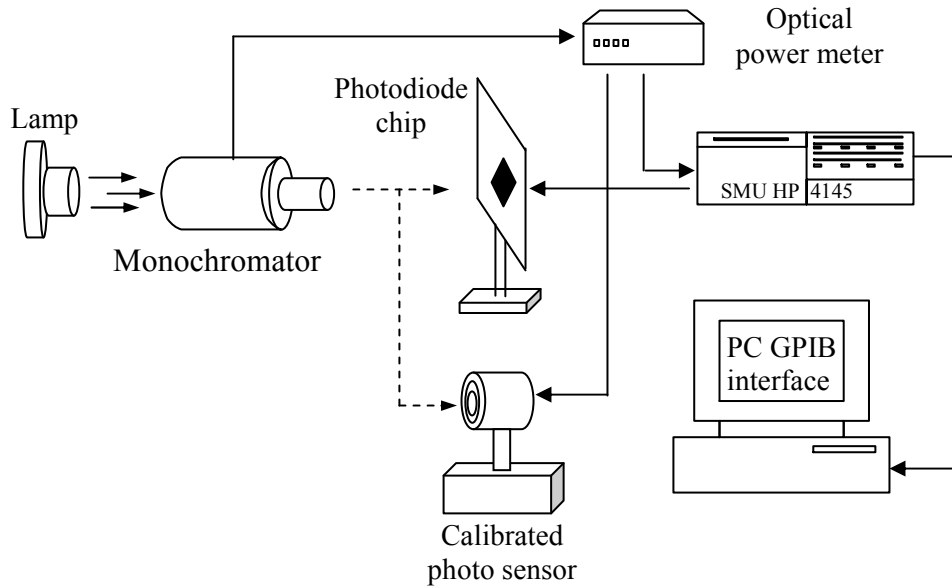


Fig.5.12: Test setup for spectral response characterization

The quantum efficiency of a photonic device indicates the efficiency of light with a given wavelength conversion into electrical signal. It represents the probability of a single photon to generate electron-hole pair, characterizing the photo converting part of the device. The experimental setup is shown in Fig.5.12. The mono-chromator with a light source provides monochromatic light with variable wavelengths. The optical output is connected to an optical fiber with one end shining on a calibrated photo-sensor and the other end on the photodiode under test. The mono-chromator, the optical power meter and a pico-ammeter SMU HP 4145 are connected to a PC through a GBIP interfaces for data acquisition and storage. All the measurements for the photodiodes are conducted in a shield box to isolate optical and electrical noise.

Since the reflection and absorption characteristics of the photo-detector sensitive material change with wavelength, so that responsivity depends on wavelengths. Fig.5.13 shows the responsivity vs. wavelengths of our test device.

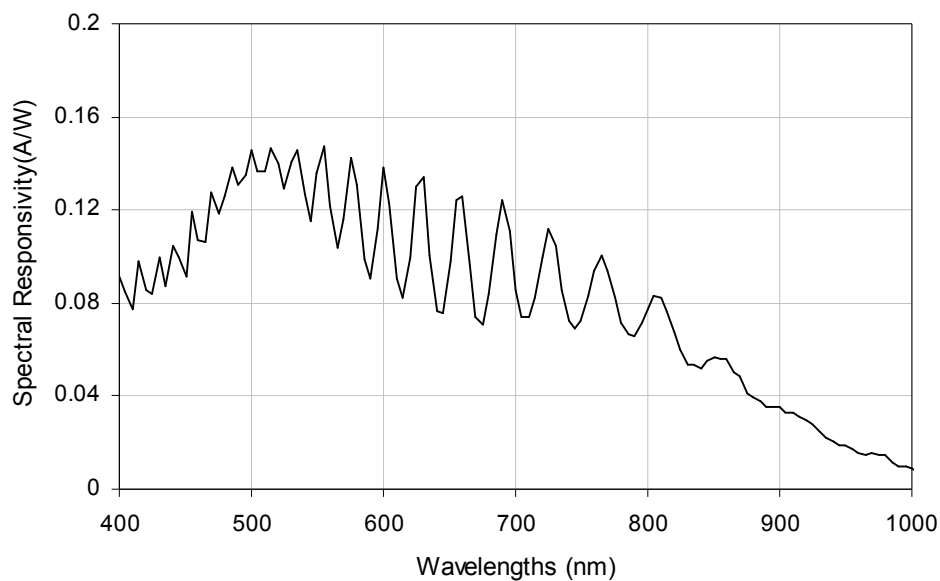


Fig.5.13: Responsivity vs. wavelengths for CAPD

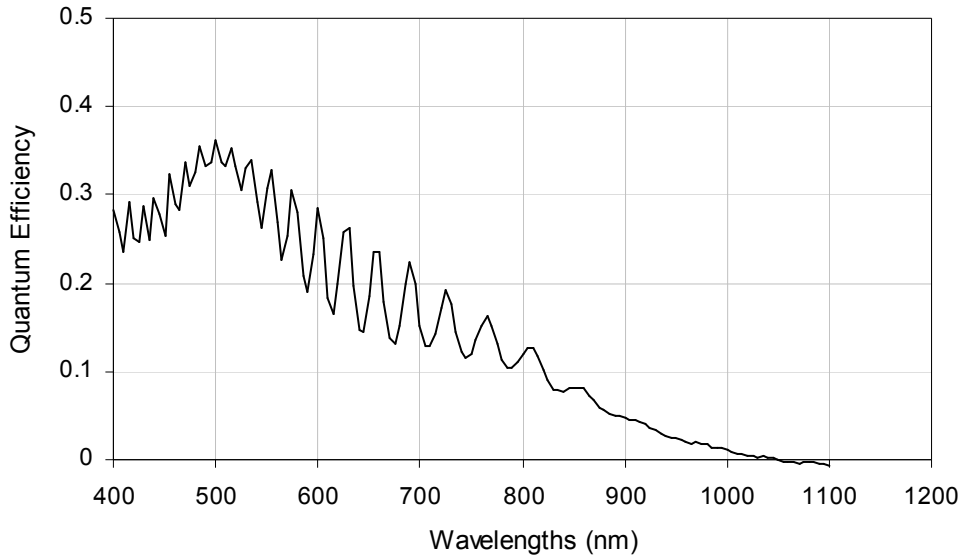


Fig.5.14: Quantum efficiency vs. wavelengths for CAPD

Fig.5.14 shows the quantum efficiency of CAPD in different wavelengths. CAPD devices have potentially higher quantum efficiencies with respect to photo-gate demodulators because their active area is not covered by polysilicon gates. Our devices show a peak quantum efficiency of 35% at 500 nm and >20% up to 600 nm.

5.3.6 Capacitance measurement:

Junction capacitance of the image sensors charge sensing node determines the charge capacity and the charge-to-voltage conversion gain. A smaller capacitance at the charge sensing node is preferred due to higher signal-to-noise ratio of the output signal. On the other hand, small capacitance has lower charge capacity and thus a lower dynamic range.

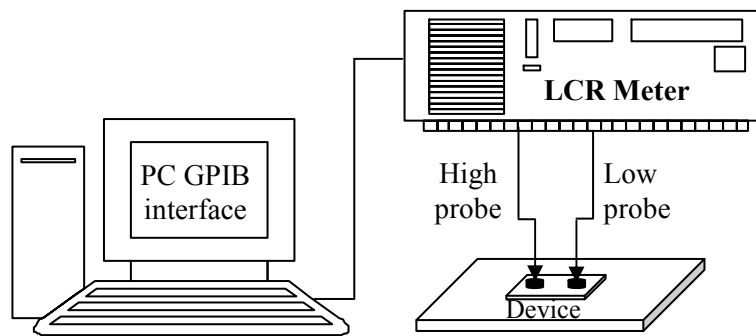


Fig.5.15: Experimental set-up for capacitance measurement

The experimental set-up for capacitance measurement of the CAPD is shown in Fig.5.15. A LCR Meter is used for accurate measurement of capacitance. The LCR meter is a general purpose meter used to measure inductor (L), capacitor(C) and resistor (R).

The LCR meter has a built-in power supply and is capable of supplying the bias voltage required for the device. In this experiment the LCR meter serves two main functions. They are to measure the capacitance of the device and to supply the required voltage bias across the junction. The LCR meter and the experiment are controlled by using a LABVIEW program via GPIB interface between the Computer and the LCR meter.

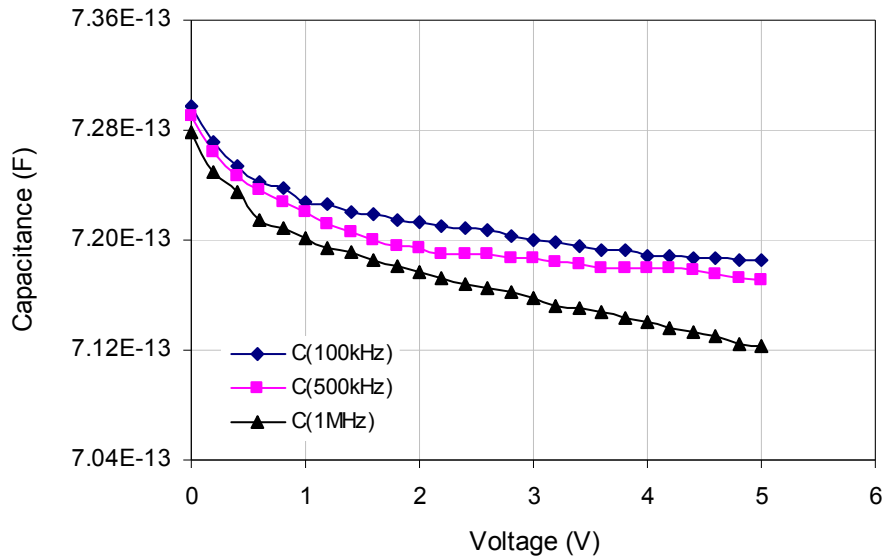
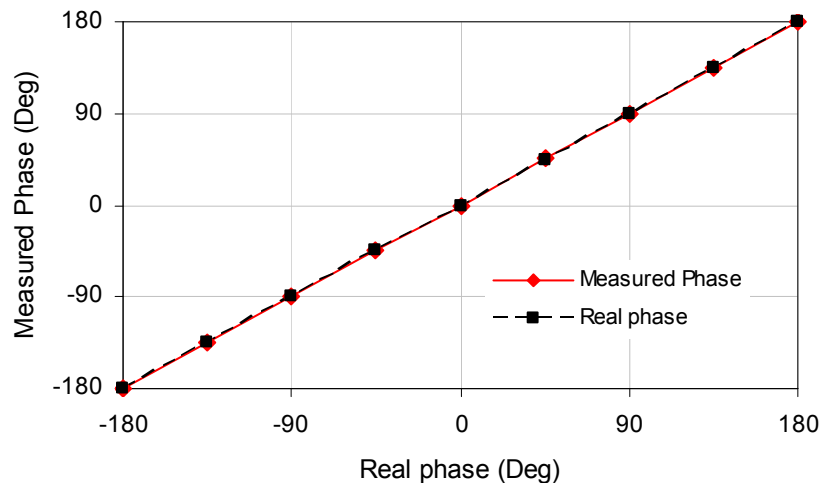


Fig.5.16: C-V response at different frequencies

Fig.5.16 shows C-V response under different frequencies of the device. It shows that a higher reverse bias produces a lower capacitance due to a larger depletion width. For higher reverse bias, more electrons are attracted to the n-side, holes attracted to the p-side. This result increases the depletion region. In this figure it shows that, at lower frequency the capacitance is larger than at higher frequency. Due to the deep-level impurities in the space charge region make the capacitance to be frequency dependent because of their finite charging and discharging time [74, 75].

5.3.7 Phase linearity measurement of the device:

In Time-of Flight technique the phase delay of the modulated light signal is measured by the sensor receiver. The signal back reflected by the scene is modulated in light intensity and phase, the phase modulation being caused by the depth of 3D scene. It is possible to recover the signal by synchronously demodulating the incoming modulated light within the sensor by correlating it with the modulation signal that is implemented on the modulation electrodes of the sensor. For the phase delay measurement we consider both sinusoidal wave and square wave at 20 MHz frequency as the modulation signal for both modulation electrodes, with 180° phase shift between them. Another wave is used to modulate a laser emitter with appropriate synchronization between other two modulation signals. By using the same measurement set-up shown in Fig.5.6 (b) we can measure the phase delay of the device.



(a)

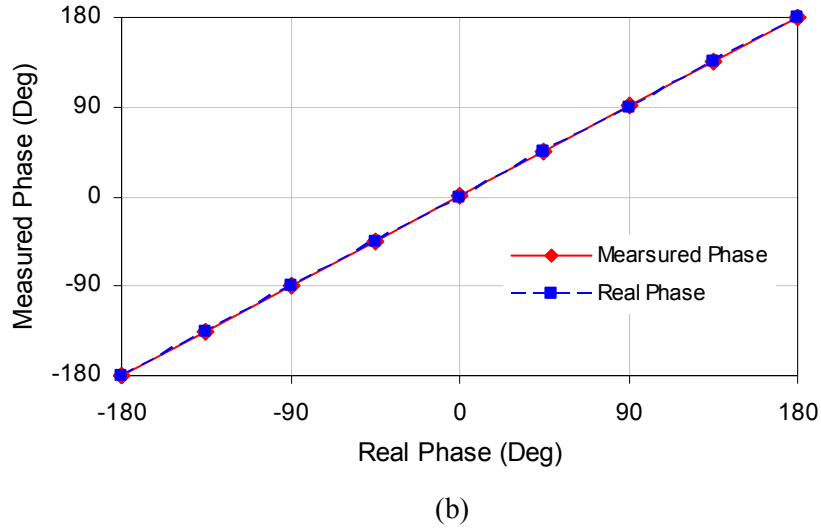


Fig.5.17: Measured and Real phase delay for (a) Sinusoidal wave (b) Square wave.

The modulation wave is sampled in four spaced sampling points of the signal time period. In this measurement the considered four sampling points are -180° , -90° , 0° and $+90^\circ$. At each point of the phase delay of the input laser modulated signal we measured the amplitude from the collecting electrodes at four sampling points C_1 (-180°), C_2 (-90°), C_3 (-0°) and C_4 ($+90^\circ$) of the modulation signal [76]. Now we can directly measure the phase by using equation (5.13):

$$\varphi = \arctan \frac{C_1(-180^\circ) - C_3(-0^\circ)}{C_2(-90^\circ) - C_4(+90^\circ)} \quad (5.13)$$

In this way we can measure the phase delay of the incoming modulated light signal within the detector with respect to the applied phase delay. Fig. 5.17(a) and 5.17(b) show the measured phase and the real phase of the modulated laser signal for both sinusoidal wave and square wave. The resulting phase and linearity error are reported in Fig 5.18.

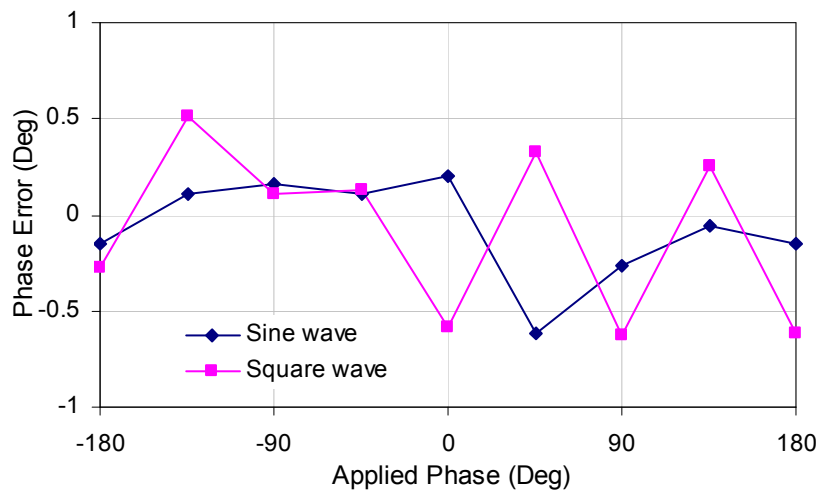


Fig.5.18: Phase linearity error vs. Applied phase in the case of sine-wave modulation and square-wave modulation

The maximum linearity errors for sinusoidal and square waves are 0.11% and 0.16% respectively, thus confirming the good linearity of the proposed system. The very good linearity obtained also in the case of

square-wave modulation indicates that the contribution of high frequency harmonic components contained in the square wave modulation signals has a small influence on the phase determination. The measurement method employed thus reveals a good robustness against optical and electrical modulating signal distortions, which would be inevitably present in a real measuring system.

5.3.8 Noise measurement:

We know that shot noise is present in all photon detectors due to the random arrival rate of photons from the source of illumination under measurement and background radiation. This shot noise is often called "photon noise". Photon noise limits the detector performance even if all internal noise sources were eliminated. Shot noise also arises from the dark current in the absence of light. A low-frequency noise measurement arrangement is shown in the Fig.5.19. It consists of a low-noise biasing circuit, a device under test (DUT), a current amplifier, a spectrum analyser and a personal computer.

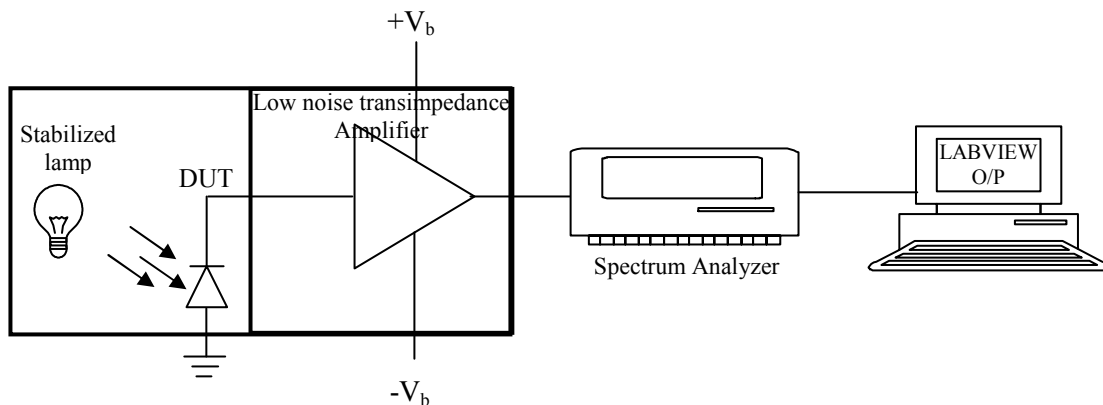


Fig.5.19: Experimental set-up for shot noise measurement

It is taken to make sure that the system noise is not influenced by the noise other than that from the DUT. For this purpose, batteries are employed to provide power to the measurement set-up. A shield metal box is used to protect the set-up from 50 Hz power line noise and from the surrounding electromagnetic interference. The connection between the DUT, low noise transimpedance amplifier and the dynamic signal analyser was made by using double shielded low-noise BNC cables. The connecting cable between the DUT and the current amplifier was made as short as possible in order to reduce the undesirable noise to a minimum.

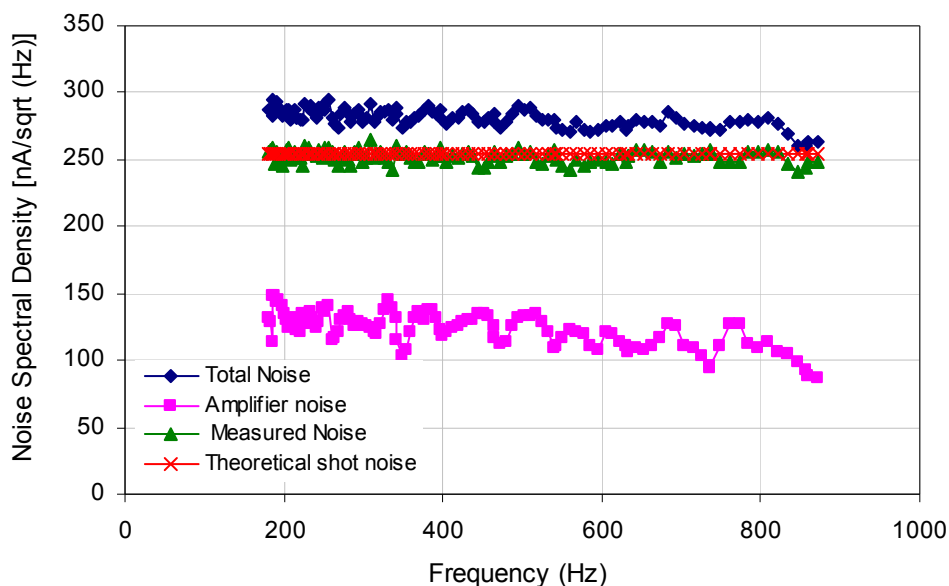


Fig.5.20: Noise Spectrum Density vs. Frequency

In this experiment the shot noise is measured in the frequency range of 200 Hz to 1000 Hz. The theoretical shot noise can be measured by using the equation $I_S = (2qI_pB)^{1/2}$ where q is the electron charge, I_p is photo current and B is the bandwidth. By using the above experimental set up we can measure the total noise in the presence of light at different frequencies. In this case the photon shot noise and the amplifier noises are included. At the same time we can measure amplifier noise in the absence of light illumination. By calculating the total noise and the amplifier noise it is possible to measure the experimental shot noise. The measured shot noise at several frequencies is not significantly varied from the theoretical noise.

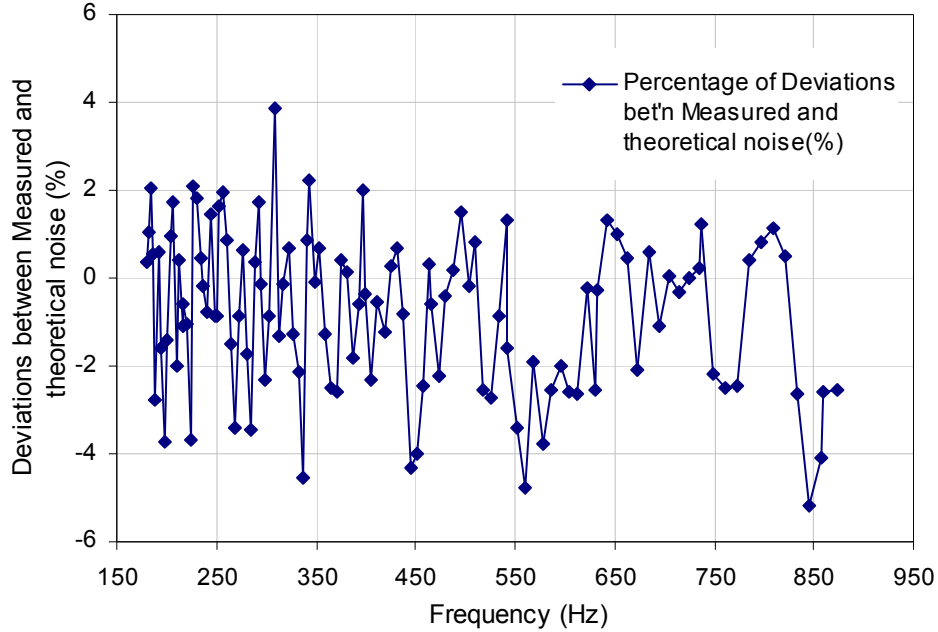


Fig.5.21: Percentage of noise deviation vs. Frequency

Fig.5.20 shows the experimental results of total noise, amplifier noise, theoretical noise and measured noise of our device. Fig.5.21 shows the percentage of deviation between measured noise and theoretical noise. The maximum deviation between them is 5.19%.

5.4 Device geometry and power consumptions:

Device simulations have finally pointed out that, by optimizing the geometry of the modulation junctions, the trade-off between demodulation contrast and power consumption can actually be relaxed. This is illustrated by Fig.5.22, showing simulated power-consumption vs. E_{CT} curves for minimum-size CAPDs differing only for the modulation junction geometry. More specifically, the structure with “short” modulation junctions is the one adopted for all previously-shown results and depicted in Fig.5.2. This structure is compared with a CAPD having longer modulation junctions (structure labeled as “long” in Fig.5.22) and with a CAPD featuring “U-shaped” modulation junctions (structure labelled as “U-shaped” in Fig.5.22). As can be noted, with the “long” modulation electrodes it is possible to obtain the same E_{CT} characterizing the standard structure at reduced power consumption or equivalently, an enhanced E_{CT} at the same power consumption. A further improvement can be achieved by using the “U-shaped” electrodes. These improvements are due to the larger volume interested by the modulation electric field, leading to a more effective charge redistribution between the two collecting nodes in response to the modulation-voltage changes and therefore to a smaller modulation voltage needed to achieve a given E_{CT} . This in turn results in reduced power consumption, the decrease in required modulation voltage being only partially compensated by the increase in the modulation hole current. CAPD with optimized modulation-junction geometries will be implemented in near future.

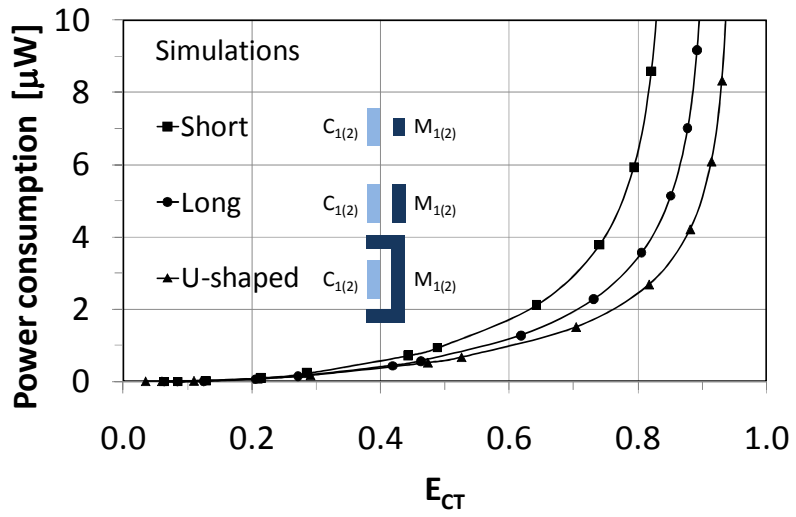


Fig.5.22: Simulated power vs. charge-transfer-efficiency (E_{CT}) curves for different modulation-electrode geometries. Simulated devices are minimum-size CAPD's ($10 \times 10 \mu\text{m}^2$ pixel).

with the help of its sensing node. The charge is converted to the voltage by the capacitance of the photodiode at the sensing node. Design of the photodemodulator in the schematic shown in Fig.6.1 is modelled by Verilog simulation. In this implementation of the pixel we adopted PMOS transistors for the reset and global shutter switches so that the whole voltage range can be measured and analyzed. Source follower transistor acts as a buffer amplifier to segregate the charge of the sensing node. The data is read out when the row select transistor is enabled.

6.2 Simulation of Photodemodulator APS:

The active pixel sensor operation is divided into three stages: reset stage, integration stage and the read out stage. The image acquisition sequence starts by resetting to V_{dd} the floating diffusions C1 and C2 turning on both the reset and the global shutter transistors for all the pixels. Integration stage follows the reset stage.

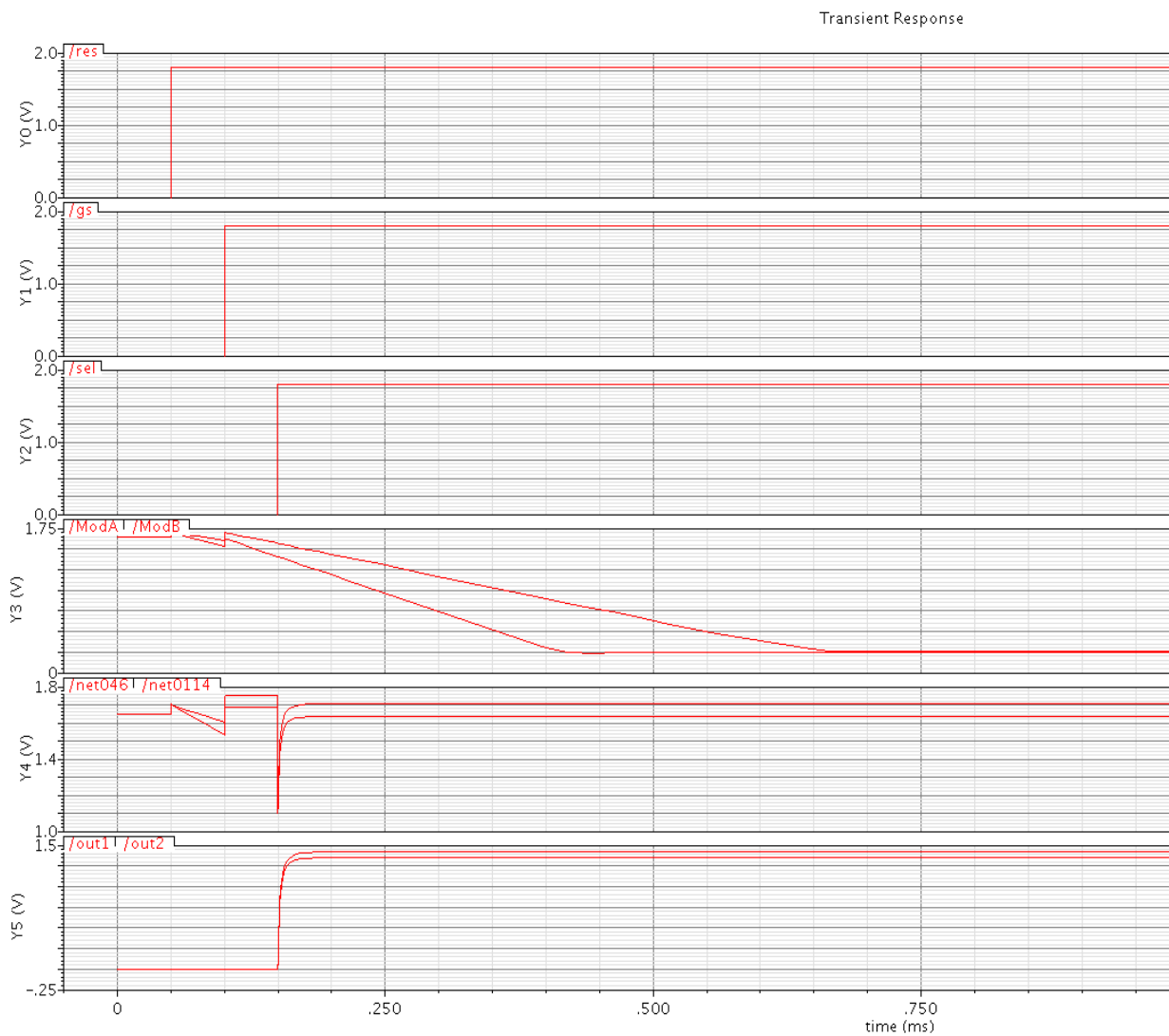


Fig.6.2: Simulation result of Photodemodulator APS

When the reset transistor is switched off, the two modulation electrodes M1 and M2 are modulated and the light emitter is turned on, so that the photo-generated charge is mixed towards the two collection nodes C1 and C2 and the DC component of the photocurrent is integrated onto the floating diffusion capacitance. After a suitable exposure time T_{exp} , The global shutter transistors are then switched off in all the pixels, sampling the demodulated signals onto the floating diffusions while anti-blooming diodes

avoid blooming effects. In the above simulation results Fig: 6.2 indicates transient simulation of the pixel circuit. In this graph, *res*, *gs* and *sel* represent the voltages at the gate of T_{RS} , T_{GS} and T_{RWS} transistors respectively. *ModA* and *ModB* indicate photodemodulator output at the collecting electrodes C1 and C2. Finally *out1* and *out2* represent the pixel output at *Bitline1* and *Bitline2* respectively.

6.3 Layout design of an Active Pixel Sensor and its specifications:

For the operation of this active pixel sensor, the pixel array needs 1.8V power supply. We know that the described photo-demodulator device is integrated with 10 transistors, active pixel structure. The half of the pixel electronics is devoted to reading one of the two collecting junctions, based on a standard source follower voltage buffer and pixel select, a reset transistor, a global shutter and an anti-blooming diode-connected transistor.

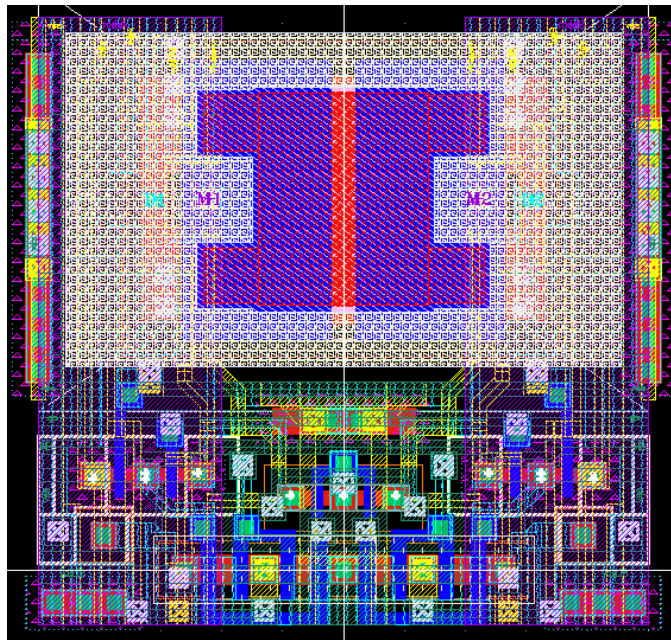


Fig.6.3: Pixel circuit layouts

Fig.6.3 illustrates the compact $10 \times 10 \mu\text{m}$ -square pixel layout with a fill factor of 24% by using a $0.18 \mu\text{m}$ CMOS technology. The $6 \mu\text{m} \times 4 \mu\text{m}$ rectangular part is the sensing area of the pixel layout. The photodemodulator contains two collecting contacts and two modulation contacts. The modulation contacts have been realized using p-well diffusions to obtain a deep electric field, while the collection diodes are made with n+ diffusions. Two metal lines are used both to mask the floating diffusions from direct light and to distribute the modulation signals. The two vertical parts of this layout are sized and spaced equally in vertical dimensions to get symmetrical pixel arrays. Table-IV shows the summarized characteristics of the pixel.

Table-IV: Pixel Summaries

Technology	:	0.18 μ m CMOS technology
Pixel area	:	10 \times 10 μ m ²
Transistors per pixel	:	10
Fill Factor	:	24%
Photodetector type	:	Current Assisted Photo Demodulator (CAPD).
Pixel Supply voltage	:	1.8V

6.4 Photodemodulator Verilog simulations:

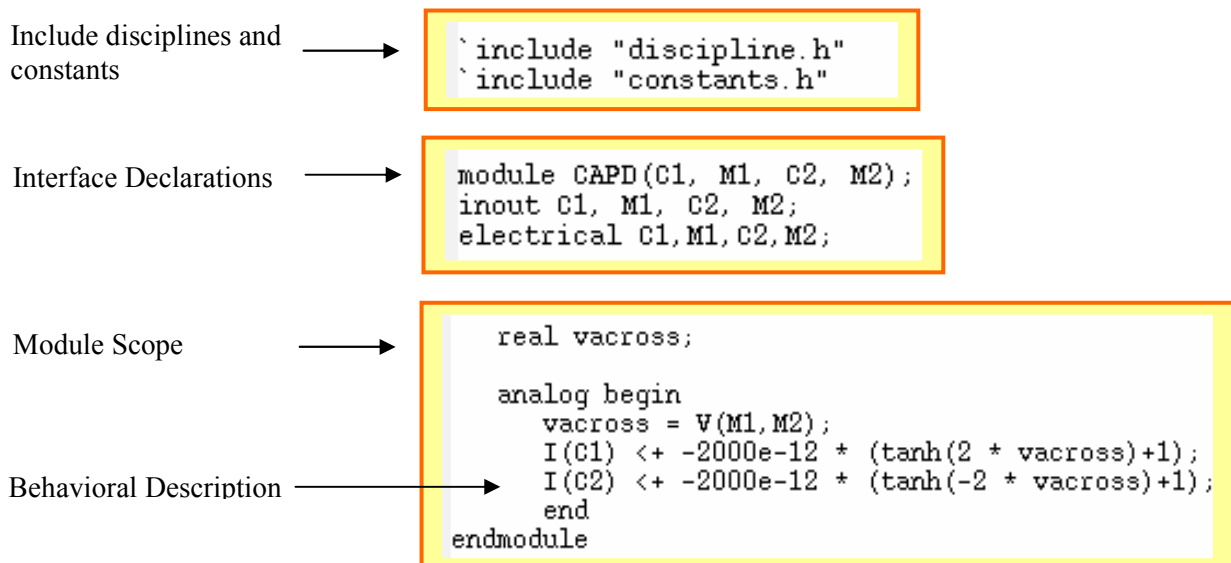
We know that Verilog-AMS is an event-based Hardware Description Language (HDL) for analog and mixed signal systems and integrated circuits to create and use modules that encapsulate high-level behavioural descriptions as well as structural descriptions of systems and components [77]. In this pixel circuit simulation we will use Verilog to simulate our device designs at behavioural level. In other words, we can check the correction of our device functionally by using Verilog simulation. In this section we will talk about the current assisted photonic demodulator behaviours and simulate this device with pixel circuit by using HSPICE circuit simulation tools.

Verilog-A is well-suited for describing nonlinear behaviours. According to the CAPD operation principle and DC characteristics of the collecting current, the I-V characteristics equation of the device can be written as:

$$I(C1) = [-2000e-12 * (\tanh(2 * vacross) + 1)]$$

$$I(C2) = [-2000e-12 * (\tanh(-2 * vacross) + 1)]$$

The CAPD device in the example for DC characteristics code given below is introduced. This provides a simple example of the anatomy of a Verilog electrical model of the CAPD device.



Line 1 & 2 instructs the compiler to insert the contents of the file *disciplines and constants* into the text. This file contains the definitions that make the Verilog specific for electrical modeling.

Interface declaration part declares the module block, within which the model behaviour is defined. The model is named *CAPD* and has four ports, named "C1 and C2" and "M1 and M2". Ports provide connections to other parts of the circuit.

Behavioral description of the device is described in the module scope. The keyword *analog* declares the analog block. In this case, it is a single statement. However, statements can be grouped together using *begin/end* keywords to denote blocks which, in turn, can be named to allow local declarations. The simple, single statement includes several key aspects of the language. On the right hand side, the access function *vacross* returns the voltage difference between M1 and M2. The "<+" in this line is called the *contribution operator* and in this example contributes the value of the evaluated right hand side expression as the voltage from p to n.

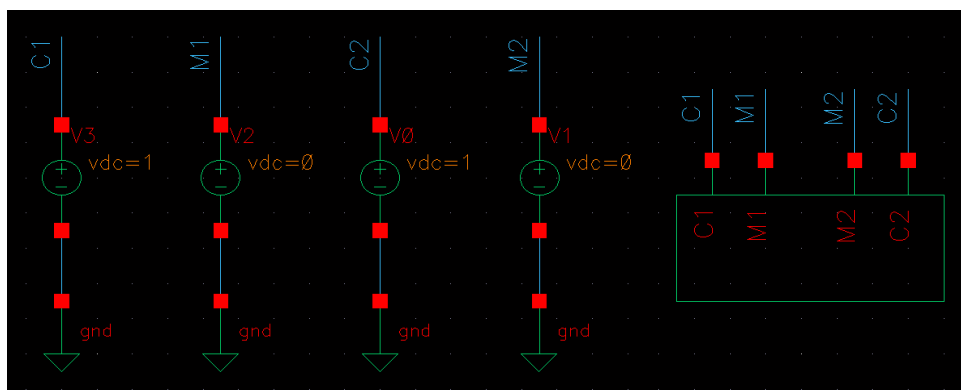


Fig.6.4: Schematic of Verilog-CAPD devices.

Fig.6.4 shows the DC characteristics schematic and the symbol of the CAPD device. Here C1 and C2 indicate the collecting electrodes and M1 and M2 indicate the modulation Electrodes.

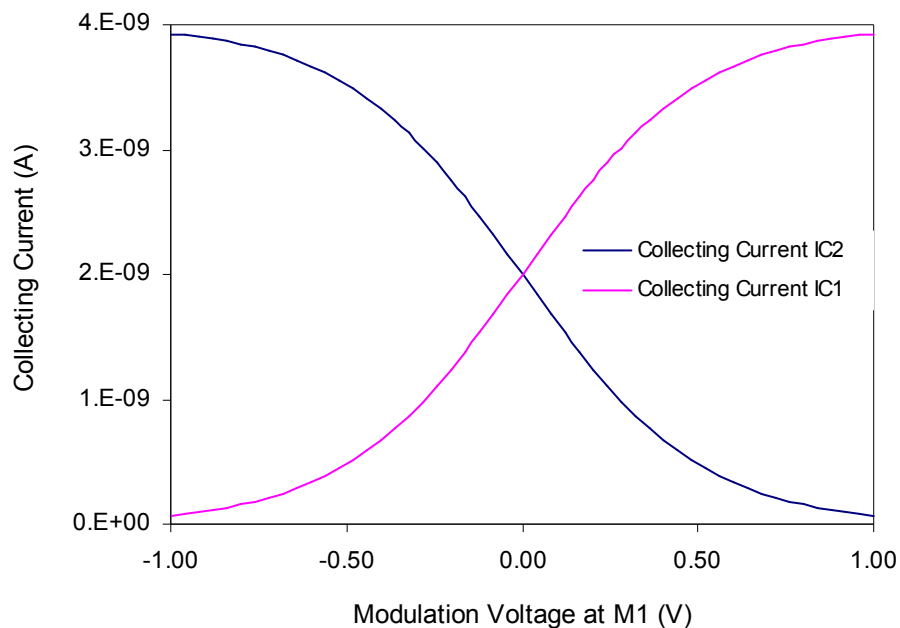
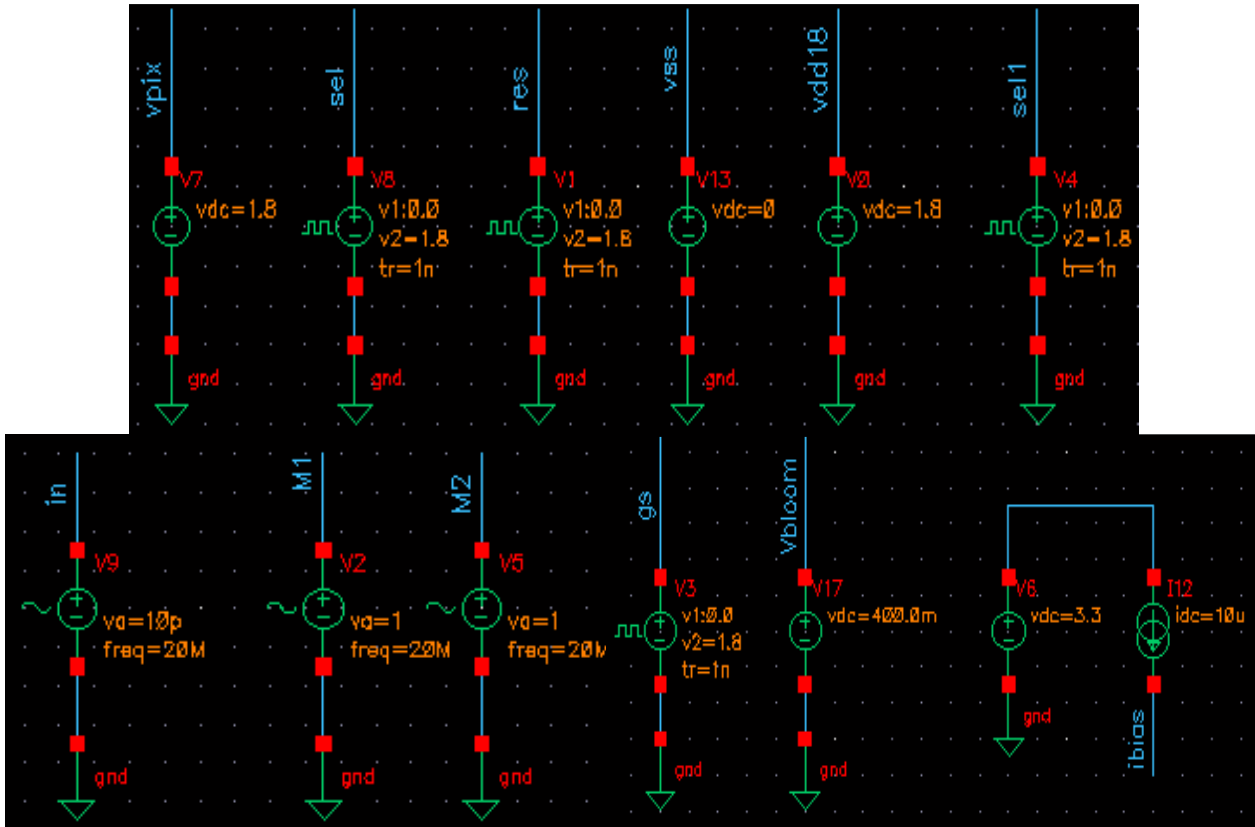
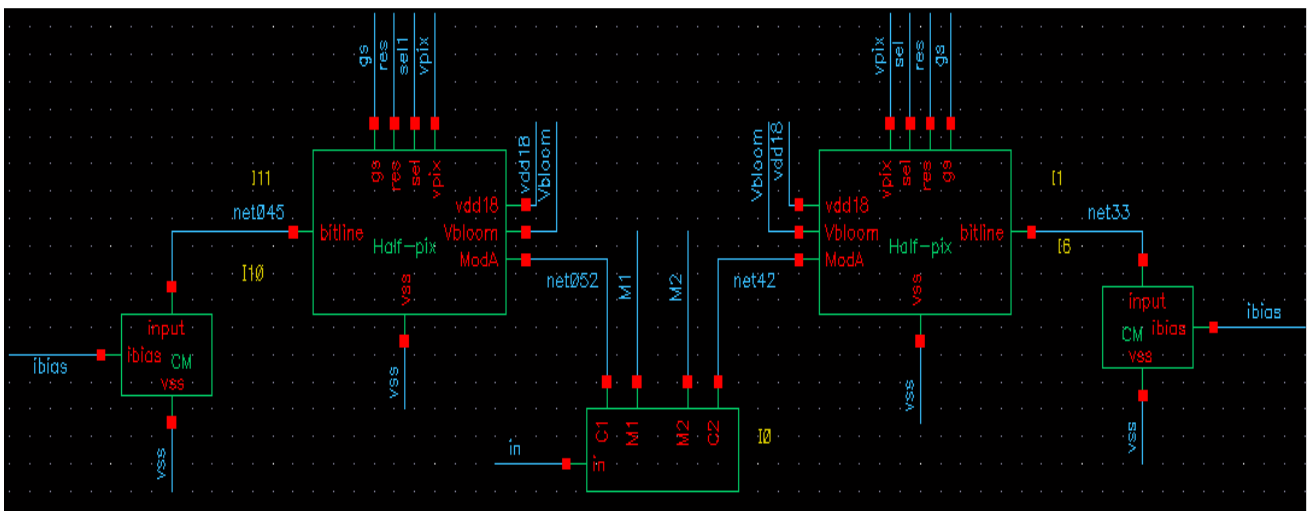


Fig.6.5: I-V curve of Verilog CAPD device model

According to the DC characteristics of the CAPD device, similar consideration is taken. The modulation electrode M1 is swept from -0.5V to 0.5V and another modulation electrode M2 remains 0V. At the same time the collecting electrodes C1 and C2 is biased by 1V. By using the above code we can find out the similar DC output characteristics curve that has already shown in Fig.5.8 (a), which is obtained from device simulation software by ISE-TCAD and device experiment. Fig.6.5 indicates the DC mixing properties of the CAPD device.



(a)



(b)

Fig.6.6: (a) & (b) Pixel circuit configuration using Verilog-device model.

Fig.6.6 (a) & (b) shows the HSPICE simulation of pixel circuit using Verilog model device. Here, in the Fig.6.6 (a) represents different types of applying voltage to the pixel circuit. Fig.6.5 (b) shows the block diagram of the pixel circuit. The CAPD device consists of four electrodes as we explained before, another electrode *in* represents the equivalent voltage source of the illuminated light source. The half pixel block indicates the five transistors pixel circuit that we have already described at the beginning of this chapter. The CM is the current mirror that is used as a load. For this simulation the device model code is written below:

Include disciplines and constants

```
`include "discipline.h"
`include "constants.h"
```

Interface Declarations

```
module CAPD(C1, M1, C2, M2, in);
inout C1, M1, C2, M2, in;
electrical C1, M1, C2, M2, in;
```

Module Scope

Behavioral Description

```
real vacross;

analog begin
    vacross = V(M1, M2);
    I(C1) <+ -V(in) * (tanh(2 * vacross)+ 1);
    I(C2) <+ -V(in) * (tanh(-2 * vacross)+ 1);
end
endmodule
```

For this simulation we consider two 20 MHz sinusoidal voltages with 180° phase shift for modulation electrodes M1 and M2, a constant potential 1V is biased the collecting electrodes C1 and C2. Another 20MHz sinusoidal modulating signal is applied to the electrode of the CAPD device *in* which can act as a reflected laser modulated signal.

Applying all required voltages for the reset signal, global shutter, *Vpix*, anti-blooming, row select signal and consider the *in* signal with an arbitrary phase delay $\Delta\phi$. From the transient simulation, at arbitrary phase delay $\Delta\phi$ of the *in* signal we get different photodiode output. Finally, the data is read out by enabling the row select transistor. Fig.6.7 shows the transient simulation of the Verilog CAPD device based pixel at different phase of the signal in which is equivalent to the laser modulating signal. In this figure graph 1, 2 and 3 represent reset signal, global shutter and row select signal respectively. Graph 4 indicates the photodetector output and graph 6 indicates the bit line output of the pixel circuit.

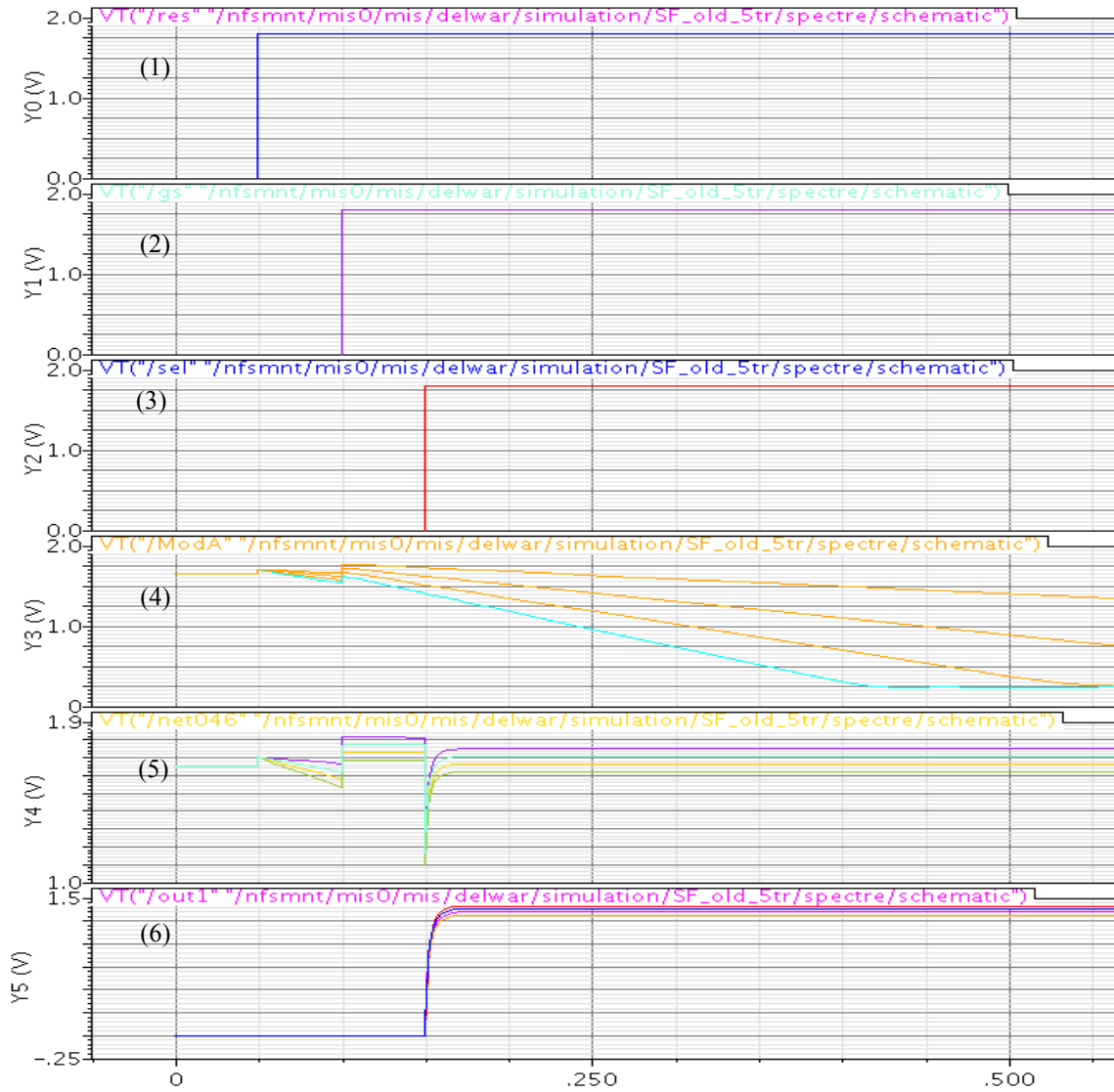


Fig.6.7: Transient simulation of the pixel circuit using Verilog device model

6.5 Architecture of a 120 × 160 pixels Image Sensor:

The core of the sensor is formed by a 120×160 pixel array. The image sensor architecture is shown in Fig.6.8. The two bit lines in each column are connected to a column pseudo-differential amplifier performing a first filtering of the output signal to reduce pixel Fixed Pattern Noise (FPN). Column FPN is removed by an output amplifier performing Differential Double Sampling. Because of the large modulation current flowing in the whole array, a modulation signal distribution tree has been implemented to equalize the parasitic resistive paths of the metal lines. Column amplifiers and output stage are based on 3.3V transistors in order to maximize the signal swing.

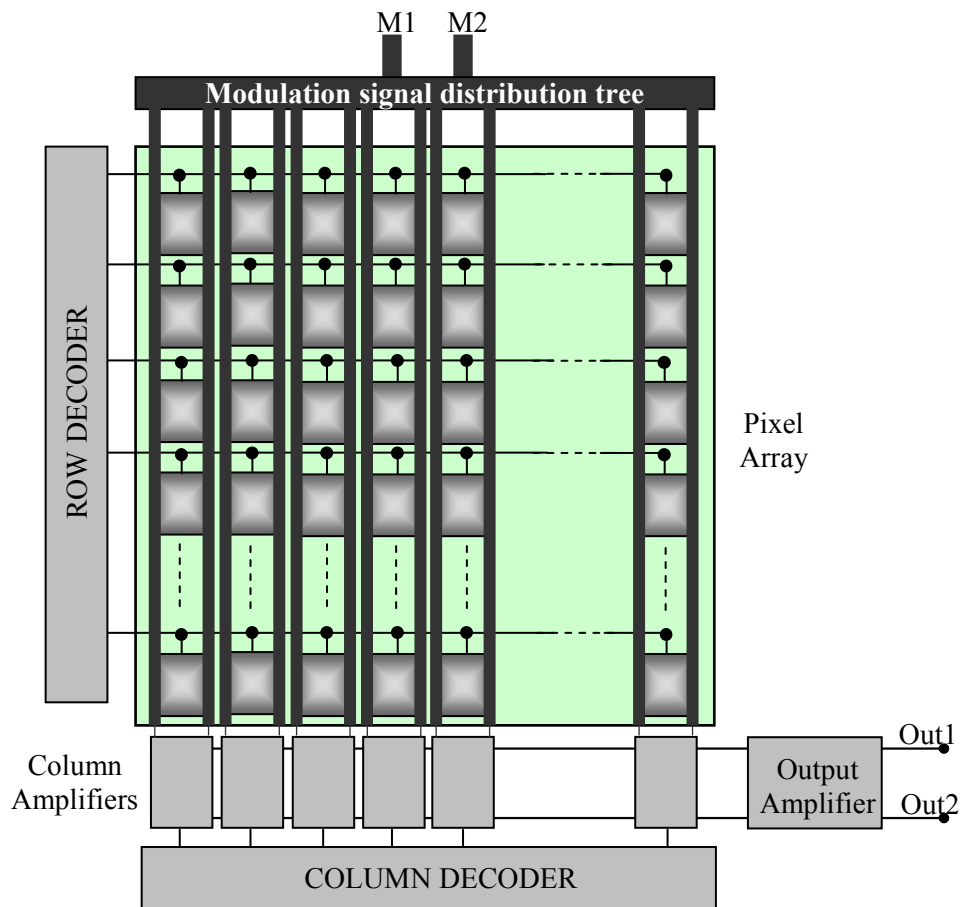


Fig.6.8: Imaging Chip Architecture

The sensor micrograph is shown in the Fig.6.9, where the main functional blocks have been highlighted: the pixel array, the column amplifiers, row and column decoder, the output filtering stage and the modulation signal distribution tree, everything integrated in a 2.5× 2.5 mm² area.

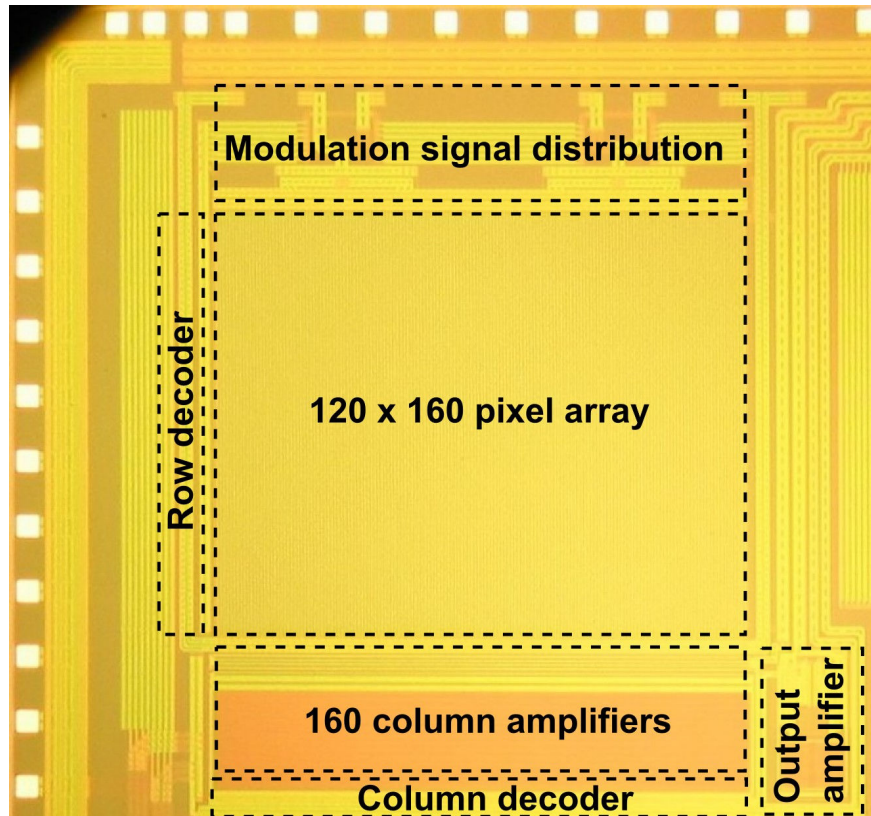


Fig.6.9: Sensor micro-photograph

6.5.1 Column Amplifier:

After collection of photodemodulator signal from a pixel array, it is read out by selecting each row and filtered by Column Filtering Stage (CFS). Fig.6.10 shows the column filtering stage of the sensor. After row select, the two stored voltage values are sampled at the bottom of each column, onto capacitors C_{CFS} .

Then θ_1 is switched off and two different operation modes can be selected. In case of 2D imaging, the pixel is reset, performing a standard double sampling read out aimed at reducing the FPN due to the in-pixel source follower mismatches.

When 3D imaging mode is enabled and taking advantage of the pseudo differential pixel structure, firstly sampled on capacitor C_{CFS} when θ_1 and θ_2 is high and θ_3 is low. The difference between the two pixel outputs is directly extracted by switching off θ_2 first and turning on θ_3 , thus doubling the swing of the resulting signal, reducing the noise contribution of subsequent stages.

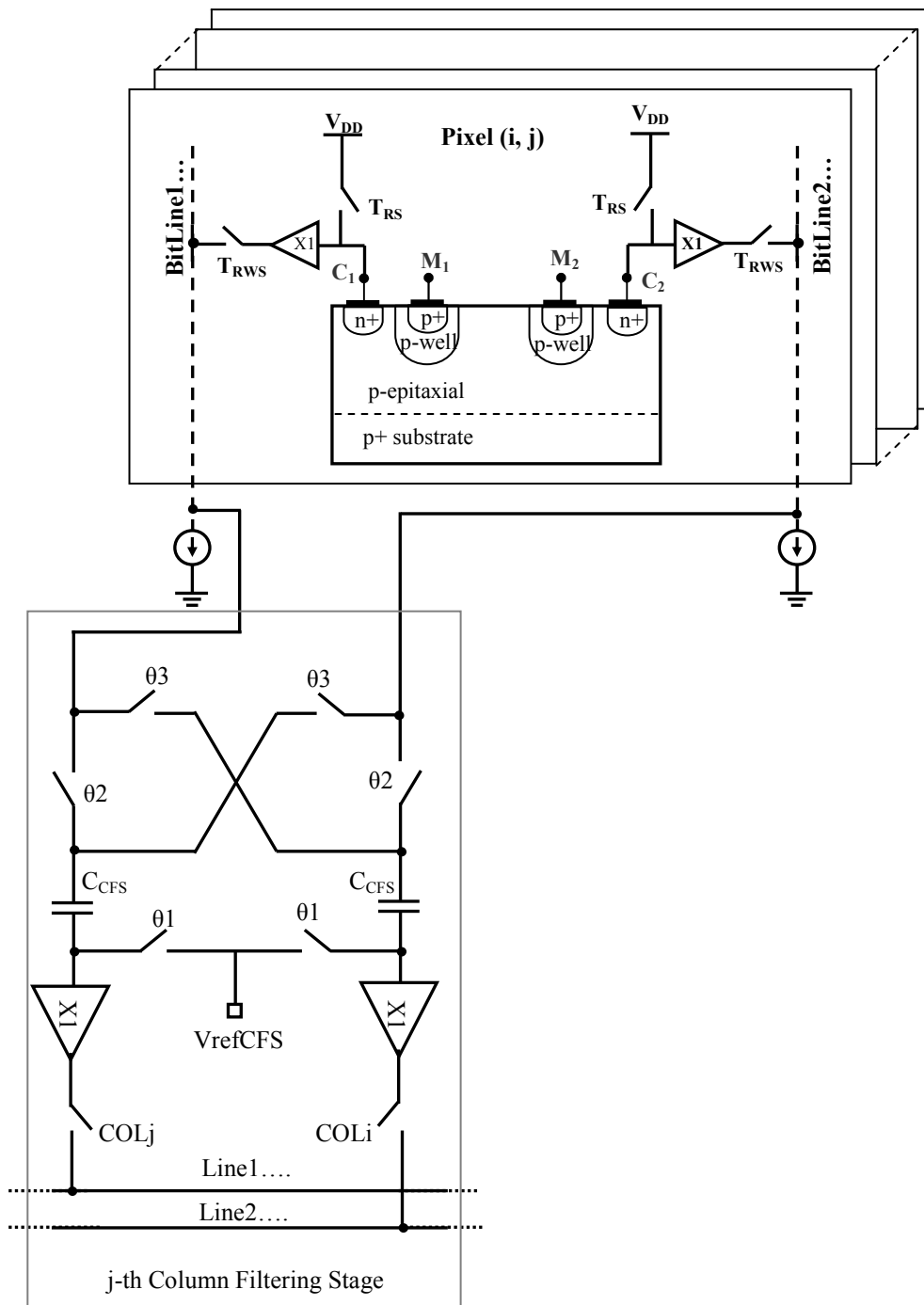


Fig.6.10: Column Amplifier

6.5.2 Double Delta Sampling (DDS):

A Double Delta Sampling (DDS) circuit has been implemented to filter Column Fixed Pattern noise. DDS is performed after the Column Filtering Stage (CFS) of the sensor. The reset voltage is subtracted from the integrated values in DDS circuits, eliminating the voltage offset variations due to the output of Column Filtering Stage. DDS is performed after the column filtering stage (CFS), shown in Fig.6.11. At the beginning of the measurement, the feedback capacitor C_{DDS} is reset at $\phi_4 = \text{High}$; by doing the Column Filtering Stage offset is sampled on C_{DDS} to allow its cancellation for the following phase. The input signal at the end of reset phase the CFS out put of this stage is sampled onto the capacitor C_G ; in this

phase ϕ_4 =High and $\overline{\phi_4}$ =low. After that the phase ϕ_4 is set low; C_S is discharged onto the capacitor C_{DDS} . Thus, the difference between the reset and signal value is obtained at the end of DDS output and reduce the column filtering stage FPN.

The use of DDS circuits for the entire imager further improves the precision and accuracy by eliminating Column Filtering Stage Fixed Pattern Noise.

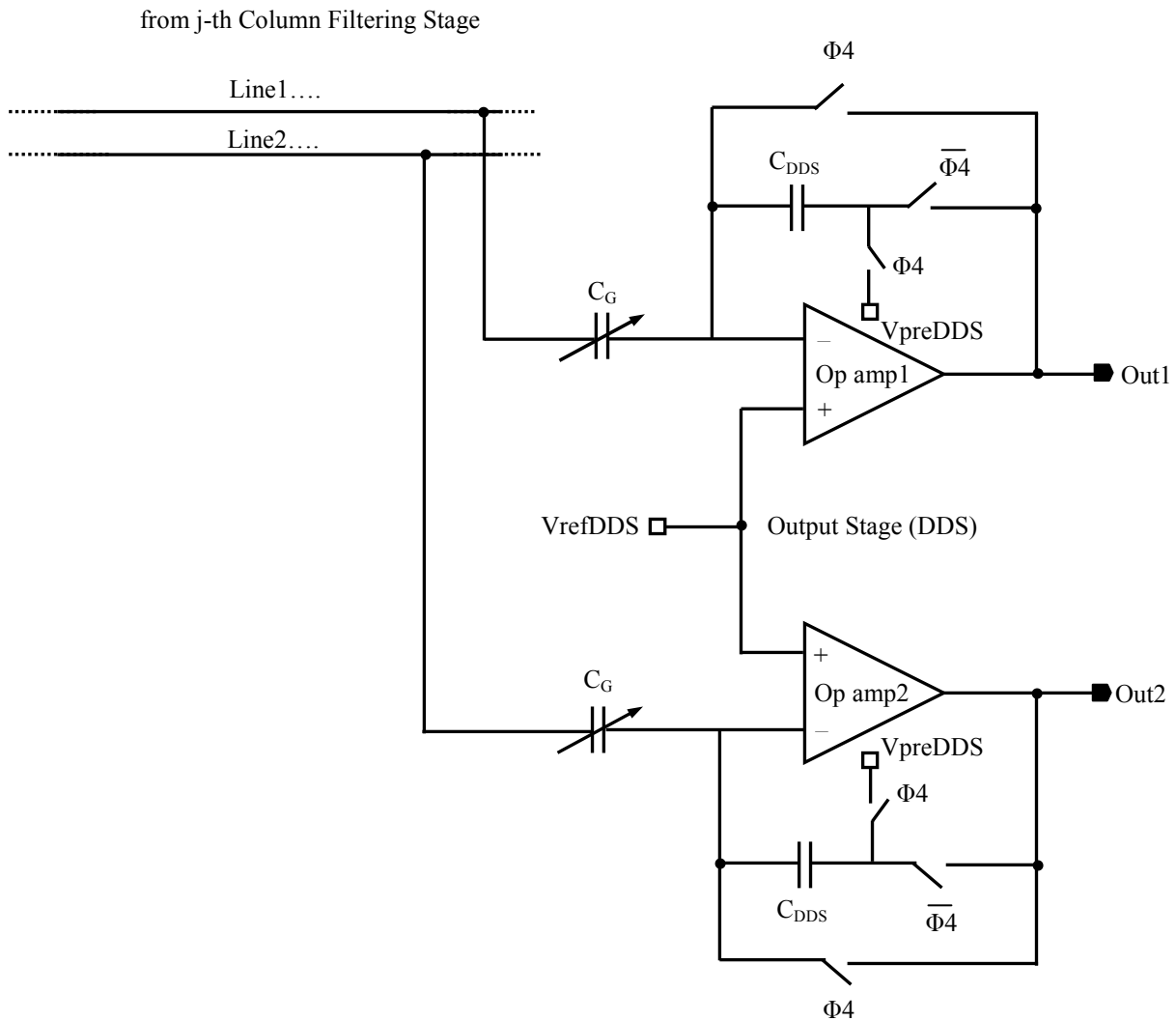


Fig.6.11: Double Delta Sampling (DDS)

6.5.3 Row and Column decoder:

We know that a decoder is a circuit component that decodes an input code. Given a binary code of n-bits, a decoder will tell which code is this out of the 2^n possible codes is shown in Fig.6.12. Each of the 2^n outputs corresponds to one of the possible 2^n input combinations. In a large capacity image sensor a separate clock signal is used to strobe in either the row or column addresses. In the present sensor, the row decoder and the column decoder are generally realizing by a shift register. The shift register is basically a cyclic one with load, clear and preset functions. In general operation, one D Flip-Flop (DFF) in row shift register and another one in column shift register are set to activate the row and column switches respectively. Hence a row is addressed and a pixel in the addressed row is selected. The other pixel cells in the addressed row are sequentially selected. Then follow through the pixels of the other rows.

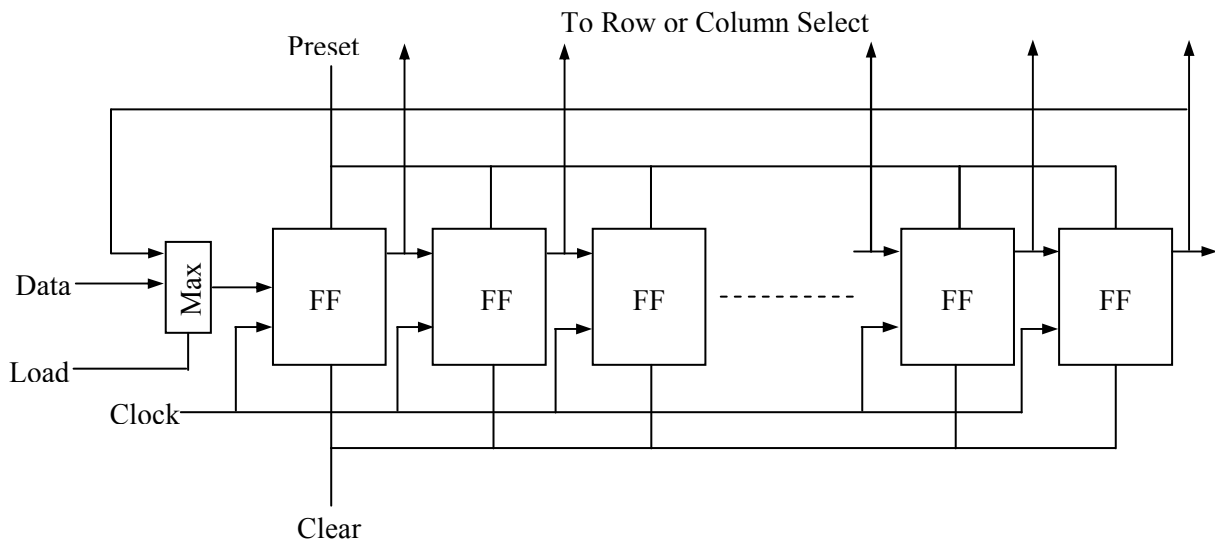


Fig.6.12: Row and Column Decoder

6.6 Characterizations of a 120 ×160 pixels Image Sensor:

In the previous sections, we have discussed the Current Assisted Photo mixing Demodulator (CAPD) based Active pixel sensor architecture and operation principle and presented a 120×160 pixel array image sensor based on previously described photodemodulator. In the following sections, we introduce the time of flight ranging system based on CAPD and fabricated in 0.18μm CMOS technology. After that we will demonstrate the respective function modules of the ranging system based on the CAPD device. Finally the results of correlation function measurement and some typical range measurements of the realized CAPD sensors will be presented.

6.6.1 System Description:

The testing setup used to measure the sensor performance is shown in Fig.6.13. The image sensor chip was mounted on a test board providing the power supplies and reference voltages and currents. The analog outputs were acquired through an acquisition board, while the timing signals were provided by a digital pattern generator. The pattern generator provided also the modulation signals to the chip and to an illumination module. A modulation driver was implemented on a separate circuit board to generate the high current needed by the modulation input electrodes. A camera objective (f=2.9mm, F/1) was mounted in front of the sensor chip, while a collimating diffuser was used to match the illumination field with the camera field of view.

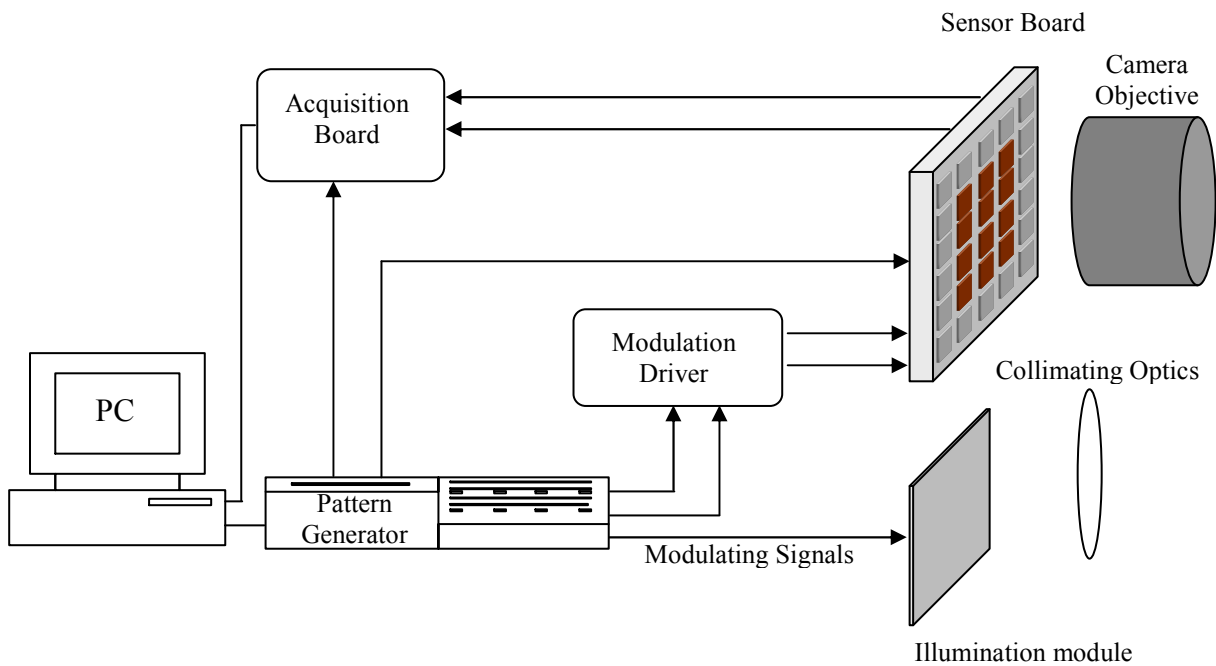


Fig.6.13: 3D measuring system block diagram.

6.6.1.1 Illumination module and Modulation driver:

The schematic diagram of the illumination module is shown in Fig.6.14 (a). It is composed of 3 high power LEDs L1 – L3 in series, driven by 3 signal MOSFETs M1-M3 in parallel. This topology has been determined by the need of modulating the current at high frequency while not exceeding the maximum power specification of the MOSFETs. Three small-valued resistors R_{M1} - R_{M3} have been added at each MOSFET source to reduce the effect of threshold voltage difference among them. The average current flowing into the LEDs is determined by the voltage at the divider formed by R1 and R2, while the modulation signal is injected by a pre-driver through a decoupling capacitor C.

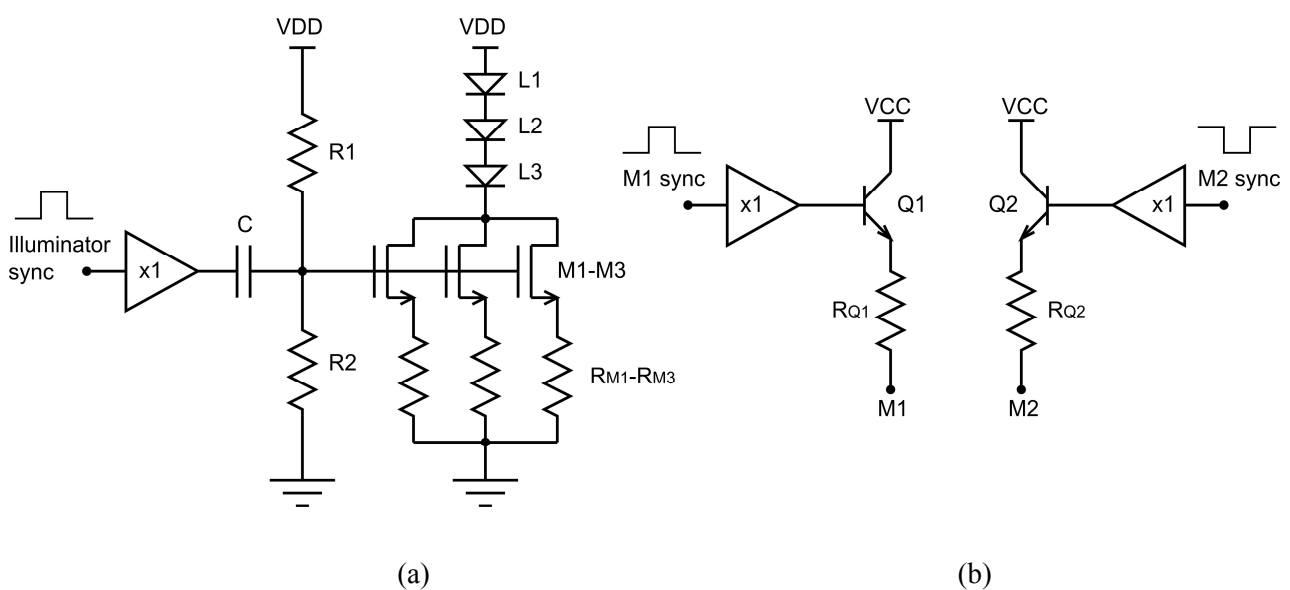


Fig.6.14: (a) Illumination module schematic diagram (b) Modulation driver schematic diagram.

The modulation current driver schematic is shown in Fig.6.6 (b). Two medium-power bipolar transistors Q1 and Q2 are used to provide the 400mA peak current typically sinked by the chip modulation inputs. Two unity-gain buffers provide the base current needed by the transistors, while the output currents are limited by two small-valued resistors R_{Q1} and R_{Q2} in series with the emitters. With this topology, an asymmetric modulation is provided, because this modulation driver has only current sourcing capabilities and all the current entering the modulation electrodes must be sinked by the chip ground connections. However, using this configuration, the power consumption of the drivers is reduced and the system is greatly simplified if compared to a push-pull stage with bipolar power supplies.

6.6.1.2 Light wavelength and power:

We know that the wavelength of light illustrates both the colour of the light and the visibility. For example, light with a wavelength of 650 nm is bright red. Light with a wavelength of 810 is invisible, infrared light. As most applications specify the use of invisible light, we use a longer wavelength of infrared light of 850nm. On the other hand light power is the same as brightness. A light source with more light power is brighter than a light source with less light power. The average optical power inside the field is 140mW and the LEDs are operated with an average current 400mA and a maximum current of 800mA. Fig.6.15 shows the photograph of our 3D sensor system with illumination module and the Table-V shows the summary of the system.



Fig.6.15: Micro Photograph of 3D imager With illumination module

Table-V: Illumination module Specifications

Illumination Module:	
Type	: LED, 20MHz
Wavelength	: 850nm
Power in the Field of View	: 140mW
Class (IEC 60825-1)	: 1M
Sensor:	
Objective	: 2.9mm,F/1
Sensor Field of View	: 23° × 30°
Modulation Current	: 400mA (Peak)

6.6.1.3 Field of View:

The field of view is the area which a camera can see. The area is shaped as a pyramid, on its side. Field of view is measured in degrees, either a single figure, which is a diagonal field of view, or two figures, the horizontal and vertical field of view. We have built our imager with field of a view of 23° × 30°.

6.6.1.4 Diffuser:

A diffuser is an optical component which converts light from one shape/pattern to another shape/pattern. A diffuser is typically made from glass or plastic. We use diffusers to take a beam of light from an LED and change that beam into an even pattern of light across a specific field of view. A relatively simple solution is to put a diffuser on top of the LED light source that is designed for the particular field of view. The diffuser provides an even light distribution over a predefined shape.

6.6.2 Correlation function measurement:

A first characterization of the sensor is conducted using a setup slightly different from the one shown in Fig.6.13. The chip is uniformly illuminated through a diffuser, while a red modulated laser ($\lambda=650\text{nm}$) is used as a light source. A commercial high frequency function generator is employed to modulate both the laser and the modulation electrode current. A 20MHz modulation frequency and both sine-wave and square-wave signals are used in the measurements.

Fig.6.16 (a) shows the correlation function measured as the output signal difference $\text{Out2} - \text{Out1}$ as a function of applied phase shift in the case of sine-wave modulation. In the measurement, the outputs are averaged over all the pixels of the array, thus reducing the temporal noise contribution to a negligible value with respect to the non-linearity. As can be observed, a good sine-wave fitting obtained, indicating a potentially low-distortion measurement.

In the final range-imaging system the correlation function is measured only for 4 different phase shifts and the phase shift is calculated using equation (5.13). To evaluate the linearity error obtained from this technique, the phase measurement has been repeated several times applying an increasing delay between modulation signal and optical signal. The measured delay averaged over the whole array is reported in Fig. 6.16(b) as a function of the applied delay. The maximum linearity error is 0.60%, corresponding to an error of 4.5cm in the distance measurement.

A sine wave correlation function is also observed applying square-wave modulation signal. Although theoretically the correlation signal between two square waves should be a triangular wave, the high order harmonics are filtered by the low-pass characteristics of the demodulator and in both cases a sine-wave correlation function is measured. Therefore, equation (5.13) was applied also in the case of square-wave modulation.

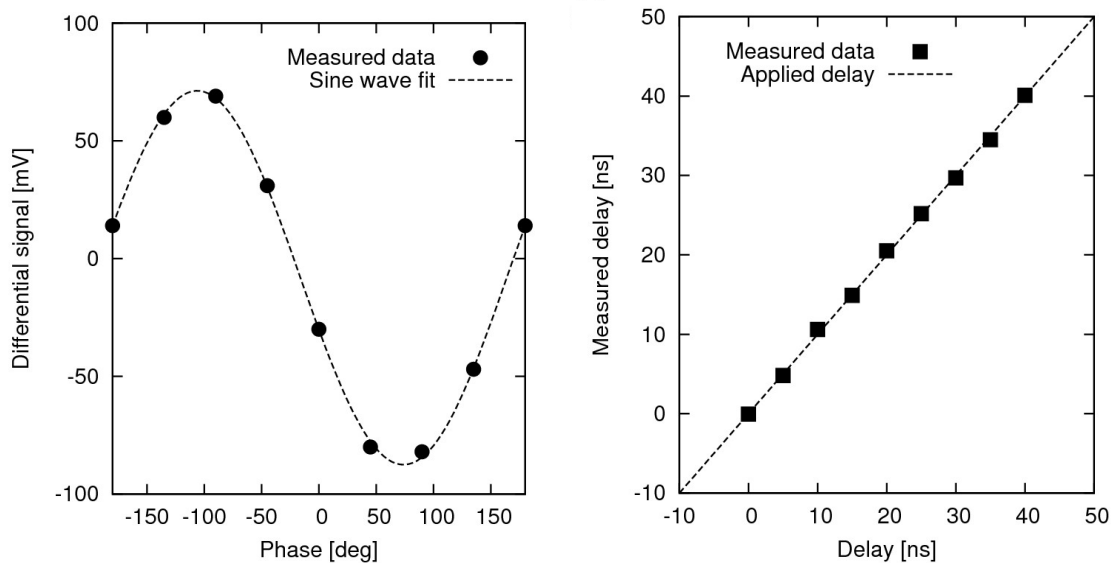


Fig.6.16: (a) Measured differential output as a function of applied phase. (b) Measured time delay as a function of applied time delay.

6.7 Distance measurement setup:

The 3D ranging performance of the system is finally evaluated using the setup shown in Fig. 6.17 using a 20 MHz-modulation frequency and square wave modulation signals. As described before, the sensor had a field of view of $23^\circ \times 30^\circ$ and the average optical power inside this field was 140mW. The image sensor mounts a 2.9mm objective, having an f number of 1. The maximum modulation current was 400mA, while the LEDs were operated with an average current of 400mA and a maximum current of 800mA. In this way we could achieve an 80% optical signal modulation depth. A 30ms integration time per frame was set, giving a range image frame rate of 7fps. A white diffusing target was placed at increasing distances in front of the sensor and a set of range images was acquired. A white board is placed at different distances from the sensor and is illuminated by the illumination module described before.

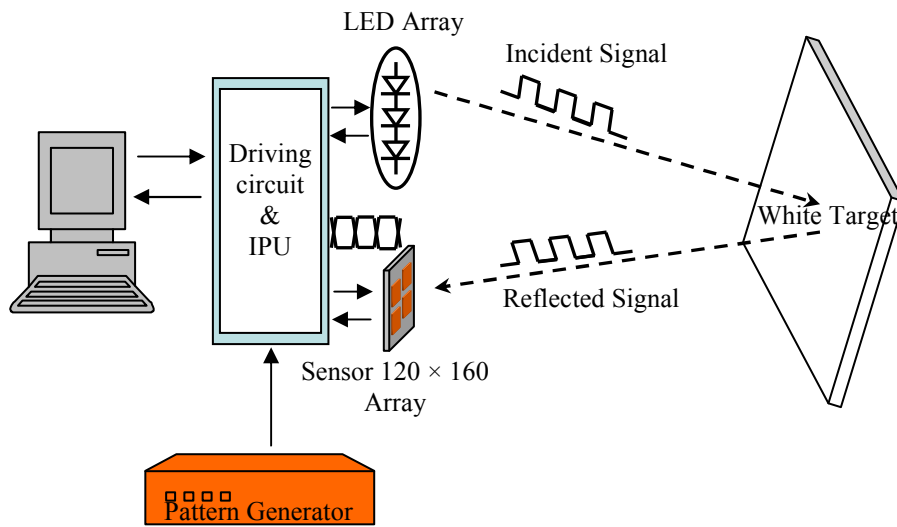
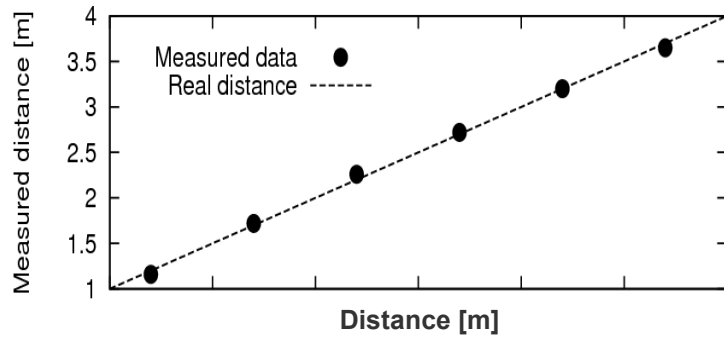


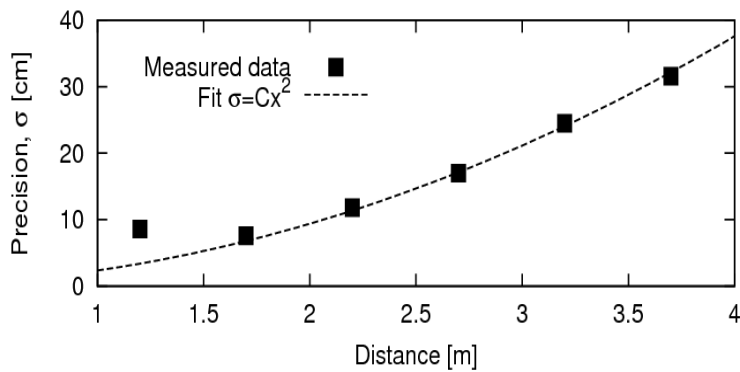
Fig.6.17: TOF based measurement Set-up

6.8 3D range measurement and sample pictures:

The measurement is done in the presence of ambient light. Fig.6.18 shows the actual distance of a white reflecting board from the sensor and the measured distance by the sensor. It shows the linear distance range from 1.2m to 3.7m. The maximum linearity error between the original and measured distance is 3.3%, while the distance non-uniformity among the pixels is lower than 2cm. Precision is the closeness of agreement between independent tests results obtained under specified conditions. The measure of precision is usually expressed in terms of imprecision and computed as a standard deviation of the test results. Less precision is reflected by a larger standard deviation. Precision is usually distinguished from accuracy, the variability of a measurement process around the true value. It is, in turn, can be decomposed further into short term variation or repeatability, and long term variation, or reproducibility. Beside the distance function also the relation between distance and standard deviation is of major importance because the accuracy of the measurements depends heavily on the amount of light received by the camera. In Fig.6.18 (b), apart from the first point in the series, where the sensor is close to saturation, the measurement precision increases with the square root of distance.



(a)



(b)

Fig.6.18: (a) Measured distance of a white diffusing target. (b) Measured distance precision

A sample 3D image acquired with an overall exposure time of 400ms is shown in Fig.6.19. The distance is coded in grayscale levels, while the image histogram can be seen on the right. Three peaks, two corresponding to the two hands and forearms and one to the back plane can be distinguished. The counts that are observed between the two hands are due to shadowing effect, due to the non-coaxial placement of the illuminator with respect to the camera sensor. This shadowing effect can be eliminated by using two illuminators or by placing the LEDs around the focusing optics of the sensor.

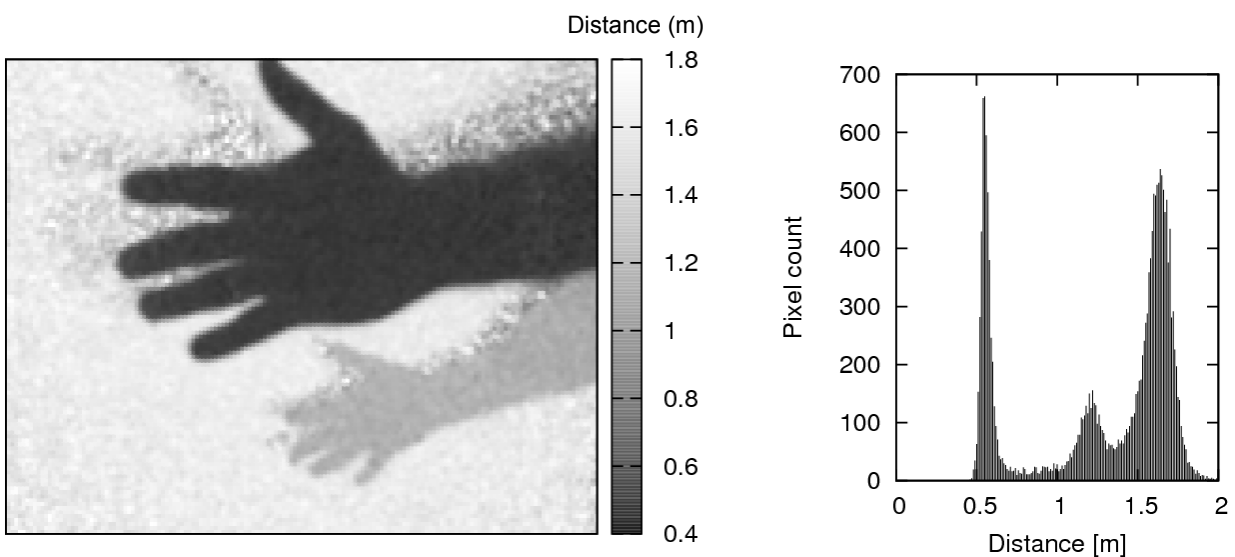


Fig.6.19: Left: Distance map of two hands in front of a white diffusing target. Distance in meters is coded in gray levels. Right: Histogram of distance distribution.

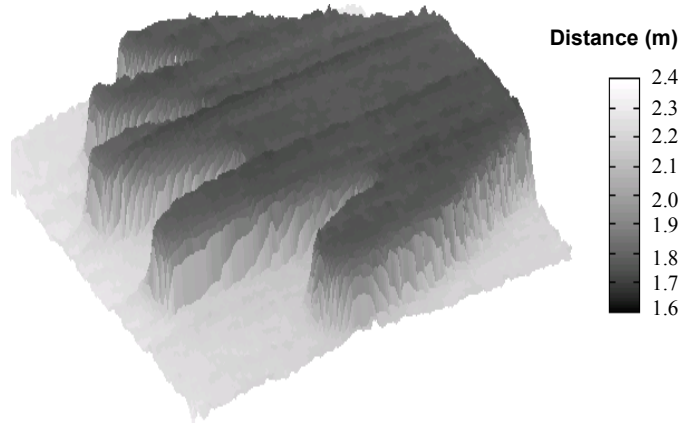


Fig.6.20: Sample of 3D image.

To demonstrate the 3D ranging capabilities of the TOF sensor Fig.6.20 also illustrates the measurement of a 3D scene. The distance information is coded in the z-direction and gray level intensity.

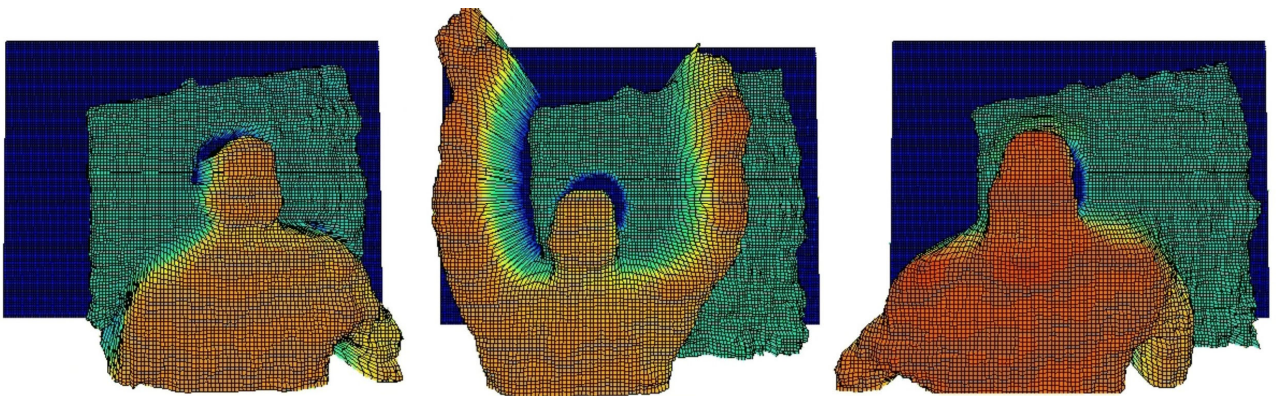


Fig.6.21: Sample frames from a video acquired in 7 3D frames per second.

Three sample frames from a video taken at 7fps are shown in Fig.6.21. The video, representing a person in front of a white panel, has been spatially filtered using a 3×3 median filter. In the video a threshold on the signal amplitude has been applied to filter out the noisy pixels due to shadowing effects and to insufficient power of the back-scattered light.

Table-VI summarizes the specifications of the sensor chip. A 120×160 CMOS Time-Of-Flight range camera based on Current Assisted Photonic Demodulators with $10 \times 10 \mu\text{m}^2$ pixel area and 24% fill factor. The chip, having a power consumption of 200mW, mainly due to the contribution of modulation current, demonstrate the feasibility of CAPD-based pixels in a medium resolution sensor fabricated on epitaxial wafers with standard resistivity. A range camera system is realized with the proposed sensor and a 3-LED illumination module delivering 140mW optical power on the target. The system, having $23^\circ \times 30^\circ$ field of view, is capable of acquiring a stream of 7 3D frames/s with a maximum non-linearity of 3.3% in the range 1.2m-3.7m and a precision better than 10 cm at 2m and 20 cm at 3m.

Table-VI: Sensor Summary

Technology	:	0.18 μ m 1Poly,4Metal CMOS technology
Power Supply	:	1.8V & 3.3V transistors
Sensor area	:	2.5 \times 2.5 mm ²
Number of Pixels	:	120 \times 160
Pixel size/Fill Factor	:	10 \times 10 μ m ² / 24%
Modulation Frequency	:	\geq 20MHz
Maximum non-linearity	:	3.3% in the range 1.2m-3.7m
Precision	:	10 cm at 2m and 20 cm at 3m
Power consumption	:	200mW

Chapter 07

Conclusion and Future work

In this century, imaging market continues to expand with new emerging applications. CMOS technology permits the integration of the circuits in the same die as the sensor, thus reducing the cost, power consumption, size and weight of the final camera. In this PhD dissertation, we have presented the development and characterization of a Current Assisted Photo mixing Demodulator (CAPD) and the realization of a 3D time-of-flight range camera in 0.18 μm CMOS technology.

The first part of the thesis provides some theoretical background, including an overview of photodetection in semiconductors, the definition of some conventional parameters of photodetectors, and a comparison between the classical CCD image sensors and CMOS imagers, which have achieved more importance in recent years. Nowadays, CMOS APS explosion is due to the fact that these devices can be fabricated with standard technologies that are gradually being miniaturized and improved, driven by the computer industry. This makes possible to employ more and more functionality within the sensor device and to realize more pixels in the same chip area. We have also given an overview of the different range measurement techniques, their corresponding advantages and drawbacks and the typical applications in distinct industrial areas. Among other optical techniques, the time-of-flight (TOF) technique has been preferred for this project because of the better performance in terms of acquisition speed and wide range of detectable distance as well as lower cost.

The core of the thesis has covered the most relevant issues related to the design and characterization of CAPD devices fabricated in a custom technology on high resistivity silicon substrates. Structures with different shapes and sizes have been considered and compared in terms of electrical and electro-optical performance. In particular, we have investigated the DC and dynamic demodulation performance of a linear-shaped CAPD device. For 10 MHz modulation frequency we measured a dynamic demodulation contrast of 25% for a 650nm modulated laser light source. We also measured the DC demodulation efficiency of the same device and the obtained result is about 100%. In the multiple strip CAPD devices, the effective potential gradient is applied to the multiple modulating electrodes, a fact that speeds up the signal charges transferring to the detection regions. The measured dynamic demodulation contrast is more than 20% at 30 MHz modulation frequency. The maximum phase linearity error between the applied phase and the measured phase is 3.9%. However, as multiple strip conductors are used in this device, the fill factor is very low with respect to the device size. Finally, a round shaped CAPD device has been characterized. The substrate contact of this device is not uniform and the applied drift field does not spread equally over the sensitive area, thus lowering the speed of the device, despite the device DC demodulation contrast is nearly 90%, which indicates good demodulation efficiency of this device at low frequency. Although not truly representative of the final CMOS CAPD devices, due to the largely different fabrication process, these test structures have been deemed appropriate to investigate the main design concepts and to provide a first test bench for comparison of experimental characteristics and simulation prediction, with reference to a technology for which all the relevant information is available.

Later, we have extensively investigated the simulation and experimental performance of a CMOS based CAPD device. The demodulator structure has been featured in a small pixel area of $10 \times 10 \mu\text{m}^2$ and fabricated in the standard 0.18 μm CMOS technology. Static characterization of the CAPD structures has been carried out using a 650nm laser to illuminate the device. Therefore, the device DC charge transfer efficiency was measured. It was found to be larger than 80% with a modulation voltage of 0.5V. The corresponding power consumption was measured and is 10 μW . At 45MHz modulation frequency, we measured the dynamic demodulation contrast of 40% with a modulation voltage of 800mV. Our proposed device can be competitive with existing photo-gate-based mixer technologies because it offers a larger demodulation contrast and a bandwidth comparable with the best devices presented so far. Phase measurement of the device showed an excellent linearity for sinusoidal and square waves where the maximum linearity error was found to be 0.11% for the former and 0.16% for the latter. In the case of square-wave modulation, a small phase linearity error indicates a small influence of the high frequency harmonic components on the phase determination. We obtained a peak quantum efficiency of 35% at

500nm wavelength and more than 20% in between 500nm and 600nm. The percentage of maximum deviation between measured shot noise and theoretical noise is 5.19%, which indicates that the device shot noise is low. The electro-optical characterization of this device has shown very encouraging results. The limited power consumption and the high demodulation contrast of the CAPD are suited for implementing it as a camera pixel for time resolved imaging applications such as time-of-flight range imaging.

Finally, this PhD thesis has focused on a 3D imaging system, based on CMOS CAPD device, and consisting of a 120×160 pixel array. The illustrated pixel layout is 10×10 μm^2 with a fill factor of 24%. For the TOF measurement, the illumination module is composed of 3 high power LEDs in series with a wavelength of 850nm. We have inspected the correlation function of our imaging system. A 20MHz modulation frequency and both the sine-wave and square-wave signals have been used in this measurement. We have found the maximum linearity error of the pixel array to be 0.60%, corresponding to an error of 4.5cm in the distance measurement. The 3D ranging performance of the system was measured using a square wave modulation signal with 20 MHz frequency. The sensor had a field of view of 23°× 30° and the average optical power inside this field was 140mW, while the LEDs were operated with an average current of 400mA and a maximum current of 800mA. The overall power consumption of the pixel array was found to be 200mW with a modulation current of about 400mA. The optical signal modulation depth was measured as 80%. A 30 ms integration time per frame was set, giving a range image frame rate of 7fps. The distance range between 1.2 m and 3.7m was measured and showed that the sensor was capable of measuring distance maps with quite a good accuracy. The maximum non-linearity was 3.3% in the range 1.2m-3.7m and a precision better than 10 cm at 2m and 20 cm at 3m was achieved. Apart from the first point (1.2m) in the range measurement series, where the sensor is close to saturation, the measurement precision increases with the square root of distance, as can be predicted theoretically for a diffusing target.

This dissertation has a broad aspect of TOF based 3D CMOS imager including device architecture, pixel structures, processing parameters and TOF related physical phenomena of the image sensor. However, the final operation of the system was limited in terms of modulation frequency and distance measurement. In our case the maximum modulation frequency reached 20MHz. The reason for not being able to increase the modulation frequency and distance further was the limitation of the available control and driving electronics and also the intrinsic limitation of the light source we used. To overcome these limitations, it is necessary to use a higher power illumination module and to optimize the driving electronics to drive the modulation frequency larger than 20MHz. Recently we have developed a high power CMOS based illumination module to be used as a light source. For further investigation, it can be possible to measure longer range distance at high modulation frequencies. For the miniaturization of the pixels and in order to achieve better image resolution, the evaluation of the integrated imagers in 130nm or 90nm CMOS technology is a promising research direction. Moreover, a compact 3D range camera with excellent performance of CAPD sensor can be developed, which will realize additional functionalities such as illumination system, distance calculation system and image processing tasks. The information of our present results from CAPD device and 3D image sensor functionalities can be used in advanced tasks, which lead us to predict broad applications in surveillance, inspection, safety, production and autonomous navigation systems.

Bibliography

- [01] S. Sze, "Physics of semiconductor devices", *John Wiley & Sons*, New York, U.S.A., (1981).
- [02] J.D. Eskin, H.H. Barret and H.B. Berber, "Signal induced in semiconductor gamma-rays imaging detectors." *Journal of applied physics* vol85, no2 pp 647-659, January1999.
- [03] Orly Yadid-Pecht, Ralph Etienne-Cummings, ISBN 1-4020-7962-1 "CMOS Imagers: From Photo-transduction to Image Processing" *Kluwer Academic Publishers*, (2004)
- [04] Edward S. Yang "Microelectronic Devices", International Edition, McGraw-Hill Book Company.
- [05] A. Moini, "Vision chips or seeing silicon," Center for High Performance Integrated technologies and Systems, University of Adelaide, Adelaide, Australia, *Technical Report*, March 1997.
- [06] S. Mendis, S. Kemeny, R. Gee, B. Pain, Q. Kim, and E. Fossum, "CMOS active pixel image sensors for highly integrated imaging system," *IEEE J. Solid-State Circuits*, vol. 32, p. 187, Feb. 1997.
- [07] M. Schanz, "Linear CMOS Image Sensors with Integrated Signal Processing," *PhD dissertation*, University of Duisburg, Duisburg, Germany, June 1998.
- [08] P. Aubert et al., "Monolithic Position Encoder with On Chip Photodiodes," *IEEE Journal of Solid State Circuits*, Vol. 23, No. 2, pp. 465-473, April 1988.
- [09] A. Mäkynen et al., "CMOS Photodetectors for Industrial Position Sensing," *IEEE Transactions on Instrumentation and Measurement*, Vol. 43, No. 3, pp. 489-492, Jun. 1994.
- [10] I. Brouk, and Y. Nemirovsky, "Dimensional effects in CMOS photodiodes," *Solid-State Electronics* Vol. 46, No. 1, pp. 19-28 Jan. 2002.
- [11] O. Y. Pecht, and R. Ginosar, "A Random Access Photodiode Array for Intelligent Image Capture," *IEEE Transactions on Electron Devices*, Vol. 38, No. 8, pp. 1772-1779, Aug. 1991.
- [12] B. Dierickx, "CMOS image sensors: Concepts and Limits," *SPIE—The International Society for Optical Engineering, Photonics West*, San Jose, USA, Short-course Notes, Jan 2000.
- [13] H. Tian, B. Fowler, and A. El Gamal, "Analysis of Temporal Noise in CMOS Photodiode Active Pixel Sensor," *IEEE J. Solid State Circuits*, vol. 36, no. 1, pp. 92-101, January 2001.
- [14] P. Seitz, "Image sensing with maximum sensitivity using industrial CMOS technology", *Proceedings of the SPIE*, Vol. **3099**, Munich, (1997).
- [15] T. Spirig, "Smart CCD/CMOS Based Image Sensors with Programmable, Real-time, Temporal and Spatial Convolution Capabilities for Applications in Machine Vision and Optical Metrology", *Ph.D. Dissertation ETH Zurich*, Switzerland, No. **11993**, (1997).
- [16] S. M. Sze, *Physics of semiconductor devices*, second edition, New York: John Wiley & Sons, 1985.
- [17] Elisenda Roca, Servando Espejo, Rafael Domínguez-Castro and Angel Rodríguez-Vázquez, "Light-Sensitive Devices in CMOS", internet source , gratefully acknowledged.
www.imse.cnm.es/Proyectos/dictam/2ND_PHASE/Dissemination/FULL_TEXT/CMOS/

- [18] W.S. Boyle, G. Smith, Charge-coupled semiconductor devices, *Bell System Techniques of Journal* 49 (1970) 587–593.
- [19] T. Yamada et.al., “A ½ -in 1.3 M-Pixel Progressive-Scan IT-CCD for Digital Still Camera Applications”, *IEEE Transactions on Electron Devices*, Volume 48, No. 02 pp. 222-230, 2001.
- [20] J.D.E. Beynon and D.R. Lamb, “Charge-coupled devices and their applications,” McGraw Hill Book Company (UK) Limited, 1980.
- [21] M.J.Howes and D.V. Morgan, “Charge-coupled Device and Systems,” John Wiley & sons Limited, 1979.
- [22] Dyson, P.E, Rossello, R.; CMOS Challenges CCD in Vivitar’s 3000; PMA ‘97: new technology and applications for digital photography; *The Seybold Report on Publishing Systems*; April 1997, Vol.26, Num. 13.
- [23] Albert J.P Theuwissen, “CCD or CMOS Image sensors for consumer’s digital photography” in 2001 International Symposium on VLSI Technology System and applications.
- [24] E.Fossum “Active Pixel Sensor: are CCD’s Dinosaurs?” *Proceedings SPIE charged coupled devices and solid state optical sensors vol.1900*, pp 2-14 San Jose, CA, USA 1993.
- [25] Hon-Sum Wong, “Technology and Device Scaling Considerations for CMOS Imagers”, *IEEE Transactions of Electron Devices*, vol43, no.12, pp 2131-2142, 1996.
- [26] VISION home page web site, URL: <http://www.vvl.co.uk/>.
- [27] E. Fossum, “CMOS Image Sensors: Electronic Camera-on-a-Chip,” *IEEE Transaction on Electron Devices*, Vol. 44, No. 10, pp. 1689-1698, Oct. 1997.
- [28] S. K. Mendis, S. E. Kemeny, R. C. Gee, B. Pain, Q. Kim, and E. R. Fossum, 'Progress in CMOS Active Pixel Image Sensors,’ *Proc. SPIE*, Vol. 2172, pp. 19- 29, 1994.
- [29] S. G. Wu, H. C. Chien, D. N. Yaung, C. H. Tseng, C. S. Wang, C. K. Chang and Y. K. Hsiao, “A High Performance Active Pixel Sensor with 0.18-um CMOS Color Imager Technology,” *IEEE IEDM Technical Digest*, pp.555-58, December 2001.
- [30] R. Hornsey, “Design and fabrication of integrated image sensors,” Institute for Computer Research, University of Waterloo, Waterloo, Canada, *Short-course Notes*, May 1998.
- [31] Hovanesian S.A., “Introduction to sensor systems”, Artech house, p.2.
- [32] B. Jaehne, H. Haussecker and P. Geissler, Eds., “Handbook of Computer Vision and Applications. Vol. 1: Sensors and Imaging”, Academic Press, San Diego,1999.
- [33] S. Ando and A. Kimachi, "Time-Domain Correlation Image Sensor: First CMOS Realization of Demodulator Pixels Array", *IEEE CCD/AIS Workshop*, pp.33-36, Karuizawa, Japan, 1999.
- [34] J. Ohta, K. Yamamoto, T. Hirai, K. Kagawa and M. Nunoshita, "An Image Sensor with an In-Pixel Demodulation Function for Detecting the Intensity of a Modulated Light Signal", *IEEE Trans. ED*, vol.50, no.1, pp166-172, January 2003.
- [35] Jarvis R.A. “A perspective on range finding techniques for computer vision”, *IEEE transections on pattern analysis and machine Intelligence*,Vol PAMI-5(2), pp 122-139, March 1983.

- [36] P. Besl, "Advances in machine vision" Springer-Verlag, chapter 1-Active optical range imaging sensors, pp 1-63, 1989.
- [37] I.Moring, T.Heikkinem, R.Myllyla and A.Kilpela, "Acquisition of three dimensional image data by a scanning laser range finder" Opt.Eng. Vol28 pp 897-905,1989.
- [38] S.T. Barnard and W.B. Thompson, "Disparity analysis of Images", IEEE Trans, Pattern Anal. Mach. Intel, 2(4), 333-340, 1980.
- [39] K.L. Boyer and A.C.Kak, "Color-Encoded structured light for rapid active ranging" IEEE Trans. Pattern Anal.Mach.Intell, 9(1), 14-28, 1987.
- [40] E. Zimmermann, Y. Salvade, and R. Dandliker "Stabilized three-wavelength source calibrated by electronic means for high-accuracy absolute distance measurements" Optical letters, vol.21.pp 531-533,1996.
- [41] Bahaa E. A. Saleh, Malvin Carl Teich, "Fundamentals of Photonics", ISBN 0-471-83965-5, John Wiley & Sons, (1991).
- [42] P.Hariharan, "Basics of Interferometry", ISBN 978-0-12-373589-8, Academic Press, (2007)
- [43] R. Schwarte, "Principles of 3D Imaging Techniques", in *Handbook of Computer Vision and Applications*, B. Jähne, H. Haussecker and P.Geissler (Eds.), Academic Press, (1999).
- [44] S. Bourquin, "Low-coherence interferometry based on customized detector arrays", Ph.D. Dissertation EPFL-Lausanne, Switzerland, No. 2171, (2000).
- [45] Price, M.; Kenney, J.; Eastman, RD. Hong, T. "Training and optimization of operating parameters for flash LADAR cameras". In *Proceedings of IEEE International Conference on Robotics and Automation*, San Antonio, TX, USA, 2007; pp. 3408-3413.
- [46] Büttgen, B.; Oggier, T.; Lehmann, M. "CCD/CMOS Lock-in pixel for range imaging: challenges,limitations and state-of-the-art". In *Proceedings of 1st Range Imaging Research Day*, Zurich,Switzerland, 2005; pp. 21-32.
- [47] <http://www.riegl.co.at>, (1998).
- [48] Z. Xu, Investigation of 3D-Imaging Systems Based on Modulated Light and Optical RF-Interferometry (ORFI) – ZESS – Forschungsberichte, Shaker Verlag Aachen, ISBN 3-8265-6736-6, 1999.
- [49] Schwarte, R., Heinol, H., Xu, Z., Li, J., and Buxbaum, B.: "Pseudo-Noise (PN)-laser radar without scanner for extremely fast 3D-imaging and navigation", Microwave and Optronics Conference (MIOP),Stuttgart , pp. 168-176,1997.
- [50] R.Jeremias, W.Brockherde, G.Doemens, B.Hosticka, L.List and P.Mengel, " A CMOS Photosensor Array for 3D Imaging Using Pulsed Laser" , Proceedings of ISSCC'01,paper 16.5,Sanfransisco (CA) USA,Feb, 2001.
- [51] O .M. Schrey, O. Elkhilili, P. Mengel', M. Petermann, W. Brockherde, B.J. Hosticka "A 4x64 Pixel CMOS Image Sensor for 3D Measurement Applications" , IEEE Journal of Solid State Circuits, vol.39, no.7, pp.1208-1212,July, 2004.
- [52] David Stoppa, Luigi Viarani, Andrea Simoni, Lorenzo Gonzo, Mattia Malfatti, Gianmaria Pedretti, "A 16x16-Pixel Range-Finding CMOS Image Sensor" Proceedings of IEEE European Solid-State Circuits Conference- ESSCIRC'04, pp. 419-422, September, 2004.

- [53] D.Stoppa, L.Viarani ,A.Simoni, L.Gonzo,M.Malfatti, G.Pedretti “ A 50×30 pixel CMOS sensor for TOF-based real time 3D imaging” proceedings of the IEEE workshop on CCD and advanced Image sensors, pp.230-233,2005.
- [54] R.lange and P. Seitz, “Solid- State Time-of-Flight Camera”, IEEE Journal of Quantum Electronics, Vol.37,no.3, pp. 390-397, March 2001.
- [55] R. Miyagawa and T. Kanade, “CCD-Based Range-Finding Sensor”, IEEE Trans. ED, vol.44, no.10, pp.1648-1652, 1997.
- [56] T. Oggier, M. Lehmann, R.Kaufmann, M. Schweizer, M. Richter, P. Metzler, G.Lang, F. Lustenberger, N. Blanc,“An all solid-state optical range camera for 3D real-time imaging with sub-centimeter depth-resolution(SwissRanger), Proceeding of SPIE Vol.5249, pp. 634-645, 2003.
- [57] Mesa Imaging website: [http: www.swissranger.ch](http://www.swissranger.ch)
- [58] Cannesta Inc. website: [http: www.canesta.com](http://www.canesta.com)
- [59] T.Ushinaga, I.A. Halim, T.Sawada, S.Kawahito,M. Homma, Y.Maeda , “A QVGA- size CMOS Time-of-Flight range image sensor with background light charge draining structure” Proceedings of SPIE,vol.6056,Jan,2006.
- [60] B. Buttgen, F.Lustenberger, P.Seitz,,”Demodulation pixel based on static drift fields”, IEEE Trans. on Electron Devices, vol.53, no.11 pp. 2741-2747, Nov, 2006.
- [61] C. Niclass, A.Rochas, P.-A. Besse, E.Charbon, “Toward a 3D camera based on single photon avalanche diodes”, IEEE journal of selected topics in Quantum Electronics, Vol.10, no.4, pp-796-802, July/August 2004.
- [62] C. Niclass, E.Charbon, “A single photon detector array with 64×64 resolution and millimetric depth accuracy for 3D imaging” ISSCC Digest of Technical Papers,pp.364-365, Feb.2005.
- [63] D.Stoppa,L.Puncheri ,M.Scandiuzzo,L.Gonzo,G.-F.Dalla Betta, A. Simoni, “A CMOS 3D imagers based on single photon avalanche diode”. IEEE transaction on circuit and systems I, pp.4-12 Jan, 2007.
- [64] Rudolf Schwarte, “Dynamic 3D Vision”, Proceedings of International Symposium on Electron Devices for Microwave and Optoelectronic Applications, pp.241-248, 15-16 November, 2001.
- [65] B. Buxbaum, R. Schwarte, T.Ringbeck, M. Grothof, X. Luan, “MSM-PMD as correlation receiver in a new 3D-ranging system”, Proc.SPIE Vol.4546,pp.145-153,2002.
- [66] Shaoji Kawahito, Izhal Abdul Halin,Takeo Ushinaga,Tomonari Sawada, Mitsuru Homma and Yasunari Maeda, “A CMOS TIme-of-Flight Range Image Sensor with Gates-on-oxide Structure”, IEEE Sesnors Journal, Vol.7 No.12 pp.1578-1585,December,2007.
- [67] D. Van Nieuwenhove, W.VanDer Tempel and M.Kuijck, “Novel Standard Detector using majority for guiding Photo-Generated Electrons towards Detecting Junctions”, Proceedings Symposium IEEE/LEOS Benelux Chapter, pp.229-232, 2005.
- [68] D.VanNieuwenhove, W.VanDerTempel, R.Grootjans, J.Steins and M.Kuijck, “Photonic demodulator with sensitivity control”, Sensors journal, IEEE, vol.7, no.3 pp.317-318, March 2007.

- [69] G. De Geronimo, G. Deptuch, A. Dragone, V. Radeka, P. Rehak, A. Castoldi, A. Fazzi, E. Gatti, C. Guazzoni, M. Rijssenbeek, W. Dulinski, S. Besson, M. Deveaux, M. Winter, "A novel position and time sensing active pixel sensor with field-assisted electron collection for charge particle tracking and electron collection for charge particle tracking and electron microscopy", *Nuclear Instruments and methods in Physics Research A*, vol. 568, pp. 167-175, 2006.
- [70] L. Pancheri, D. Stoppa, N. Massari, M. Malfatti, C. Piemonte, G.-F. Dalla Betta, "Current Assisted Photonic Mixing Devices Fabricated on High Resistivity Silicon" *IEEE SENSORS Conference*, Lecce, Italy, pp.981-983, 2008.
- [71] DESSIS 8.0 User Manual, Synopsys Inc.
- [72] P. Gulden, M. Vossiek, P. Heide, R. Schwarte, "Application of the photoelectronic mixing device to optical measurement of presence, distance and velocity", in *Proc. 2000 European Microwave Conference*, pp. 1-4.
- [73] R. Schwarte, "Dynamic 3D-vision", in *Proc. 2001 International Symposium On Electron Devices for Microwave and Optoelectronic Applications (EDMO)*, pp. 241-248.
- [74] D. K. Schroder, *Semiconductor material and device characterization*, 2nd ed. New York: Wiley, 1998.
- [75] C. F. Robinson, "Microprobe analysis," 1973.
- [76] R. Lange, P. Seitz, A. Biber and R. Schwarte. "Time-of Flight Range Imaging with a Custom Solid State Image Sensor", *EOS/SPIE International Symposium*. Munich, Germany, June 14-18 1999, pp. 180-191.
- [77] Cadence Verilog Language and Simulation, User Manual, Version 3.4, February, 2002, Cadence Design Systems, Inc.

Appendix-A

Related terminology of the image sensor used in this thesis

Sources:

<http://www.aapn.mcgill.ca/eng/resources/PhotonicsGlossary.pdf> & http://www.datx.com/solution_center_mach_vision/Glossary-of-Machine-vision.pdf (gratefully acknowledged).

Accuracy- The extent to which a machine vision system can correctly measure or obtain a true value of a feature. The closeness of the average value of the measurements to the actual dimension.

Ambient Light- Light which is present in the environment of the imaging front end of a vision system and generated from outside sources. This light, unless used for actual scene illumination, will be treated as background noise by the vision system.

Bandgap - In a semiconductor material, the minimum energy necessary for an electron to transfer from the valence band into the conduction band, where it moves more freely.

Bandwidth- The range of frequencies over which a particular device is designed to function within specified limits.

Beam splitter- An optical device for dividing a beam into two or more separate beams. A simple beam splitter may be a very thin sheet of glass inserted in the beam at an angle to divert a portion of the beam in a different direction.

CCD (Charge Coupled Device)- A photo-sensitive image sensor implemented with large scale integration technology.

Collimated Lighting- Radiation from a given point with every light ray considered parallel. In actuality, even light from a very distant point source (i.e. a star) diverges somewhat.

Crosstalk- The measurable leakage of optical energy from one optical channel to another. Also known as optical coupling.

Dark current- The current that flows in a photodetector when there is no optical radiation incident on the detector and operating voltages are applied.

Depth-of-Field- The range of an imaging system in which objects are in focus.

Detector- A device designed to convert the energy of incident radiation into another form for the determination of the presence of the radiation. The device may function by electrical, photographic or visual means and a device that provides an electric output that is a useful measure of the radiation that is incident on the device.

Dynamic Range- The measure of the range light sensitivity a sensor is able to reproduce, from the darkest to the brightest portion of a scene. Usually expressed in decibels.

Field-of-View- The 2D area which can be seen through the optical imaging system.

Fill factor (FF)- Ratio between the light sensitive pixel area and the total pixel area.

Focus- The point at which rays of light converge for any given point on the object in the image. Also called the focal point.

Focal Length- The distance from a lens principal point to the corresponding focal point on the object.

Gain- Also known as amplification. The increase in a signal that is transmitted from one point to another through an amplifier. A material that exhibits gain rather than absorption, at certain frequencies for a signal passing through it, is known as an active medium. In a photo detector, the ratio of electron-hole pairs generated per incident photon.

Image- Projection of an object or scene onto a plane (i.e. screen or image sensor).

Image Capture- The process of acquiring an image of a part or scene, from sensor irradiation to acquisition of a digital image.

Image Processing- Digital manipulation of an image to aid feature visibility, make measurements or alter image contents.

Incident Light- Light which falls directly onto an object.

Laser illumination- Lighting an object with a laser source for frequency selection, pulse width (strobe) control or for accurate positioning.

Linearity- For optical measurement instruments, generally used to refer to the deviation of a measured change of a performance parameter (e.g., power, wavelength) from the expected change.

MOS Array- Metal Oxide Semiconductor camera array sensor with random addressing capability, rows and columns of photodiodes and charge sent directly from the photodiode to the camera output.

Object- The 3D item to be imaged, gauged or inspected.

Photodiode- A single photoelectric sensor element, either used stand-alone or a pixel site, part of a larger sensor array.

Photometry- Measurement of light which is visible to the human eye (photopic response).

Photon- A quantum of electromagnetic energy of a single mode; i.e., a single wavelength, direction and polarization. As a unit of energy, each photon equals $h\nu$, h being Planck's constant and ν , the frequency of the propagating electromagnetic wave. The momentum of the photon in the direction of propagation is $h\nu/c$, c being the velocity of light.

Pixel- An acronym for "picture element." The smallest distinguishable and resolvable area in an image. The discrete location of an individual photo-sensor in a solid state camera.

Precision- The degree of spread or deviation between each measurement of the same part or Feature.

Quantum efficiency (QE)- Ratio between the number of generated electrons and the number of impinging photons.

Range Measurement- Determination of the distance from a sensor to the object.

Resolution - Describes the degree to which closely spaced objects in an image can be distinguished from one another.

Responsivity- Output per unit input of a radiation detector.

Sensitivity- In a radiation detector, the ratio of the output to the input signal.

Solid-State Camera- A camera which uses a solid state integrated circuit chip to convert incident light or other radiation into an analog electrical signal.

Spectral Analysis- Evaluation of the wavelength composition of object irradiance.

Spectral Response- Ratio of current and incoming light power for a given wavelength. Units: A/W.

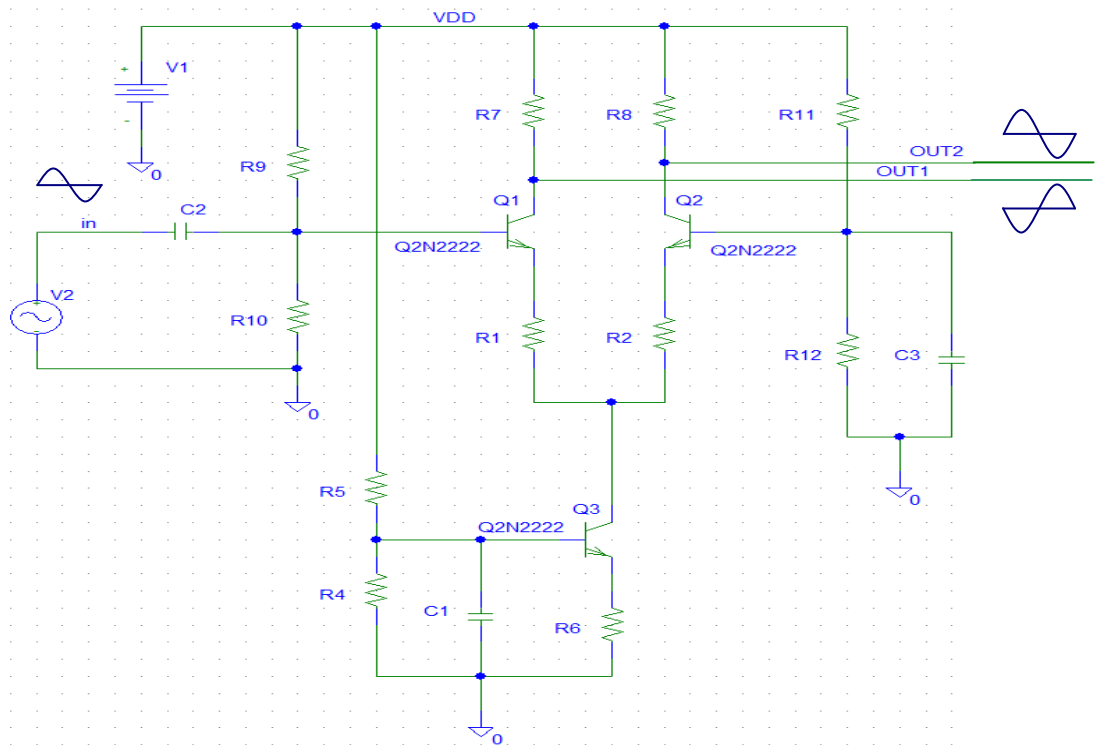
Structured Light- Points, lines, circles, sheets and other projected configurations used to directly determine shape and/or range information by observing their deformation as it intersects the object in a known geometric configuration.

Visible Light- The region of the electromagnetic spectrum in which the human retina is sensitive, ranging from about 400 to 750 nm in wavelength.

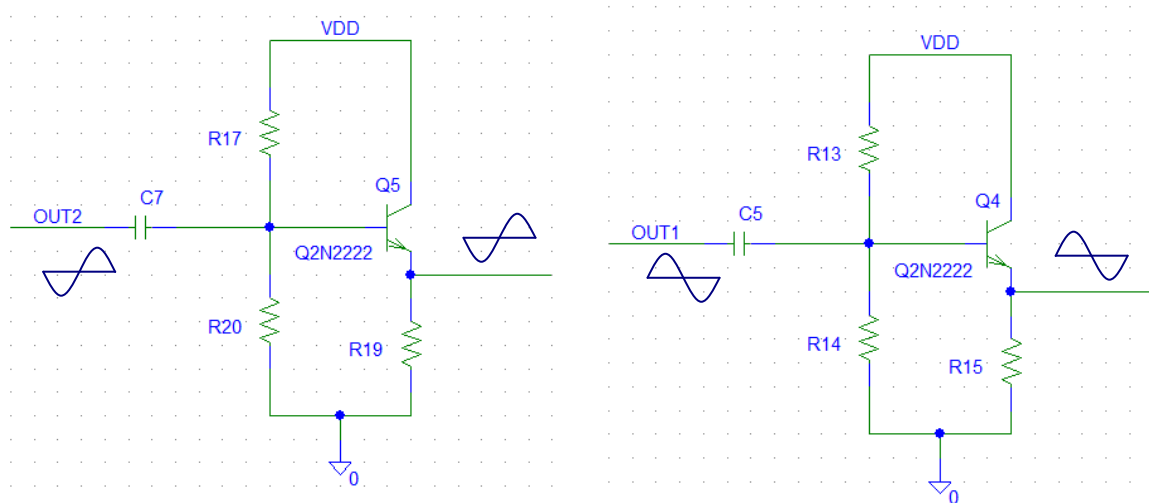
Wavelength- The distance covered by one cycle of a sinusoidal varying wave as it travels at or near the speed of light. It is inversely proportional to frequency.

Appendix-B

B.1 Pseudo Differential Amplifier: The beginning of the integrated circuit led to the development of the circuit configurations that used the strengths of monolithic technology advantage. The differential amplifier circuit configuration in particular assumed considerable prominence in this respect. In this thesis, for the electro-optical characterization of the test device we used a pseudo differential amplifier. In this experiment a dual output signal generator is used to generate two sine wave signals. One of the two signals is used to modulate a laser emitter and the other is connected to the input of a pseudo differential amplifier. Two output signals of the differential amplifier with 180° phase shift are connected to the modulating of electrodes of our device [see in Chapter 05 Fig.5.6 (b)]. In the following section we will describe a pseudo differential amplifier circuit and its operation.



(a)



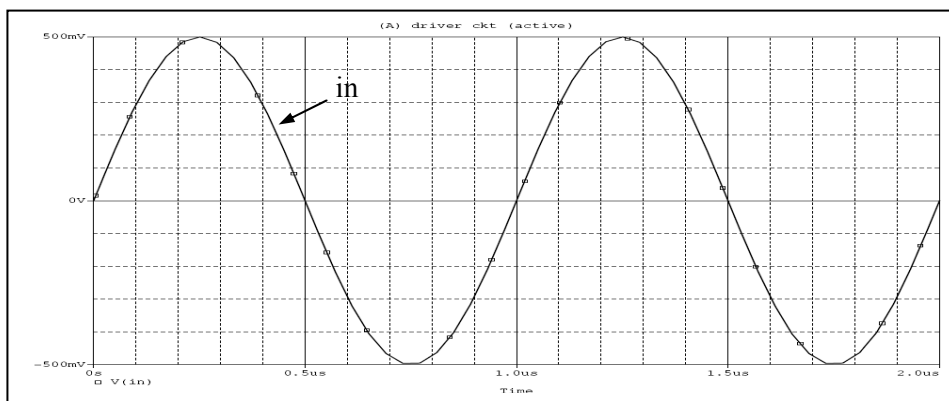
(b)

Fig.A.1: (a) Differential Amplifier circuit (b) Emitter follower Circuit

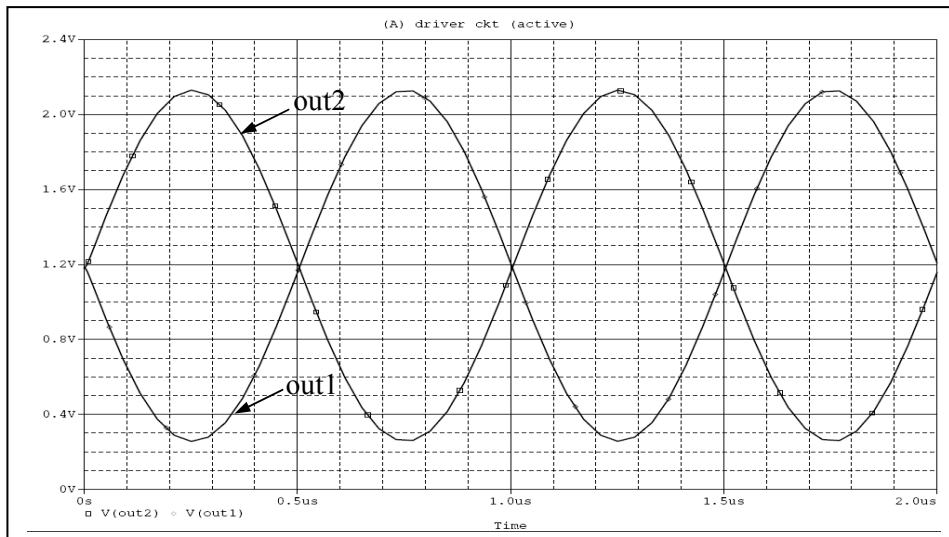
The differential pair circuits are one of the most widely used circuit building blocks. A differential amplifier provides two input and two output terminals, the input to be amplified is usually connected between one input and circuits ground. The other input is used for feedback and other purposes. The two outputs are taken from the collector terminals of the transistors Q1 and Q2. The basic differential amplifier circuit using BJTs is shown in Fig. B.1. The circuit consists of two common-emitter amplifiers with emitter resistor. Ideally both transistors Q1 and Q2 should have equal parameters; in this case the collector current in the transistor Q1 and Q2 can be described

$$I_{C1}=I_{C2} \text{ and } I_{E1}=I_{E2}=I_{C3}/2$$

A current source is used to DC bias Q1 and Q2. This current source is designed to overcome variations in the transistors parameters and for temperature compensation. A simple current source consists of an npn BJT and a biasing scheme similar to the common-emitter amplifier. The resistance R6 is chosen for the specified biasing current and insures that the transistor Q3 stays in the active mode of operation.



(a)



(b)

Fig.B.2: Simulation results of Differential Amplifier (a) Input (b) Output signal of the Emitter follower

In the *out1* and *out2* of the differential amplifier a common collector amplifier is used as a buffer because of its high input resistance. The collector is connected directly to the dc power supply which is an ac ground. The *out1* of differential amplifier is connected to the base and the output is taken from the emitter.

The output signal is in phase with the input signal looking from the input coupling capacitor to the base, the equivalent ac circuit has the bias resistors and the resistors in the emitter circuit as shown in Fig.B.1 (b)

The ac circuit can be simplified by combining the emitter and load resistors into one equivalent resistor ($R_E \parallel R_L$). As in all linear amplifiers, the voltage gain in this common collector amplifier is $A_V = V_{out}/V_{in}$. In this analysis of the gain, the bias resistors are not included because they do not directly affect the input signal although they do cause the loading effect on the source. In the figure of common collector circuit the input voltage is across emitter resistance r'_e in series with the $R_E \parallel R_L$. The output is across only $R_E \parallel R_L$. In the usual case r'_e is small compared to $R_E \parallel R_L$, so we can ignore the small drop across r'_e . It means that the input and output voltages are nearly the same.

Therefore,
$$A_V \cong 1$$

Because of the small drop across r'_e the actual gain is slightly less than 1. Since the output voltage on the emitter follows the input voltage that's why it is called emitter-follower. We know the emitter follower is characterized by a high input resistance which makes it a very useful buffer circuit to minimize the loading effect. Looking from the source of buffer circuit the total input resistance

$$R_{in(tot)} = R_1 \parallel R_2 \parallel [\beta_{ac} (r'_e + R_E \parallel R_L)]$$

The signal current gain for the emitter follower is I_{load}/I_S ; where I_{load} is the ac current in the load resistor and I_S is the ac current from the source. The current I_S is calculated using $V_{in}/R_{in(tot)}$. Since the voltage gain is approximately 1, the input voltage is also across the load. Thus, the load current is V_{in}/R_L .

Therefore,
$$A_I = \frac{I_{load}}{I_S} = \frac{V_{in} / R_L}{V_{in} / R_{in(tot)}}$$

Fig.B.2 shows the simulation result of the differential amplifier circuit. Fig.B.2 (a) indicates the input signal of the circuit and Fig.B.2 (b) shows the final output results of the amplifier after the emitter follower circuit.

B.2 Laser Driver Circuit: For the device experiment we need to use a laser illuminator to illuminate the device. I laser driver is used to drive the laser. We know solid state lasers use stimulated emission to generate light by creating a large population of high energy electrons and a small population of low energy electrons within a cavity surrounded by highly reflective surfaces. The laser driver design is a simple concept but we need to give some attentions such as large output current requirements and 'clean' operation at full bit-rate. Bipolar transistors are the best suited for the design of laser drivers due to their very high current densities, high gain and bandwidth.

The circuit of Fig.B.3 shows a simple driving circuit, using a common emitter configuration. This amplifier circuit converts an input base voltage into a collector current. Figure shows the arrangement most commonly used for biasing a discrete-circuit transistor amplifier if only a single power supply is available. The technique consists of supplying the base of the transistor with a fraction of the supply voltage V_{DD} through the voltage divider R_1 , R_2 and R_3 . Here R_3 is a variable resistance to adjust the circuit biasing. In addition, a resistor R_4 is connected to the emitter. The laser is connected to the collector of the transistor Q1 and the input signal is applied to the collector port also. The common emitter configuration is adapted with a bipolar transistor providing current gain and the output current flowing through the Laser. Lasing occurs only at current levels above the threshold current of the laser. A monitor diode is used to control the current fed through the laser by the constant circuit for stable and reliable operation. By adjusting the monitor resistance it can be possible to stabilize the laser current.

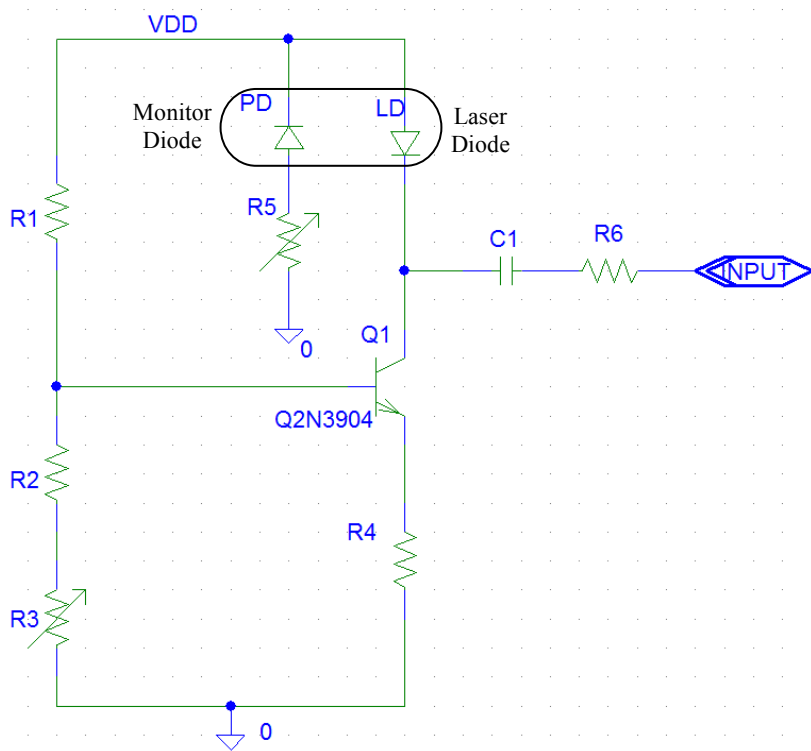


Fig.B.3: Simple laser driving circuit, using a common emitter configuration

Because the laser diodes have to be operated at a high current density and they are at risk of destroying themselves due to thermal runaway. As a result their electrical operation must be much more carefully controlled than a LED.